

PREPARATION AND CHARACTERIZATION OF POROUS ANODIC ALUMINA NANOSTRUCTURES

Thesis

Submitted in partial fulfillment of the requirements for the degree of
DOCTOR OF PHILOSOPHY

by

P. RAMANA REDDY



DEPARTMENT OF PHYSICS

NATIONAL INSTITUTE OF TECHNOLOGY KARNATAKA SURATHKAL,

MANGALORE - 575025

October 2017

TO MY FAMILY

DECLARATION

By the Ph.D. Research Scholar

I hereby declare that the Research Thesis entitled “**PREPARATION AND CHARACTERIZATION OF POROUS ANODIC ALUMINA NANOSTRUCTURES**” which is being submitted to the **National Institute of Technology Karnataka, Surathkal** in partial fulfillment of the requirements for the award of the Degree of **Doctor of Philosophy in Physics** is a *bonafide report of the research work carried out by me*. The material contained in this Research Thesis has not been submitted to any University or Institution for the award of any degree.

P. RAMANA REDDY

Reg. No.: 112024 PH11F08

Department of Physics

Place: NITK, Surathkal.

Date: October, 2017

CERTIFICATE

This is to *certify* that the Research Thesis entitled **PREPARATION AND CHARACTERIZATION OF POROUS ANODIC ALUMINA NANOSTRUCTURES** submitted by **P. RAMANA REDDY**, (Reg. No.: 112024 PH11F08) as the record of the research work carried out by him, is *accepted as the Research Thesis submission* in partial fulfillment of the requirements for the award of degree of **Doctor of Philosophy**.

(Dr. Ajith K.M)

Research Supervisor

(Prof. N.K. Udayashankar)

Research Supervisor

Chairman - DRPC

ACKNOWLEDGMENT

Foremost, it is my immense pleasure to thank my research supervisors, Prof. N.K. Udayashankar and Dr. Ajith K.M for their excellent and eminent guidance throughout my research work. I thank them for introducing me to the exciting areas of research in nanomaterials and nanostructures for multifunctional applications. I am indeed grateful for their constant encouragement and support. I am inspired greatly from their discipline and guidance in spite of their busy schedules.

I thank the members of my Research Progress Assessment Committee (RPAC) Dr. Ravishankar K.S (Department of Metallurgical and Materials Engineering) and Dr. H.S. Ngaraja (Department Physics), for their comments and suggestions during every stage of my dissertation work.

I am grateful to, Dr. M.N. Satyanarayana (H.O.D), Prof. H.D. Shashikala, Dr. H.S. Nagaraja, Dr. Deepak Vaid, Dr. Partha Pratim Das, Dr. Karthick Tarafder, Dr. T.K. Shajahan and Dr. Kishore Sridharan for their kind support.

I express my sincere thanks to Prof. Narayana Prabhu, Materials Science and Engineering Department, NITK for allowing me to carry out contact angle measurement of the samples and to his student Dr. Mrunali Sona for helping in this regard.

I would like to acknowledge the help and cooperation of the Physics staff including Mr. Dhanraj, Mrs. Saritha, Mrs. Ashalatha, Miss. Usha, Mr. S. Nayak and Mr. Chandranna during my research work and daily activities in the physics department.

I thank my beloved mother and father for their endless love and bestowing me all that because of which I stand today as what I am.

I express my sincere thanks to all my brothers and all my family members for their unending love and affection.

Finally, I would like to express my gratitude to my friends, Dr. Nagaraja K K, Dr. Paramesh G, Dr. G. Venkateswararao, Dr. A. Santosh Kumar, Dr. Sadananda Kumar, Dr. Manoj Kumar, Dr. Shashidhar, Dr. Hidayath Ulla, Dr. Kunal Kumar, B. Naveen Kumar Reddy, Kiran P, Brian Jeeven Fernandes, Mahendra K, Suchitra S.M, Sreejesh, Martha Ramesh, Bindu K, Kathik Bhat, Amuda, M. R. Kiran, Jean Maria Fernandes, Nimith, Achyutha K, Makesh M, Siby Thomas, Manju M. S, Karthik Hegde, Rajani, Ahmed Rizwan, Safir, Subhashini, Soumalya Bhattacharya, Akhila B, Shreyas, I. Ramesh Reddy, M. Vijay and others at NITK. I thank all my friends in NITK for their cooperation and encouragement.

I remain thankful to all those who helped me directly and indirectly in carrying out this work. I would like to salute and thank them, for those who are always giving me the required strength, energy, patience, knowledge, and resources which lead into *Success in Life*.

I thank the Authorities of National Institute of Technology Karnataka for giving me the opportunity for doing research in the department of physics. I am also grateful to Ministry of Human Resource Department (MHRD)-Government of India for awarding research scholarship.

Place: NITK, Surathkal

P. RAMANA REDDY

Date: October, 2017

ABSTRACT

This thesis describes the preparation and characterization of porous anodic alumina (PAA) membranes and synthesis of metal nanostructures based on PAA templates. The aim of this investigation is to optimize the process parameters and prepare metal nanostructures on the pores of PAA membranes using chemical methods. The effect of process parameters such as anodization duration, temperature of electrolytic bath and electrolyte concentration are systematically investigated. In this way pore diameter was found to be tunable from 20 to 100 nm and template thickness achieved varied from 20 to 100 μm . Hexagonal pore array with honeycomb-like structures were obtained via self-organised oxidation process. The pore diameters and interpore distances were varied by changing anodization conditions and pore widening time. The regularity ratio (RR) of the PAA membranes were studied in detail using 2D fast Fourier transform (FFT) analysis. Mechanical properties of PAA membranes such as hardness and Young's modulus were studied using micro and nanoindentation techniques. PAA membranes obtained in sulphuric acid exhibited an extremely high hardness of 7.5 GPa and Young's modulus was 146.5 GPa. The optical absorbance and photoluminescence of PAA membranes were investigated. The PL spectra of PAA membranes showed an asymmetrical behaviour in the blue region. This spectrum was divided into two subbands by Gaussian analysis, originating from two kinds of oxygen-deficient centers, F^+ (oxygen vacancy with one electron) and F centers (oxygen vacancy with two electrons) respectively. Contact angle measurements of PAA membranes were analysed at different anodization time and pore widening durations. Synthesis of metal nanostructures (Silver and Copper) by chemical method were studied and presented in detail.

Keywords: Porous anodic alumina, Anodization, Regularity ratio, pore diameter, interpore distance, photoluminescence, Microindentation, Nanoindentation.

Contents

List of Figures	iv
List of Tables	xi
1 INTRODUCTION	1
1.1 OVERVIEW	1
1.2 ANODIZATION OF ALUMINIUM	2
1.3 CHEMICAL REACTIONS IN ALUMINIUM ANODIZATION	3
1.4 CALCULATION OF THE STRUCTURAL PARAMETRES OF PAA MEMBRANES	5
1.5 IMAGE PROCESSING	7
1.6 APPLICATIONS OF PAA MEMBRANES	9
1.7 OBJECTIVES OF THE THESIS	11
1.8 ORGANIZATION OF THE THESIS	13
2 EXPERIMENTAL TECHNIQUES	14
2.1 PREPARATION METHOD	14
2.1.1 Experimental setup for template preparation	14
2.1.2 Preparation and morphology of anodic alumina oxide templates	15
2.1.3 Basic mechanism of oxide formation in PAA membranes	17
2.2 CHARACTERIZATION TECHNIQUES	19
2.3 MORPHOLOGICAL ANALYSIS	19

2.3.1	X-ray Diffraction	19
2.3.2	Scanning electron Microscopy (SEM)	21
2.3.3	Energy Dispersive X-ray analysis (EDX)	23
2.4	OPTICAL ANALYSES	23
2.4.1	Photoluminescence (PL)	23
2.4.2	UV-Vis spectroscopy (UV-Visible)	24
2.4.3	Contactangle measurement	25
2.5	MECHANICAL ANALYSIS	26
2.5.1	Microindentation	27
2.5.2	Nanoindentation	28
3	FABRICATION OF POROUS ANODIC ALUMINA MEMBRANES: OPTIMIZATION OF GROWTH PARAMETERS	30
3.1	INTRODUCTION	30
3.2	RESULTS AND DISCUSSION	31
3.2.1	Effect of anodization duration	31
3.2.2	Effect of electrolyte concentration	34
3.3	PORE PARAMETERS (D_p , D_i , α and n)	38
3.4	FAST FOURIER TRANSFORM (FFT) BASED ANALYSIS OF PORE REGULARITY	45
3.4.1	Effect of anodization duration	45
3.4.2	Effect of electrolyte concentration	48
3.4.3	Conclusions	50
4	MECHANICAL PROPERTIES OF POROUS ANODIC ALUMINA MEMBRANES	51

4.1	INTRODUCTION	51
4.2	RESULTS AND DISCUSSION	52
4.2.1	Micro indentation	52
4.2.2	Nanoindentation	54
4.2.3	Conclusions	61
5	OPTICAL PROPERTIES OF POROUS ANODIC ALUMINA MEMBRANES	63
5.1	INTRODUCTION	63
5.2	RESULTS AND DISCUSSION	64
5.3	EFFECT OF ANODIZATION DURATION	68
5.4	EFFECT OF ELECTROLYTE CONCENTRATION	71
5.4.1	Conclusions	78
6	GROWTH OF DIFFERENT NANOSTRUCTURES USING PAA MEMBRANES	79
6.1	INTRODUCTION	79
6.2	WETTABILITY ANALYSIS	80
6.2.1	Effect of anodization duration	80
6.2.2	Effect of pore widening duration	82
6.3	SILVER NANOPARTICLES	84
6.4	ALUMINA NANOWIRES	87
6.5	COPPER NANOWIRES	89
6.5.1	Synthesis of Cu nanowires inside the pores of PAA membranes	89
6.5.2	Conclusions	92

7	SUMMARY AND FUTURE DIRECTIONS	93
7.1	SUMMARY	93
7.2	FUTURE DIRECTIONS	96
	REFERENCES	97

List of Figures

1.1	Schematic diagram of (left) barrier type alumina and (right) porous type alumina (Nielsch et al., 2001).	3
1.2	Idealized structure of anodic porous alumina (A) and a cross-sectional view of the anodized layer (B) (Balde et al., 2015).	4
1.3	Schematic representation of cross-sectional view and illustration of ion movement through the electrolyte/oxide and oxide/metal interface during the anodization in an acidic electrolyte (Patermarakis and Mousoutzanis, 1995).	5
1.4	FE-SEM micrograph of PAA membrane obtained in 0.3 M of oxalic acid (a) before binarization and (b) after binarization performed using Image-J software.	7
1.5	Screen shot micrographs of PAA membranes before and after Thresholding images using Image-J software	8
1.6	Flow chart gives the image analysis process performed using Image-J software.	8
2.1	Schematic of lab-made anodization set-up: icebath, magnetic stirrer, anodization holder and DC power supply	15
2.2	Schematic diagram of PAA membrane preparation using two-step anodization process in oxalic acid.	16
2.3	SEM micrographs and cross sectional images of PAA membrane formed in oxalic acid (a, c) and sulphuric acid (b, d).	17

2.4	Typical anodizing current density as a function of time. (a) formation of a barrier layer on the aluminum surface, (b) random formation of pore centers, (c) pores deepen and form a new barrier layer on the interface between the metal and the oxide and (d) stable growth of pores.(Alkire et al., 2008)	18
2.5	(a) Reflection of X-rays from different atomic planes, illustrating Bragg's law, (b) XRD (Rigaku-MiniFlex-600) instrument.	21
2.6	(a) Schematic representation of scanning electron microscope, (b) SEM(JEOL-JSM 6380LA) instrument	22
2.7	(a) Schematic diagram of experimental set-up for PL measurements, (b) PL (FluoroMax-4)instrument.	24
2.8	Schematic diagram of single beam UV-Visible spectrometer.	25
2.9	(a) Schematic representation of contact angle of liquid drop on solid surface, (b) Contact angle (FTA-200) instrument	26
2.10	(a) Schematic Diagram of Vickers indenter and (b) Clemex micro hardness tester.	28
2.11	Typical load/unload vs. displacement curve for a solid with non-flat indenter. Here P_{max} is maximum load applied to the indenter, h_{max} is the displacement or depth at maximum load and h_f is the depth after complete unloading.	29
3.1	XRD pattern of PAA membranes with Al substrate at 8 °C and 18 °C .	31
3.2	SEM top-view micrographs (a, c and e), their cross-sectional images (b, d and f) of PAA membranes formed in 0.3 M oxalic acid at 8 °C at different anodization durations such as 2 h, 6 h and 10 h for both steps.	32
3.3	SEM top-view micrographs (a, c and e), their cross-sectional images (b, d and f) of PAA membranes formed in 0.3 M oxalic acid at 18 °C at different anodization durations such as 2 h, 6 h and 10 h for both steps.	33

3.4	XRD pattern of the PAA obtained at different electrolyte concentration (0.1-0.9 M)	35
3.5	SEM top-view micrographs (a, c, e, g and i), their cross-sectional images (b, d, f, h and j) of PAA membranes formed in 0.3 M oxalic acid at 18 °C at different electrolyte concentrations such as 0.1, 0.3, 0.5, 0.7 and 0.9 M.	36
3.6	Thickness and growth rate as a function of electrolyte concentration for PAA obtained at 0.1 to 0.9 M.	37
3.7	Pore diameter and interpore distance distribution of PAA membranes prepared for different anodization durations, 2h (a) pore diameter (b) interpore distance, 4h (c) pore diameter (d) interpore distance and 6h (e) pore diameter (f) interpore distance at 8 °C and 18 °C.	39
3.8	Pore diameter and interpore distance distribution of PAA membranes prepared for different anodization durations, 8h (a) pore diameter (b) interpore distance and 10h (c) pore diameter (d) interpore distance at 8 °C and 18 °C	40
3.9	The influence anodizing duration on the pore diameter (a) and interpore distance (b) of porous anodic alumina films formed in 0.3M $H_2C_2O_4$ for 2h, 4h, 6h, 8h and 10h at 8 °C and 18 °C	40
3.10	The influence anodizing duration on the wall thickness (a) and barrier layer thickness (b) of porous anodic alumina films formed in 0.3M $H_2C_2O_4$ for 2h, 4h, 6h, 8h and 10h at 8 °C and 18 °C	42
3.11	Anodizing duration influence on the pore density (a) and porosity (b) of porous anodic alumina films formed in 0.3M $H_2C_2O_4$ for 2h, 4h, 6h, 8h and 10h at 8 °C and 18 °C	42
3.12	Effect of the anodization duration on the proportionality constant λ_p between the pore diameter and applied anodizing potential.	43

3.13	SEM top view micrographs, 2D FFT images and average profiles of the FFT radius of PAA formed 0.3 M of $H_2C_2O_4$ for 2h (a, b and c), 6h (d, e and f), and 10 h (g, h and i) at 8 °C.	46
3.14	SEM top view micrographs, 2D FFT images and average profiles of the FFT radius of PAA formed 0.3 M of $H_2C_2O_4$ for 2h (a, b and c), 6h (d, e and f), and 10 h (g, h and i) at 18 °C.	47
3.15	Average regularity ratio vs anodization duration (2, 4, 6, 8 and 10h)at 18 °C and at 18 °C.	47
3.16	SEM top view micrographs, 2D FFT images and average profiles of the FFT radius of PAA formed with 0.1 M (a, b and c), 0.3 M (d, e and f), 0.5 M (g, h and i), 0.7 N (j, k and l) and 0.9 M (m, n and o) of $H_2C_2O_4$ under a constant anodization potential of 40 V	48
3.17	The regularity ratio as a function of electrolyte concentration (0.1-0.9 M) for PAA formed under a constant potential of 40 V	49
4.1	FE-SEM images (a, f), cross-sectional images (b, g), fast Fourier transforms (c, h), radial averages (d, i) and average surface roughness (e, j) of PAA membranes obtained in 0.3 M oxalic and 0.3 M of sulphuric acid at 8 °C.	53
4.2	SEM micrographs of the indent mark of the PAA using Vickers Indenter and corresponding morphologies after applying loads at the edge of the indented PAA formed using sulphuric acid:0.98 N (a ,b) and 9.8N(c, d) and oxalic acid:0.98 N (e, f) and 9.8 N (g, h) at 8 °C	55

4.3	AFM topographic images of nano indentation imprints in oxalic acid (a) and sulphuric acid (d) after indentation. Surface height profiles of residual Berkovich indents made on the three directions of PAA membranes (Oxalic acid: b, c and Sulphuric acid: e, f). SEM images typical Berkovich of the nano indentation imprints and indented images obtained by applying a load of 10mN for oxalic acid (g, h) and sulphuric acid (i, j).	57
4.4	Load-displacement curves of the PAA membranes formed in Oxalic and Sulphuric acid (a, b). The surface elastic deflection, contact depth and indenter displacement as a function of the applied load for PAA membranes in oxalic (c) and sulphuric acid (d). Hardness (e) and E Modulus (f) as a function of load (P_{max}) for PAA membranes prepared in oxalic and sulphuric acids.	59
5.1	UV-Visible absorption spectra (a) and plot of $(\alpha hv)^2$ verses $hv(eV)$ of PAA membranes for oxalic and sulphuric alumina.	65
5.2	Reflectance spectra of PAA membranes obtained in oxalic and sulphuric acid solution.	65
5.3	CIE chromaticity diagram for reflectance spectra in (a) oxalic and (b) sulphuric alumina.	66
5.4	PL spectra with Gaussian, separated into two sub-bands in oxalic (a) and sulphuric (b) alumina. Chromaticity diagram for PL spectra in (c) oxalic and (d) sulphuric alumina.	67
5.5	PL spectra of the PAA membranes obtained using anodization of Al foils in 0.3M oxalic acid at 8 °C and 18 °C under different anodization durations of 2h (a, b), 4h (c, d) and 10h (e, f) respectively. Each spectrum can be Gaussian separated into two sub bands, which are shown in thick lines and labeled as 1 and 2.	69

5.6	Effect of anodization duration on F/F^+ ratio at 8 °C and 18 °C (a), relationship of F/F^+ ratio and regularity ratio at 8 °C (b) and 18 °C (c)	70
5.7	UV-Visible spectra of PAA membranes at different electrolyte concentrations (0.1-0.9 M)	72
5.8	PL spectra of the PAA membranes obtained at different electrolyte concentrations (0.1-0.9 M) (a) under a constant potential of 40 V and Gaussian analysis of PAA membranes at 0.1 (b), 0.3 (c), 0.5 (d), 0.7 (e) and 0.9 M (f).	73
5.9	CIE chromaticity diagram for (a) maximum wavelength (max), (b) F^+ centers, (c) F centers for PAA obtained at different electrolyte concentrations and (d) Defect-distribution model of PAA.	75
5.10	Effect of electrolyte concentration on F/F^+ ratio of PAA membranes.	76
5.11	Relationship of regularity ratio and F/F^+ ratio PAA membranes.	76
6.1	Shows contact angle measurement images of PAA membranes obtained at different anodization durations. (a) 2h, (c) 6h, (e) 10h at 8 °C and (b) 2h, (d) 6h, (f) 10h at 18 °C.	81
6.2	Contact angle measurement images of PAA membranes formed at different pore widening durations: Without pore widening (a). Sulphuric acid and (b). Oxalic acid; 1 hr pore widening (c). Sulphuric acid and (d). Oxalic acid; 2 hr pore widening (e). Sulphuric acid and (f). Oxalic acid; In acetone medium (g) Sulphuric acid (h) Oxalic acid.	83
6.3	FESEM images (a, e), Cross-sectional image (b), EDAX (f), 2D FFT images (c, g) and radial averages (d, h) of PAA and Ag-PAA	85
6.4	XRD pattern of (a) PAA and (b) Ag-PAA.	86
6.5	Schematic of the formation of the ANW from APA: (a) porous structure of the APA with triplet point, (b) Thinning of pore walls after dissolution of PAA in H_3PO_4 solution, (c) Alumina nanowires formation from triplet points.	87

6.6	SEM micrographs of the ANW formed in sulphuric and oxalic acid with the dissolution of APA membranes 30 (a, b) and 45 min (c, d) in H_3PO_4 solution.	88
6.7	Schematic of synthesis of Cu nanowires into the pores of PAA. (a) PAA with highly ordered pores, (b) Free standing PAA film, (c) Electroless deposition of copper nitrate solution into the pores of PAA and (d) Formation of Cu nanowires. The corresponding FE-SEM images and variation of color (inset) of the sample for each step (e, f, g and h) of fabrication of Cu nanowires.	90
6.8	(a) FE-SEM images of copper nanowires grown inside the pores of PAA, (b) Higher magnified image of randomly oriented Cu nanowires, (c) Variation of cross-sectional image PAA before and after growth of Cu nanowires and (d) EDX spectra of Cu nanowires.	91

List of Tables

3.2.1 SEM EDX data of PAA membranes prepared under different anodization durations at 8 °C and 18 °C	34
3.2.2 Thickness and growth rate data of PAA membranes obtained at different electrolyte concentrations (0.1-0.9 M)	38
3.3.1 Pore diameter and interpore distance of PAA membranes using SEM micrographs and the software Image-J, for different anodization durations carried out in 0.3 M oxalic acid at a temperature of 8 °C.	43
3.3.2 Porosity and Pore density of PAA membranes using the SEM micrographs and the software Image-J, for different anodization durations carried out in 0.3 M oxalic acid at a temperature of 8 °C.	44
3.3.3 Pore diameter and interpore distance of PAA membranes using the SEM micrographs and the software Image-J, for different anodization durations carried out in 0.3 M oxalic acid at a temperature of 18 °C.	44
3.3.4 Porosity and Pore density of PAA membranes using the SEM micrographs and the software Image-J, for different anodization durations carried out in 0.3 M oxalic acid at a temperature of 18 °C.	44
3.3.5 Barrier layer thickness, wall thickness and proportionality constant of PAA membranes using the SEM micrographs and the software Image-J, for different anodization durations carried out in 0.3 M oxalic acid at a temperature of 8 °C.	44

3.3.6 Barrier layer thickness, wall thickness and proportionality constant of PAA membranes using the SEM micrographs and the software Image-J, for different anodization durations carried out in 0.3 M oxalic acid at a temperature of 18 °C.	45
3.4.1 Regularity ratios of PAA membranes obtained at different electrolyte concentrations (0.1-0.9 M)	50
4.2.1 Nano mechanical analysis of PAA membranes formed in oxalic acid .	60
4.2.2 Hardness and Young's moduli of PAA membranes formed in oxalic acid	60
4.2.3 Nano mechanical analysis of PAA membranes formed in sulphuric acid.	61
4.2.4 Hardness and Young's modulus of PAA membranes formed in sulphuric acid.	61
5.2.1 Structural analysis of PAA membranes formed in oxalic and sulphuric acids	68
5.2.2 PL data of PAA membranes formed in oxalic and sulphuric acids . . .	68
5.3.1 PL data analysis of PAA membranes. The maximum peak positions of the PAA membranes (λ), band1 (λ_1) and band2 (λ_2) are presented. . .	71
5.4.1 PL data of PAA membranes for different electrolyte concentrations (0.1-0.9 M)	77
5.4.2 PL and regularity ratio analysis data of PAA membranes for different electrolyte concentrations (0.1-0.9 M)	77
6.2.1 Surface energy values of the obtained PAA membranes.	82
6.2.2 Contact angle data for PAA membranes formed in 0.3 M of oxalic and sulphuric acid at different pore widening durations.	84

Chapter 1

INTRODUCTION

This chapter provides a preface to the nanoporous metal oxides, an overview of porous metal oxides especially anodic alumina (Al_2O_3) nanostructures, basics of anodic alumina formation and their fundamental properties and application studies. The chapter ends with the objectives and organization of the thesis.

1.1 OVERVIEW

Nanoporous metal oxides have attracted a great deal of attention by researchers in the field of nanotechnology, due to their unique physical and chemical properties. Nanoporous materials have shown a lot of flexibility for the control of their structural properties, because of their high surface to volume ratio and large porosity. Porous nanomaterials of different pore size, porosity, pore distribution and composition have been developed for different potential applications such as energy harvesting and storage (Lu and Zhao, 2004), sensors (Kumeria et al., 2014), solar cells (Martinson et al., 2007), light emitting diodes (Fu et al., 2011), photocatalysis (Albu et al., 2007), optics and electronics (Basu et al., 2001), capacitor dielectrics (Jason and Wood, 1955), templating nanomaterials and in prevention of corrosion of metal substrates from their functional environment (Bengough and Stuart, 1923). Owing to certain useful physico-chemical and surface properties, porous materials are widely used in the laboratory and industrial scale in diverse research areas, such as petrochemicals (Kulkarni, 1998), medicine (Corma, 2003), chemistry (Doadrio et al., 2004), energy and advance composite materials (Vallet-Regí, 2006). Porous anodic oxide films have also been obtained on surfaces

of valve metals, such as titanium (Paulose et al., 2006a), hafnium (Takahashi et al., 1988) niobium (Sieber et al., 2005a), tantalum (Sieber et al., 2005b), tungsten (Mukherjee et al., 2003), vanadium (Stefanovich et al., 2004), and zirconium (Tsuchiya et al., 2005). Among these nanoporous metal oxides, Al_2O_3 based porous oxides had a significant impact on the nanomaterials research because of easy fabrication besides a variety of potential applications. The ideal structure of porous anodic alumina (PAA) membranes were reported long ago at certain anodizing conditions (Masuda and Fukuda, 1995). Afterwards, with the expanding progress in nanotechnology, PAA has been used as an ideal template for fabrication of various types of nanostructured materials (Stepniowski and Salerno, 2014). The most significant structural difference between PAA and other metal oxides is that in PAA pore array is continuous while in the other metal oxide pore array is in discontinuous manner (Gong et al., 2001). One of the salient features of PAA is its application in quite diverse sectors of materials science (Ingham et al., 2012). This thesis deals with the fabrication, structural, mechanical, optical characterization and some application studies of anodic alumina (Al_2O_3) based nanostructures.

1.2 ANODIZATION OF ALUMINIUM

Anodization of aluminium has been widely used for several decades to manufacture protective and decorative coatings on Al surface. Anodization of aluminium is an electrochemical oxidation process carried out by applying positive voltage to Al electrode dipped in an electrolyte and this results in the thickening of its oxide namely, Al_2O_3 . Due to their easy fabrication procedure and their excellent chemical, thermal stability and corrosion resistance porous anodic alumina (PAA) membranes have been used in many products for the last fifty years. The development of electron microscopy techniques made it possible to study the nanostructures of PAA membranes (Diggle et al., 1969). Depending on the anodization process parameters, it was found that two types of oxides can exist such as barrier-type and porous-type oxide layers. If Al is anodized in acidic electrolytes such as oxalic, sulphuric and phosphoric acids, deep pores, having pore diameters 20-100 nm and length few microns are formed. This type of oxide is rep-

represented as porous anodic aluminium oxide (PAA). Instead, if Al is anodized in neutral or basic solutions ($pH > 5$) a flat, non-porous, insulating barrier oxide is formed. As shown in the Figure 1.1, anodic aluminium oxide layer (barrier or porous) result from anodization process. It consists of two parts called inner layer and outer layer. These inner and outer layers are due to the non-homogeneity in anionic content across the film thickness (Nielsch et al., 2001). The general structure of PAA membrane is shown in the Figure 1.2. Self-organized anodic porous alumina grown by the anodization of aluminium can be represented schematically as a closed-packed array of hexagonally arranged cells containing pores in each cell center (Figure 1.2). Highly ordered PAA membranes are often characterized by various parameters such as a pore diameter, wall

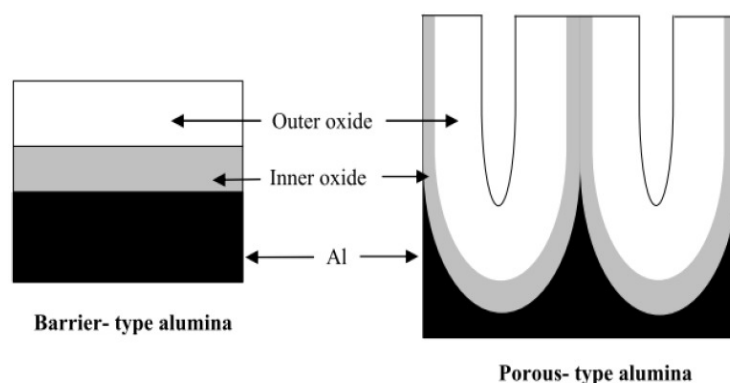


Figure 1.1 Schematic diagram of (left) barrier type alumina and (right) porous type alumina (Nielsch et al., 2001).

thickness, barrier layer thickness and interpore distance. The uniform pore diameter, which is easily controlled by altering the anodizing conditions, can range from a few nanometres to hundreds of nanometers. The depth of fine parallel channels can even exceed $100 \mu m$, a characteristic which makes anodic porous alumina one of the most desired nanostructures with a high aspect ratio and high pore density.

1.3 CHEMICAL REACTIONS IN ALUMINIUM ANODIZATION

Anodic oxides (barrier-type and porous-type) formed by the anodization of aluminium are amorphous oxides. The studies showed no presence of crystalline structure of alu-

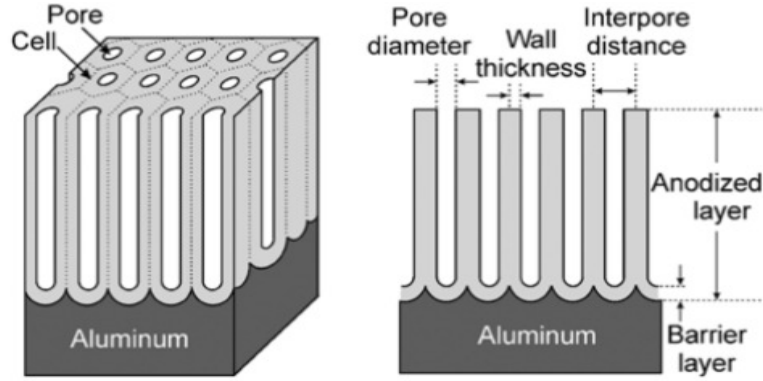
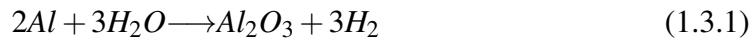


Figure 1.2 Idealized structure of anodic porous alumina (A) and a cross-sectional view of the anodized layer (B) (Balde et al., 2015).

mina $\gamma\text{-Al}_2\text{O}_3$. Additionally, the anodic alumina is characterized by incorporation of electrolyte ions within its structure, thus it cannot be considered as pure Al_2O_3 . The overall chemical reaction during the anodization of aluminium can be written as (Li et al., 1998):

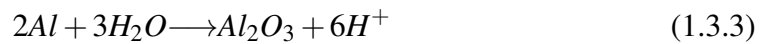


Although this reaction is formally correct, it does not reflect the details of the whole electrochemical process. A schematic illustration of processes occurring during anodization is shown in the Figure 1.3. The equilibrium chemical reactions can be summarized as follows:

At the metal/oxide interface, Al^{3+} ions are formed and migrate into the oxide layer



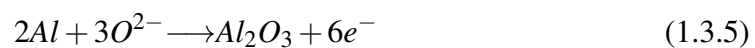
The Al^{3+} ions migrate outwards under the electric field across the oxide from the metal/oxide interface toward the oxide/electrolyte interface:



At the oxide/electrolyte interface the water-splitting reaction occurs (Despić and Parkhutik, 1989)



The O^{2-} (oxide) ions migrate inwards under the electric field across the oxide from the oxide/electrolyte interface toward the metal/oxide interface, to form Al_2O_3 :



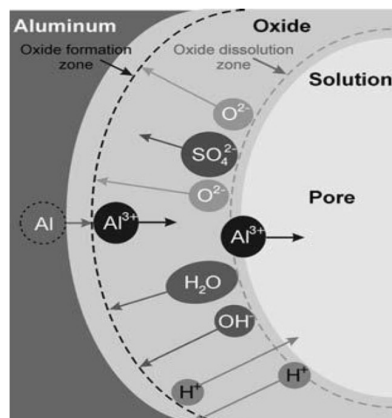
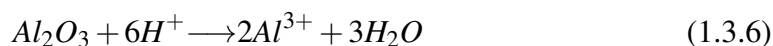


Figure 1.3 Schematic representation of cross-sectional view and illustration of ion movement through the electrolyte/oxide and oxide/metal interface during the anodization in an acidic electrolyte (Patermarakis and Moussoutzanis, 1995).

In the acidic electrolyte where the oxide is soluble, the film dissolution happens:



Some anions in the electrolyte may also be incorporated in the PAA layer, in addition to the above principal reactions. In the case of phosphates and chromate as electrolytes, due to high current efficiency the majority of Al^{3+} are involved in the formation of oxide at the electrolyte/oxide interface. In contrast, for anodizing in oxalate electrolytes accompanied with low current efficiency, the direct ejection of Al^{3+} ions to the electrolyte is expected. These two processes of the formation of oxide result in the migration of the electrolyte ions (*e.g.* SO_4^{2-} , COO_2^{-2} , PO_3^{-4}) through the oxide layer in the formation of PAA membranes.

1.4 CALCULATION OF THE STRUCTURAL PARAMETERS OF PAA MEMBRANES

A major advantage of PAA membranes is that pore parameters such as layer thickness, pore diameter, cell size and barrier layer thickness can be controlled by anodizing conditions or chemical methods. One of the most important parameters is pore diameter. Pore diameter mainly depends on the anodizing conditions, where the main controlling parameter is the anodization voltage. Earlier reports have confirmed that in the case of porous anodic alumina obtained from oxalic acid, the pore diameter D_p has a linear

relation with applied anodizing potential (U) in the following manner:

$$D_p = \lambda_p \cdot U \quad (1.4.1)$$

Where λ_p is a proportionality constant (1.29 nmV^{-1}). As a result the uniform pore diameter achievable is in the range of 10-100 nm. The interpore distance (D_i) is also linearly proportional to the anodizing potential:

$$D_i = \lambda_i \cdot U \quad (1.4.2)$$

Where λ_i is approximately 2.5 nmV^{-1} . Each electrolyte has a restricted working potential range. The anodizing potential range for sulfuric acid is 10 – 25V, for oxalic acid 40 – 80V, and phosphoric acid, it is 120 – 200V for mild anodization process. Another morphological feature, namely, the wall thickness (W) is estimated from pore diameter and interpore distance using the equation:

$$W = \frac{D_i - D_p}{2} \quad (1.4.3)$$

One of the important parameters is the porosity of the PAA membrane. Assuming a perfect hexagonal array of pores in the alumina obtained by self-organization, the porosity (α), can be expressed as (Sulka and Parkola, 2007):

$$\alpha = \frac{\pi}{2\sqrt{3}} \cdot \left(\frac{D_p}{D_i}\right)^2 = 0.907 \left(\frac{D_p}{D_i}\right)^2 \quad (1.4.4)$$

Where D_p and D_i denote the pore diameter and the interpore distance, respectively. The knowledge of porosity is an important factor for electrochemical deposition using PAA membranes because it defines the working electrode surface. The porosity of PAA may vary a lot due to various types of pore widening mechanisms during anodization in different electrolytes or post-treatment procedures (etching of barrier layer). It is usually in the range of 10 – 40% or even more in extreme cases, however the standard values are around 10%. The following relation was used for the calculation of barrier layer thickness (B) for the anodization performed in oxalic acid (Zaraska et al., 2010).

$$B = 1.12 W \quad (1.4.5)$$

This compact dielectric layer at the pore bottom makes electrochemical deposition into the pores almost impossible or at least very complicated. On account of this limit, the thickness of the barrier layer is extremely important and can determine required modifications of PAA for various applications.

1.5 IMAGE PROCESSING

The basic parameters of PAA membranes have been measured using the Image-J 1.37v software (<https://imagej.nih.gov/ij/>). At first, Image-J software was used to identify all the nanopores within the particular image and the center of mass coordinates was estimated for every pore. Then, the file with this information was employed as input to calculate pore diameter (D_p), interpore distance (D_i), porosity (α) and pore density (n). In order to obtain such characteristic features of the pores, a binarization of the SEM image (Garg, 2013) is performed and this provides an image containing black

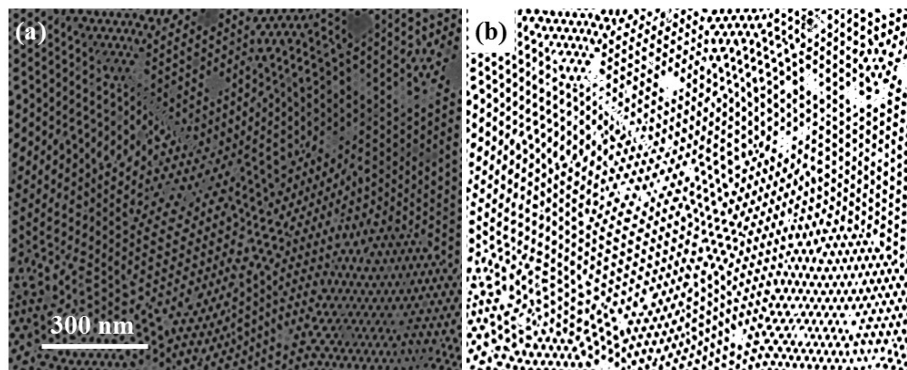


Figure 1.4 FE-SEM micrograph of PAA membrane obtained in 0.3 M of oxalic acid (a) before binarization and (b) after binarization performed using Image-J software.

and white zones. The black zones correspond to the pores and the white zones are associated with the alumina top surface of the PAA as shown in the Figure 1.4. To study the morphological analysis of PAA membranes using image-J software, first of all we have to do binarization of SEM image of PAA membrane. There are three methods to perform binarization of the SEM image: 1) Fixed Thresholding Method, 2) Otsu Method

and 3) Kittler Method

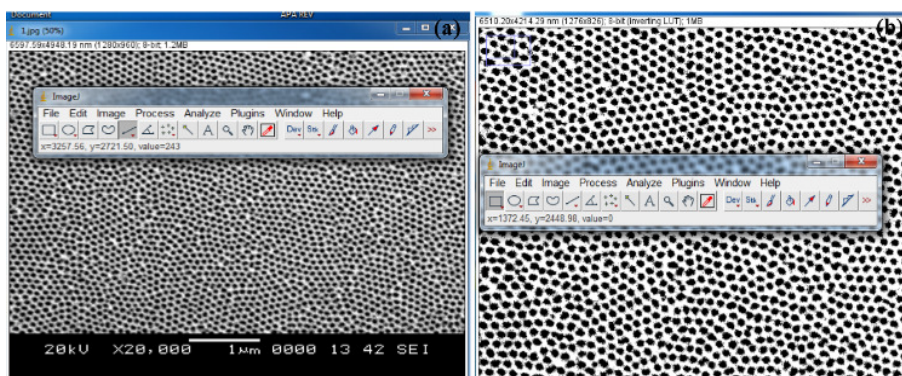


Figure 1.5 Screen shot micrographs of PAA membranes before and after Thresholding images using Image-J software

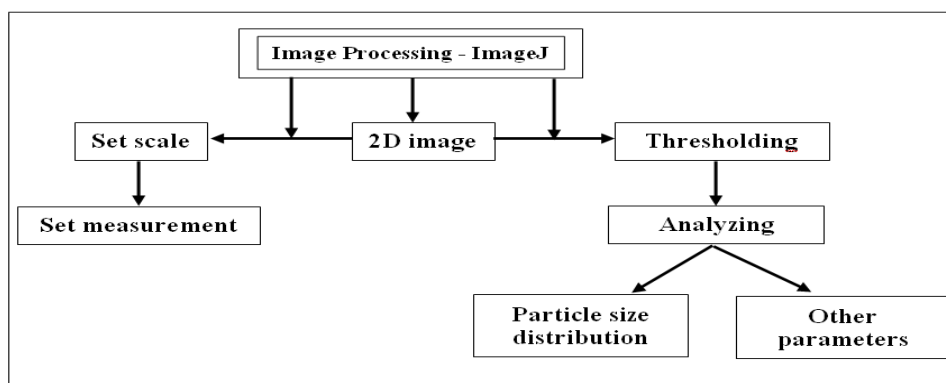


Figure 1.6 Flow chart gives the image analysis process performed using Image-J software.

Flow chart of the image analysis process developed within Image-J is shown in the Figure 1.6. The analysis was carried out in two steps. The measure scale is set that is suitable with the 2D SEM image. Furthermore the detail and required measurements are set up includes in the first step, shown in the screenshot Figure 1.5. In the second step, the boundaries of each grain on the image were detected. The boundary can easily be detected from binary images, which were obtained from the thresholded SEM images. After Thresholding the SEM image, choosing parameters required for analysis is analyzed from the analyzing part of Image-J software.

In order to obtain a quantitative estimation of the regularity of the pores, a self-correlation function (SCF) (Mínguez-Bacho et al., 2012) was performed on the SEM

micrographs. The resulting self-correlated image (SCI) is a mathematical image that gives information of how well an image correlates with itself under discrete displacements in all possible directions. Also, the pore regularity has been studied using the open software WSxM 4.0 (Horcas et al., 2007). A typical fast Fourier transform was carried out for PAA membranes obtained by various anodization durations using WSxM software. For a quantitative analysis, the correction aspects such as the number of pores (n), analyzed surface area (S) and PAA porosity (α) have been considered in our analysis. The averaged regularity ratio (R), derived from the FFT radial average was calculated using the following equation (Stepniowski et al., 2014a).

$$R = \frac{I}{W} \frac{\sqrt{n}}{S^{3/2}} \quad (1.5.1)$$

Where I is the intensity of the radial average, W is the width of the radial average at half of its height, n is the number of pores on the analyzed image and S is the analyzed surface area. The radial averages form soft, separate peaks which make the estimated results truthful. The physical significance of the radial average is that it exhibits the distribution of the interpore spaces in the inversed space. Hence, if the distribution of pores is not uniform, the FFT image will not be clear and the intensity of the radial average would be lower. Moreover, the abscissa of the radial average peak corresponds to the average interpore space (Stepniowski et al., 2014a) and breadth of the peak at half of its width is strongly related to the distribution of the interpore spacing values. The combination of both the software Image-J and WSxM allows the calculation of the most relevant geometrical features of the PAA membranes.

1.6 APPLICATIONS OF PAA MEMBRANES

Anodic porous alumina which exhibits a characteristic nano level-honeycomb structure has received increasing attention both experimentally and theoretically (Su and Zhou, 2008a). PAA membranes have been extensively used as templates for fabrication of various nanostructured materials such as nanodots, nanowires, nanotubes, and many other types, especially to realize the collective functioning of arrays of nano-elements which may not be realized by individual nano-elements. PAA membranes are essential for applications in high density magnetic media, photonic crystals, semiconductor de-

vices, lithium- ion batteries, solar cells and nanocapacitors (Su and Zhou, 2008b), due to the following advantages: the quasi-periodic arrangement of the nanopore channels, narrow distribution of pore sizes and interpore distances, excellent thermal stability, and very low cost.

Recently, the research on self-organization in nanotechnology has gained momentum with the use of PAA. Due to its hydrophilic properties, PAA is currently used in micro humidity sensors that show good response and are easily fabricated. These devices are based on integrated electrodes that take advantage of the sensitive capacitance-humidity relationship (Yao et al., 2009). Furthermore, these PAA membranes are now employed as electrochemical biosensors. PAA membrane also acts as a support for enzymes and other biological materials (Adiga et al., 2009). Another interesting characteristic of PAA is its useful biological properties, and for years, PAA has been used in dental and bone implants due to its biocompatibility and ease of integration with medical implant.

To date, for RF and microwave applications, PAA has been used mainly as an isolation layer in multilevel circuits. PAA is also formed on a glass substrate to produce Multichip Module Deposited (MCM-D) substrates. 1-D materials such as nanowires or carbon nanotubes have already shown great promise in applications for quantum devices. By using PAA, researchers have been able to fabricate an inexpensive, high throughput and easily tunable template. Anodized porous alumina has several advantages even to produce Carbon Nanotubes (CNTs). Primarily, they offer consistently parallel pore channels and have the ability to engineer varying pore diameters. They are optically transparent in the visible spectrum and are resistant to most chemicals except for strong bases and acids. CNTs in PAA have been explored by several groups (Sui et al., 2002).

Lithium batteries composed of nanowire arrays as anode show much higher energy capacity compared with conventional thin film batteries, due to the large surface area and a reduced Li-ion diffusion length. With the length of nanowire increasing, the

capacity can be further increased. However, due to the agglomerate of the high aspect-ratio nanowires, the total surface area decreases, and significant degradation of performance was found (Storm et al., 2003). The potential applications in electrochemical devices, quantum wires and electrodes for rechargeable Li-batteries are just some of the numerous areas that have been explored (Storm et al., 2003). The optical properties of PAA have been well documented and the material has been utilized in both polarizers and electroluminescent devices. The photoluminescent (PL) properties of PAA are further enhanced when they are filled with semiconductor composites such as CdS or ZnO. These optical nanowires are being utilized in polymer light emitting diodes (PLEDs) and optical displays (Wu et al., 2007).

Metal nanostructures have become the subject of intensive research in view of their potential applications in the areas of plasmonics (Walsh and Chumanov, 2001), nano-electronics (Yanson et al., 1998), biology (Reich et al., 2003), superconductivity (Tian et al., 2003) and magneto-sensors (Liu et al., 1998). For these applications, nanostructures are usually embedded in various substrates including PAA membranes (Lu et al., 2009). Also, PAA membranes are widely used materials for the nanomaterial fabrication because of the ease of synthesis of these membranes with good control over the pore dimensions. Cu and Ag nanostructures have been grown onto the pores of PAA membranes by electroless deposition method in the present work. The advantage of the electroless deposition is that there is no necessity for the surface to be electronically conductive unlike the electrochemical deposition method and the nanoowires can be controlled by varying pore dimensions.

1.7 OBJECTIVES OF THE THESIS

In the last few years, the effort is focused on the fabrication of nanostructured materials by electrochemical template-synthesis method and the development of porous anodic alumina nanostructures. In this thesis, we were focussed on the synthesis of metal (Ag, Cu) nanostructures inside the pores of PAA membranes using electro-less deposition method. The goal is to develop highly effective, versatile and low-cost PAA

nanostructures. The optimization of growth parameters of PAA membranes, such as anodization duration and electrolytes concentration were presented in detail. In addition to this, a degree of pore ordering array of PAA membranes were discussed by 2D fast Fourier transform (FFT) using Image-J and WSxM softwares. Structural features of PAA membranes such as pore diameter, interpore distance, porosity, pore density, wall thickness and barrier layer thickness were studied in detail. The effect of porosity and regularity ratio of pores on hardness and Young's modulus of PAA membranes were investigated. Contact angle measurements of PAA membranes were studied by varying anodization time and pore widening duration. Furthermore, the effect of anodization duration and electrolyte concentration on Photoluminescence (PL) properties of PAA membranes has been discussed.

The objectives of the proposed research are:

1. To fabricate nano-porous anodic alumina by electrochemical two-step anodization process.
2. To study the optical, morphological and structural properties of the fabricated nano porous alumina templates.
3. To study the effect of high temperature annealing on the structural properties of fabricated nano porous alumina.
4. To study the mechanical properties of the fabricated porous anodic alumina templates.
5. To prepare metal (Cu, Ag) nanostructures on porous anodic alumina templates by using chemical methods.

1.8 ORGANIZATION OF THE THESIS

The thesis is organized as follows:

Chapter 1 presents the overview of metal oxide nanostructures, especially Al_2O_3 nanostructures, preparation methods and application areas. The chapter also includes the objectives and organization of the thesis.

Chapter 2 gives the brief description of two-step anodization process, which is employed to synthesize PAA and Al_2O_3 based nanostructures. This is followed by a concise description of different characterization techniques.

Chapter 3 begins with a discussion of influence of anodization duration and electrolyte concentration on the growth mechanism of PAA membranes. Also, it contains the discussion on the degree of pore ordering in PAA membranes by changing the anodization process parameters.

Chapter 4 deals with the mechanical properties of PAA membranes such as hardness and Young's modulus obtained using micro and nanoindentation techniques. The effect of porosity and regularity ratio of pores on mechanical properties of PAA membranes were studied in detail.

Chapter 5 gives the optical properties of PAA membranes using UV-Visible and Photoluminescence techniques. The effect of anodization duration and electrolyte concentration on optical properties of PAA membranes was studied in detail.

Chapter 6 gives the applications of alumina based nanostructures. It begins with the wettability analysis of alumina nanostructures and also it discusses the synthesis of metal nanostructures such as copper and silver nanowires grown on alumina membranes using electroless deposition method.

Chapter 7 gives the overall summary of the results described in the previous chapters. Moreover, the scope for future research work in this area is also discussed.

Chapter 2

EXPERIMENTAL TECHNIQUES

This chapter gives a detailed description of experimental technique involving two-step anodization process, which is employed to obtain PAA based nanostructures in the present research work. This includes an account of the basic mechanism of oxide formation in PAA membranes. Measurement techniques and experimental setup used to study the physical parameters such as structural, optical, mechanical and wettability were discussed.

2.1 PREPARATION METHOD

2.1.1 Experimental setup for template preparation

In the present work, indigenously assembled anodization setup was used. The schematic of the experimental setup is shown in the Figure 2.1. The main part of the setup was a laboratory scale two-electrode electrochemical cell. The cell consists of a two electrode setup stand, DC power supply, ice bath and a magnetic stirrer. The electrolyte was taken in a borosil beaker and placed on the magnetic stirrer. The typical volume of the electrolyte was 100 ml. The magnetic stirrer was used to stir the electrolyte continuously. This keeps the electrolyte at equilibrium temperature. The potentiostat used had a working range of 0-300 V and 0-5 A.

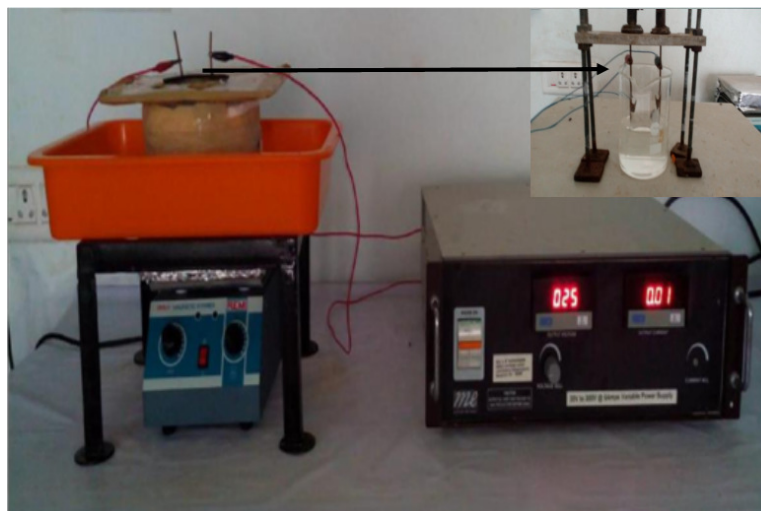


Figure 2.1 Schematic of lab-made anodization set-up: icebath, magnetic stirrer, anodization holder and DC power supply

2.1.2 Preparation and morphology of anodic alumina oxide templates

In the present study, PAA membranes were prepared using two step self-organized anodization process. The purpose of this section is to describe the preparation conditions of self-assembled porous alumina with variable pore diameter and aspect ratio. The preparation of porous alumina consists of three processes, (a) pre-treatment, (b) anodization and (c) post-treatment shown in the Figure 2.2. Firstly, the aluminum foil (high purity- 99.99%, Merck-0.3 mm thickness) is cleaned with acetone in an ultrasonic bath for 30 min to remove contaminations. Then the aluminum foil is annealed in air at 500 °C for 5 h to reduce the stress in the material. The electrochemical polishing of the aluminum foil is then carried out in a mixture of perchloric acid ($HClO_4$) and ethanol (C_2H_6O) with a volume ratio of 1 : 4, with polishing parameters of current density (200 mA/cm^2) for 2 min at 10 °C. After polishing, the aluminum surface becomes smooth and shiny. In our experiments, oxalic acid and sulphuric acid were employed as the anodizing electrolytes. As an example, in the following we will describe the necessary anodizing conditions for oxalic acid; the anodizing potential being 40 V. For each electrolyte, there is a certain potential and concentration which can be applied without burning the oxide film. The standard potential and concentration for sulphuric acid are 25 V and 0.3 M respectively. The self-organized growth of pores takes place perpen-

dicular to the surface of the aluminum. In order to get a highly ordered arrangement of pores, porous oxide layer was etched away chemically after the first step anodization. This etching process was carried out in a mixed solution containing 6% phosphoric acid (H_3PO_4) and 1.8% chromic acid (H_2CrO_4) in a water bath at 60 °C for 2 h. After removing of the first oxide layer, the second step anodization was carried out with the same conditions as those used for the first step. The anodizing time was varied from 2-20 hours depending on the required thickness. To obtain a free-standing template,

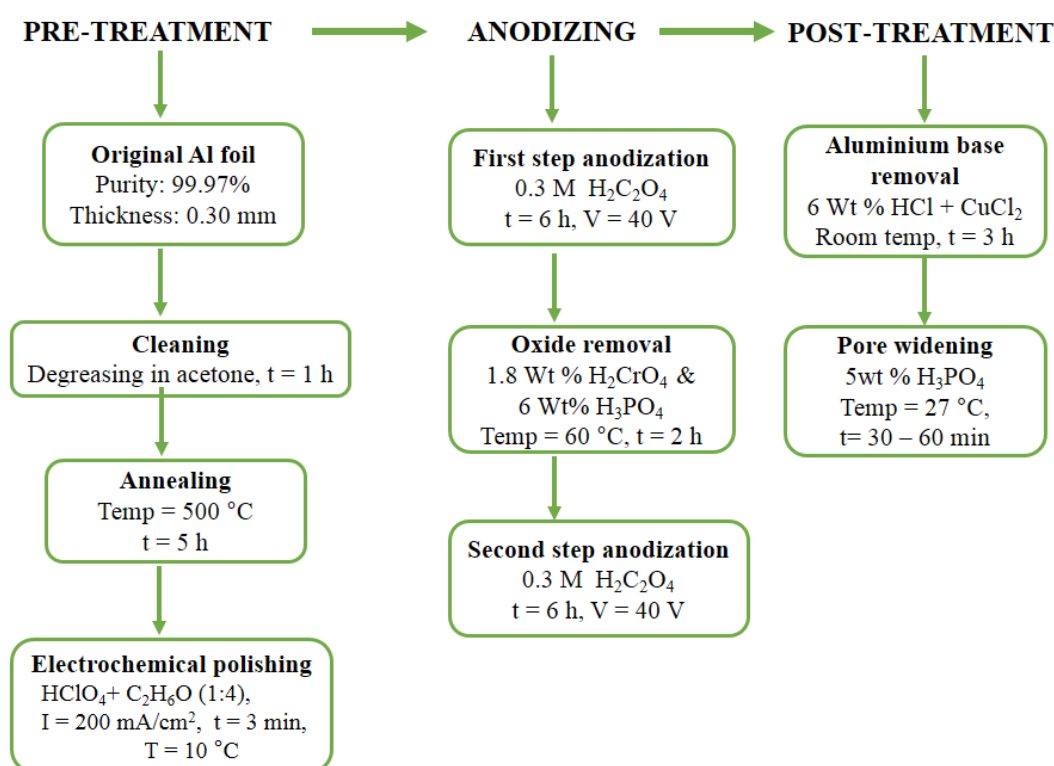


Figure 2.2 Schematic diagram of PAA membrane preparation using two-step anodization process in oxalic acid.

usually it takes more than 8h for anodization. Otherwise, the template was too thin and fragile to handle. The remaining aluminum base and barrier layer was removed from the nonoxide side to open the pores. This step was called the post-treatment process. A mixed solution of hydrochloric acid (HCl) and copper chloride ($CuCl_2$) was employed to dissolve the aluminum base. The barrier layer was removed afterwards with a 5wt% phosphoric acid H_3PO_4 solution. For pores grown in oxalic and sulfuric acid, these processes were carried out at 30 °C for 30 min, 30 °C for 15 min respectively. In gen-

eral, with an increasing etching time, the pores were significantly widened because the walls were dissolved along the horizontal direction. That means that the pore diameters were increasing together with a decrease of pore wall thickness. SEM images and cross sectional views of PAA membranes prepared using oxalic and sulphuric acid as electrolytes were shown in the Figure 2.3. The average pore diameter of PAA membranes formed in oxalic acid was 62 nm and those formed in sulphuric acid was 22 nm.

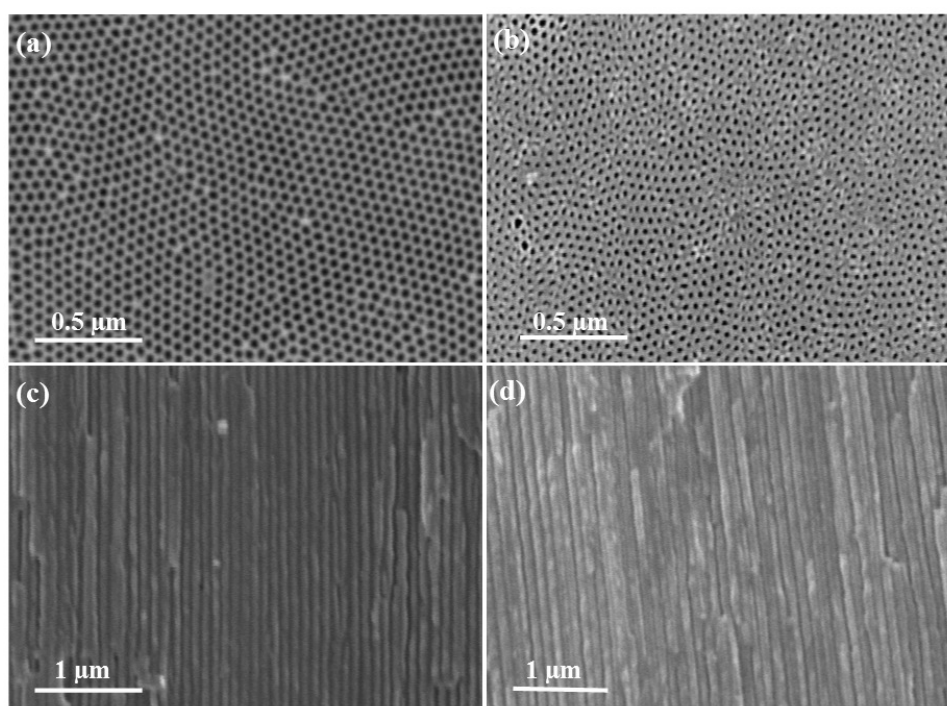


Figure 2.3 SEM micrographs and cross sectional images of PAA membrane formed in oxalic acid (a, c) and sulphuric acid (b, d).

2.1.3 Basic mechanism of oxide formation in PAA membranes

The preparation and applications of PAA membranes were studied over the last three decades, but the formation and growth mechanism of pores still remain quite controversial. Several theories have been proposed and developed. First research group reported that oxygen ions are generated on the bottom of the pores at the gas/electrolyte interface. Meanwhile, the dissolution of the oxide layer leads to the pore growth (Baumann, 1936). Second research group developed a theory according to which a homogeneous barrier film is formed at the beginning of the anodizing process and the dissolution is

caused by the current. Meanwhile the current raises the local temperature enhancing the dissolution of the oxide (Keller et al., 1953). Another research group developed a theory for the oxidation process (Murphy and Michelson, 1962). They reasoned that the outer side of the barrier layer was transformed into hydroxide and hydrate compounds because of the contact with the electrolyte. This layer could absorb or bond anions from the electrolyte to create a gel-form matrix. The inner layer is a dense oxide layer. Transmission of oxygen anions towards the metal base leads to the oxidation between the inner and the outer layer, and initial pores are formed at defect sites

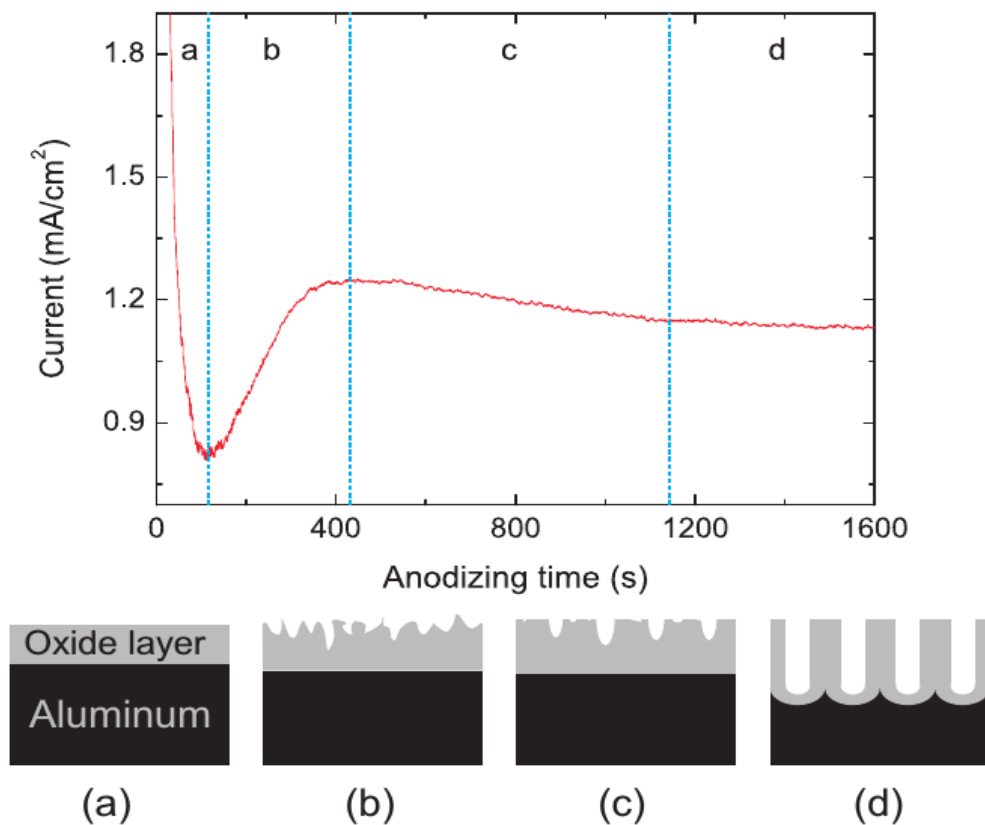


Figure 2.4 Typical anodizing current density as a function of time. (a) formation of a barrier layer on the aluminum surface, (b) random formation of pore centers, (c) pores deepen and form a new barrier layer on the interface between the metal and the oxide and (d) stable growth of pores.(Alkire et al., 2008)

(Murphy and Michelson, 1962). Four steps involved in the pore growth mechanism of PAA templates are shown in the Figure 2.4, where each step is related with a different growth pore regime. In the stage-a, a constant voltage is applied on the surface of the aluminum, the current decreases with time until the local minimum is reached.

Simultaneously a barrier layer grows on the interface of the electrolyte and aluminum, which is non porous with a homogeneous thickness. In the stage-b, the current increases gradually to a steady point, and pore precursors form on the oxide layer (barrier layer) surface, which can be dissolved in the electrolyte. In the stage-c, the formation of these pore precursors is random, and usually occurs around a defect. Further anodizing and etching results in the growth of pores, and the aluminum is constantly anodized under an electric field, pores are widened, and at the same time the growth of the barrier layer is increasingly stable. In the stage-d, the growth and the dissolution of the oxide layer reach an equilibrium on the electrolyte-oxide interface and oxide-metal interface (O'sullivan and Wood, 1970), the current density is constant. Anodizing conditions determine the current parameters, such as the minimum current value, the rate of current decrease, and the time after which the steady state forms.

2.2 CHARACTERIZATION TECHNIQUES

Several techniques have been used to characterize PAA and nanostructures including metallic and molecular species based on PAA. X-ray diffraction data were used to confirm the amorphous nature of PAA and to derive information that allows an improvement of preparation conditions. In addition, scanning electron microscopy (SEM) was used to characterize the morphology of the nanostructures. Furthermore, the optical properties and energy transfer were recorded by the photoluminescence (PL) spectra. UV-Visible spectra is used to detect the oxygen vacancies in PAA. A standard Vickers micro hardness tester and nanoindentation techniques were used to measure the mechanical properties of the PAA. Wettability properties of PAA membranes were studied using contact angle measurement technique.

2.3 MORPHOLOGICAL ANALYSIS

2.3.1 X-ray Diffraction

The collection of X-ray Diffraction data is the first step in determining the structural properties of any material synthesized. Interaction between matter and x-rays with

suitable wavelengths results in inelastic and elastic scattering of the radiation. It is the elastic scattering from the electrons inside the matter which leads to the observed diffraction of the incident X-ray beam by the sample (Leng, 2009). By recording and analyzing the diffraction pattern, information on the crystal structure of the material is obtained. Although the scattering takes place from individual atoms, the observed patterns can also be explained by assuming that planes of atoms are sources of the scattered radiation waves. In XRD, a collimated beam of X-rays, with a wavelength typically ranging from 0.7 to 2 Å, is incident on a specimen and is diffracted by the crystalline planes in the specimen to give maximum intensity according to Bragg's law and it is illustrated in the Figure 2.5a:

$$n\lambda = 2d\sin\theta \quad (2.3.1)$$

Where n is an integer denoting the order of diffraction, d is the spacing between atomic planes in the crystalline phase and λ is the X-ray wavelength. Bragg's law states that large diffracted intensity takes place only when the phases of the scattered waves differ by an integral multiple of wavelengths ($n\lambda$). When this is the case, the waves sum up leading to constructive interference and a peak is seen in the diffraction pattern. Otherwise, the waves cancel each other out causing destructive interference and a lower intensity is observed.

The intensity of the diffracted X-rays is measured as a function of the diffraction angle and the specimen's orientation. This diffraction pattern is used to identify the specimen's crystalline phase and to measure related structural properties. Generally, Scherrer formula is used to determine the crystallite size and is given below:

$$D = \frac{0.9\lambda}{\beta\cos\theta} \quad (2.3.2)$$

Where D is the crystallite size, λ is the X-ray wavelength, θ is the diffraction angle in degrees, and β (in radians) is the full width at half maxima (FWHM) measured for the corresponding Bragg reflection. In the present study, the average size of the PAA based nanoparticles can be estimated using Scherrer equation. XRD pattern of PAA membranes were carried out using X-ray diffractometer (Rigaku-miniflex-600:Figure 2.5b) to verify the amorphous nature of the PAA and crystalline phases in the PAA based nanostructures. Data were collected using Cu K_{α} radiation ($\lambda = 1.5418\text{\AA}$) in

the diffraction angle (2θ) ranging from 20° - 80° with a scanning rate of 2° per minute. The x-ray tube was operated at 40 kV and 30 mA. The XRD patterns obtained were compared with those of Joint Committee on Powder Diffraction Standards (JCPDS) data to assess the crystalline phases present.

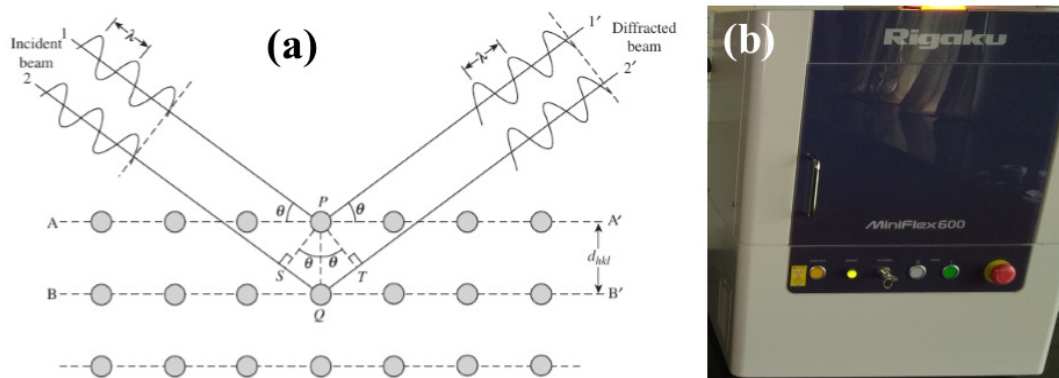


Figure 2.5 (a) Reflection of X-rays from different atomic planes, illustrating Bragg's law, (b) XRD (Rigaku-MiniFlex-600) instrument.

2.3.2 Scanning electron Microscopy (SEM)

The scanning electron microscopy (SEM) is a unique and versatile electron microscopic technique that provides image of a sample providing information about the surface of the specimen at much higher magnification, higher resolution and large depth of focus compared to optical microscopy. SEM uses a focused beam of high-energy electrons to generate a variety of signals at the surface of solid specimens. The signals that derive from electron sample interactions reveal information about the sample including external morphology (texture), chemical composition, crystalline structure and orientation of grains making up the sample. In most applications, data are collected over a selected area of the surface of the sample, and a 2-dimensional image is generated that displays spatial variations in these properties.

Figure 2.6 shows the schematics of a typical SEM instrument. Electron source in SEM produces a finely focused beam of electrons having energy range from a few hundred eV to 30 keV called the primary electron beam. When these electrons strike and penetrate the surface of the sample by passing through two pairs of electromagnetic

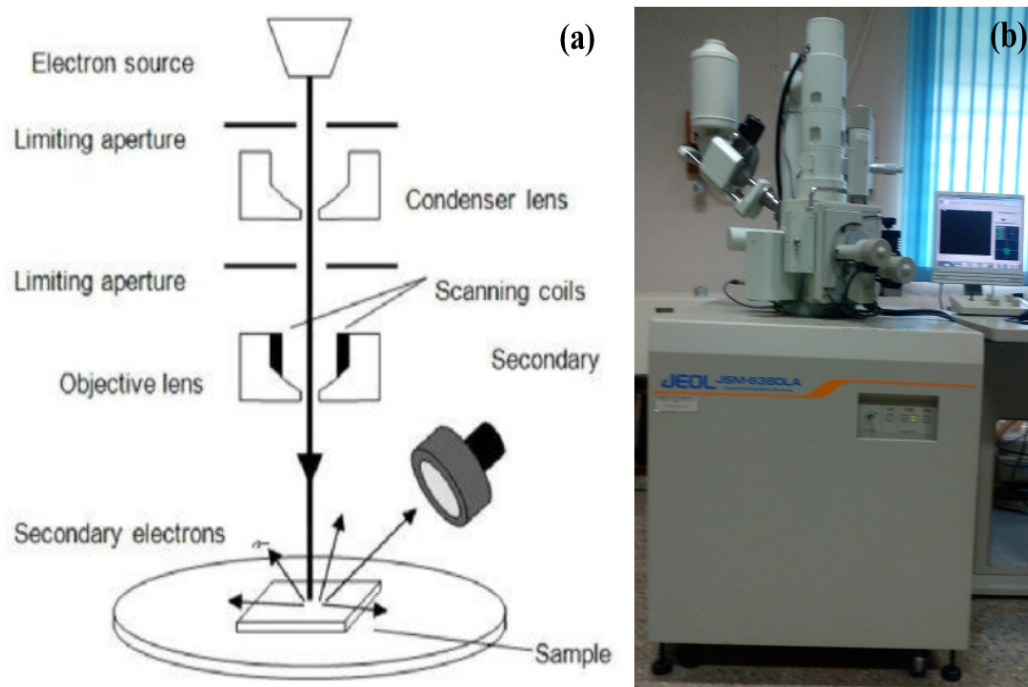


Figure 2.6 (a) Schematic representation of scanning electron microscope, (b) SEM(JEOL-JSM 6380LA) instrument

deflection coils, the emission of secondary electrons (SE) and fewer backscattered electrons (BSE) from the sample surface takes place. A more intense signal is developed by secondary electrons than by the back scattered electrons. This is due to the number of low energy secondary electrons reaching the collector being far greater than the number of back scattered electrons. SEM image can be produced by collecting the emitted secondary electrons on cathode ray tube (CRT) screen and energy dispersive X-ray analysis mode gives qualitative information about the elements present in the probed area of the specimen. The images produced in the SEM are of three types: namely secondary electron images, backscattered electron images and elemental X-ray maps.

In the present work, the surface morphology of the PAA membranes were studied using scanning electron microscopy (SEM-JEOL JSM 6380LA, Japan) and PAA based nanostructures were studied using Field Emission Scanning Electron Microscopy (FE-SEM, ZEISS). In general, the generation of electron beams that is produced by the field emission principle is different from that of an ordinary scanning electron microscope. However, SEM is carried out by rastering a narrow electron beam over the surface and

detecting the yield of either secondary or backscattered electrons as a function of the position of the primary beam. Contrast is caused by the orientation, parts of the surface facing the detector appearing brighter than parts of the surface with their surface normal pointing away from the detector. The secondary electrons have mostly low energies (5-50 eV) and originate from the surface region of the sample. Backscattered electrons come from deeper regions and carry information on the composition of the sample because heavy elements are more efficient scatterers and appear bright in the image.

2.3.3 Energy Dispersive X-ray analysis (EDX)

Energy dispersive X-ray analysis (EDX) is an X-ray technique to identify the elemental composition of materials. The data generated by EDX analysis consists of spectra showing peaks corresponding to the elements making up the true composition of the sample being analyzed. Both Scanning Electron Microscopy (SEM) and Energy Dispersive X-Ray (EDX) analysis can identify and characterize composition of particles, surfaces and more. On using the combination of SEM interfaced with EDX, qualitative information can be obtained on the full elemental composition for the prepared PAA nanostructures.

2.4 OPTICAL ANALYSES

2.4.1 Photoluminescence (PL)

Luminescence is the general name given to the process of spontaneous emission of light by excited atoms in a solid material. One of the ways in which the atoms can be promoted into excited states prior to spontaneous emission is by the absorption of light. Luminescence can thus accompany the propagation of light in an absorbing medium. Fluorescence and phosphorescence are two types of photoluminescence phenomena (Mendham et al., 2006). The physical processes involved in photoluminescence are more complicated than those in absorption. This is because the generation of light by luminescence is tied up with the energy relaxation mechanism in the solid. Further-

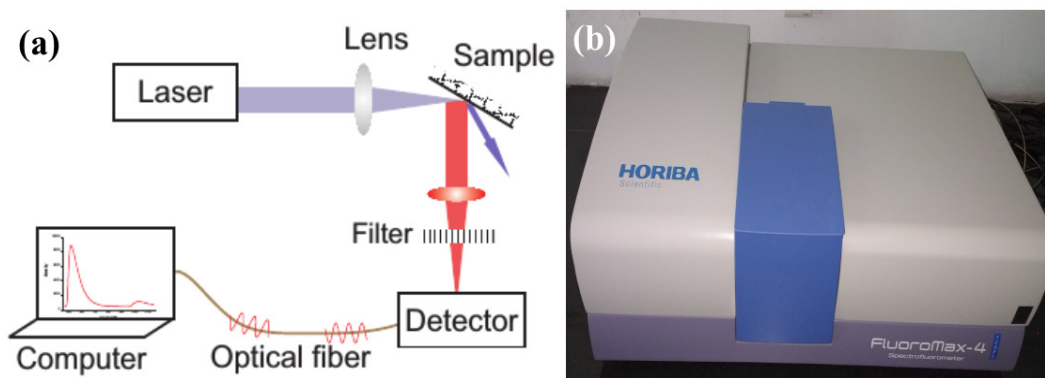


Figure 2.7 (a) Schematic diagram of experimental set-up for PL measurements, (b) PL (FluoroMax-4) instrument.

more, the shape of the emission spectrum is affected by the distributions of electrons and holes within their bands. A photoluminescence experimental arrangement consists of a laser or any other wide range radiation source as an excitation source, a sample holder (sometimes placed inside a crystal for low temperature measurements), suitable lenses for collimation and collection, a scanning spectrometer to record a spectrum and sensitive detector such as photomultiplier tube or charge coupled device (CCD). A schematic diagram of the PL set-up and PL instrument used to analyze PAA membranes is shown in the Figure 2.7. In the present work, PL spectra were studied using FluoroMax-4 fluorescence spectrometer. Throughout PL calculations, the slit width was set as 7 nm and each spectrum was obtained within 1 min. All the calculations were performed at room temperature with an excitation wavelength of 320 nm.

2.4.2 UV-Vis spectroscopy (UV-Visible)

The absorption/ transmission measurements are done to determine the different electronic and optical transitions in the material and its band gap. When an incident light falls on a material a part of it is reflected, a part transmitted and the rest absorbed. The absorption occurs when the energy of the incident photon is absorbed by the electron that is then promoted to a higher energy level. The absorption coefficient of any material can be defined in terms of change in intensity of a monochromatic beam as a function of the distance traversed in the medium:

$$I(\lambda) = I_o(\lambda)e^{-\alpha(\lambda)t} \quad (2.4.1)$$

The absorption coefficient is dependent on the wavelength of the incident light. All

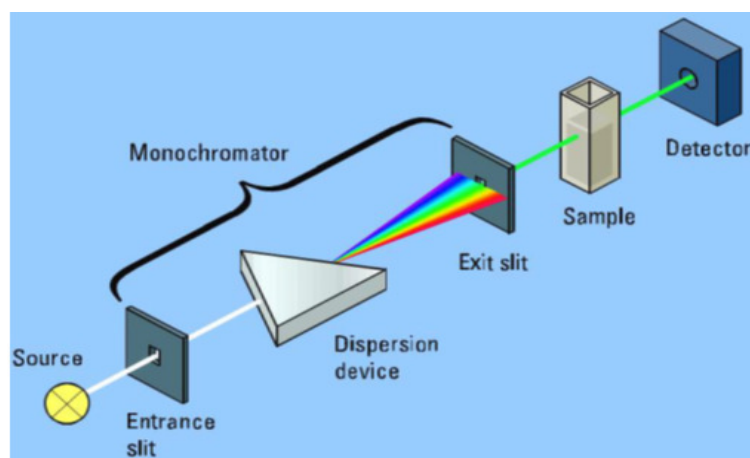


Figure 2.8 Schematic diagram of single beam UV-Visible spectrometer.

the light is transmitted when the energy of the incident beam is less than the energy of available transitions (e.g. transitions associated to the band gap E_g or to a mid-gap states). As soon as the energy of the incident photon is equal to that of a transition, the beam is absorbed by the material. When reflection is negligible, the most common method to determine the absorption coefficient as a function of the wavelength is to measure the transmittance of the film as a function of the wavelength of the incident beam in the optical range of interest. A schematic diagram of single beam UV-Visible spectrometer is shown in the Figure 2.8.

2.4.3 Contactangle measurement

Wettability is the ability of a liquid to maintain contact with a solid surface, resulting from intermolecular interactions when the two are brought together. The degree of wetting (wettability) is determined by a force balance between adhesive and cohesive forces. Contact angle of water droplet (in L) on PAA surfaces was measured using sessile drop technique. This technique constitutes an optical system to capture the profile of water droplet on solid substrate and an angle measuring goniometer. Baselines will be drawn at solid-liquid and liquid-air interfaces. The angle between the intersections of these lines is called contact angle (θ) of the liquid on that solid. The schematic representation is depicted in Figure 2.9. The contact angle provides an indication of how

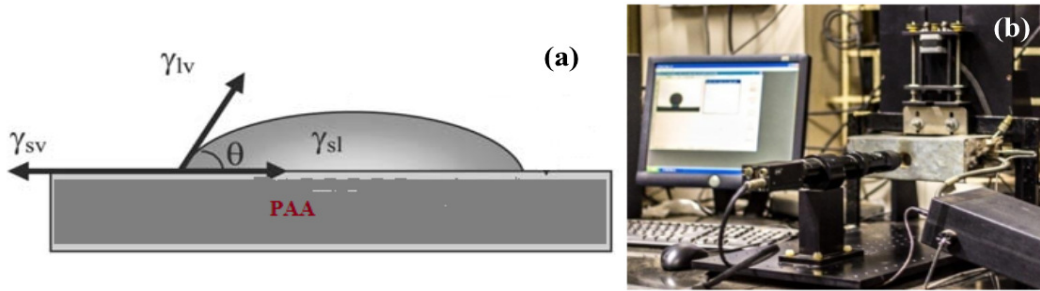


Figure 2.9 (a) Schematic representation of contact angle of liquid drop on solid surface, (b) Contact angle (FTA-200) instrument

effectively a liquid will spread over a surface. The droplet can be formed from a liquid appropriate for the system being tested, for example the contact angle greater than 90° (high contact angle) generally means that wetting of the surface is unfavorable so the fluid will minimize contact with the surface and will form a compact liquid droplet. Contact angles less than 90° (low contact angle) usually indicates that wetting of the surface is very favorable, and the fluid will spread over a large area of the surface. In the case of a liquid (L) drop forming a contact angle (θ) on a solid (S) surface, the surface free energy (SFE) can be obtained using Youngs equation (Rudawska and Jacniacka, 2009) represented by

$$\gamma_s = \gamma_{SL} + \gamma_L \cos \theta_{LS} \quad (2.4.2)$$

Where γ_s is the SFE of a solid, γ_{SL} the SFE corresponding to the solid-liquid interface, γ_L the SFE of a measuring liquid. Further Youngs - Dupre equation is given by

$$\gamma_{SL} = \gamma_s + \gamma_L - 2 \quad (2.4.3)$$

Using the above two equations the surface energy of the PAA membrane was measured. The contact angle of water on the PAA membranes has been determined using a dynamic contact analyzer (FTA-200 First ten angstroms). The effect of anodization duration and pore widening duration on wetting properties of PAA membranes were studied in the present work.

2.5 MECHANICAL ANALYSIS

Mechanical properties of PAA membranes including Youngs modulus (E) and hardness (H) were studied. Indentation is a simple technique used often to obtain these

parameters of brittle solids. Indentation involves applying a load to hard tip of known mechanical properties (diamond) and measuring the area or depth. H could be defined as the measure of resistance of the materials surface to penetration by hard indenter. Harder the material, penetration would be lesser and gives a small residual area. Different types of indenters are available like spherical, canonical and pyramid. Analytical models have been developed to extract the hardness and other parameters. Pyramid indenters are used for micro and nano indentation experiments. Four sided diamond pyramid indenter is called Vickers indenter whereas three sided one is called Berkovich indenter. Both of them have the same projected area-to-depth ratio.

2.5.1 Microindentation

In micro indentation, prescribed load is applied to the indenter in contact with the specimen for a finite time (1 - 2 min.). It leaves residual impression on the specimen surface after load is removed and the area of the impression is obtained using an optical microscope. In micro indentation, size of the indenter is comparable to that of microstructural features. It enables one to obtain relative hardness of various micro constituents of the sample. Vickers hardness measures the resistance of the specimen to permanent deformation due to a constant compression load from a sharp indenter as shown in Figure 2.10a. It is calculated by dividing the indentation load by the surface area of the remaining indentation after unloading. The conventional Vickers hardness of the PAA membranes were measured using a Vickers hardness testing machine. Vickers hardness is estimated from the following equation (Fang et al., 2007)

$$H_v = 1.854 \frac{P_{max}}{d^2} \quad (2.5.1)$$

Here P_{max} , H_v and d represent the indentation load (0.98N), Vickers hardness in GPa and half of the average length of two diagonals, measured with a precision of 0.1 μ m. Generally speaking, hardness depends strongly on both elastic deformation and plastic deformation (Yamane and Mackenzie, 1974). In the present work, hardness of PAA membranes formed in oxalic and sulphuric acid as electrolytes was examined by Vickers diamond pyramid indentation technique (Clemex micro hardness tester, MMT

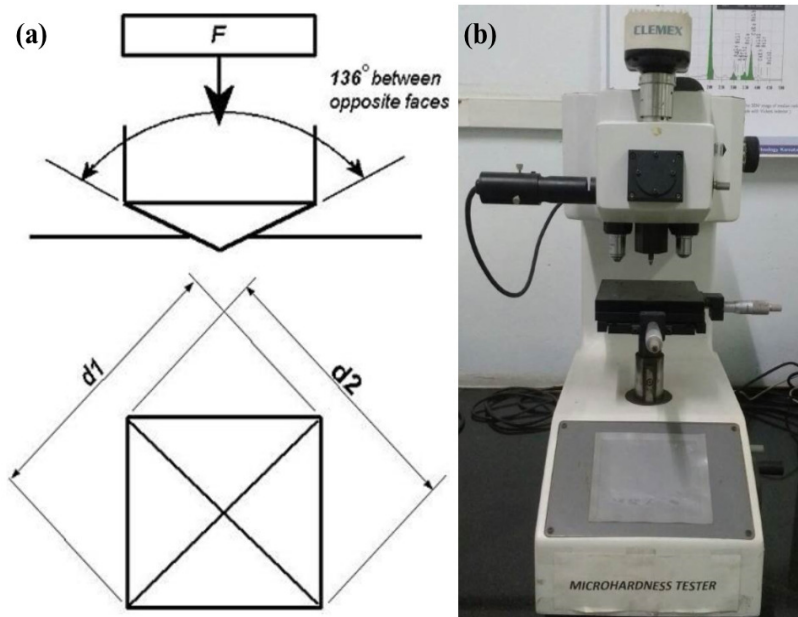


Figure 2.10 (a) Schematic Diagram of Vickers indenter and (b) Clemex micro hardness tester.

X7, Matsuzawa Seiki Corp., Japan) by applying loads of 0.98 N and 9.8 N. The duration of test force was maintained for 10 s. Microhardness of PAA membranes were carried out using the Clemex micro hardness tester was shown in the Figure 2.10b.

2.5.2 Nanoindentation

Nanoindentation is also called depth sensing or instrumented indentation. Here depth of the indenter is measured as the load is applied to it. The area is calculated using the depth at full maximum load applied and taking the known geometrical values of nano pyramid indenter into account. The load-unload vs. depth curve and its shape enables one to calculate the elastic modulus. Schematic load/unload displacement curve for a non-flat indenter (Vickers or Berkovich) in a nanoindentation experiment is shown in Figure 2.11. The elastic deflection (h_{el}) of the anodic alumina at the maximum load with negligible of pile-up is measured using Oliver and Pharr formula (Oliver and Pharr, 2004).

$$h_{el} = \epsilon \frac{P_{max}}{S} \quad (2.5.2)$$

Here ε is a constant that depends on the geometry of the indenter and $\varepsilon = 0.75$ for Berkovich indenter. Hardness is measured using the following equation:

$$H_v = \frac{P_{max}}{A_{real}} \quad (2.5.3)$$

Here A_{real} is the real contact area. The Young's modulus (E) of the PAA structures can be estimated by (Ko et al., 2006),

$$E = (1 - \nu^2) \left[\frac{1}{E^*} - \frac{(1 - \nu_i^2)}{E_i} \right]^{-1} \quad (2.5.4)$$

Here ν represents the Poisson's ratio, E_i and ν_i are Young's modulus and Poisson's ratio of the indenter. For a diamond tip, $E_i = 1140$ GPa, and $\nu_i = 0.07$, respectively and the Poisson's ratio of PAA structures is 0.22. The elastic modulus (E^*) related to the contact area (through the stiffness constant (S) is given by (Ko et al., 2006),

$$E^* = \frac{\sqrt{\pi}}{2} \frac{S}{\beta \sqrt{A_{real}}} \quad (2.5.5)$$

Here $S = dP/dh$ indicates the stiffness of the test material, β represents the shape constant of the indenter and 1.034 for the Berkovich tip. Nanoindentation of PAA mem-

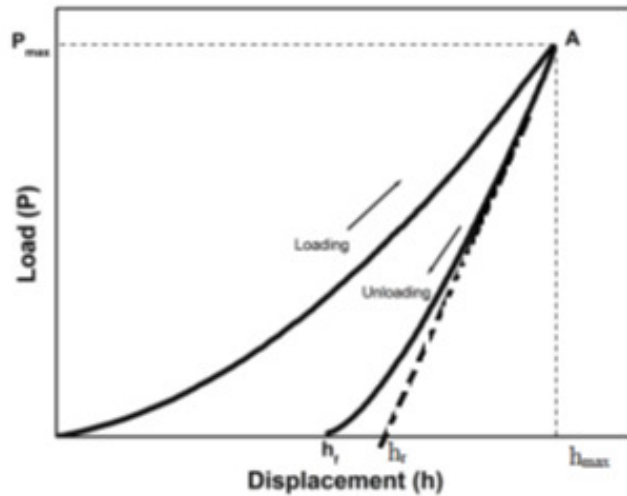


Figure 2.11 Typical load/unload vs. displacement curve for a solid with non-flat indenter. Here P_{max} is maximum load applied to the indenter, h_{max} is the displacement or depth at maximum load and h_f is the depth after complete unloading.

branes was measured using Berkovich nano indenter (Hysitron Inc Minneapolis USA, TI-900) with a maximum load of 10 mN associated with a loading and unloading rate of 0.4 mN/s (resolution of force was 1 nN). Ten indents were taken on each specimen. Nanoindentation measurements of PAA membranes were carried out at Industrial research and consultancy center (IRCC), IIT Bombay.

Chapter 3

FABRICATION OF POROUS ANODIC ALUMINA MEMBRANES: OPTIMIZATION OF GROWTH PARAMETERS

This chapter provides a set of optimization conditions for growth of highly ordered porous anodic alumina (PAA) membranes. Influence of anodization parameters such as anodization duration and electrolyte concentration on the growth mechanism of PAA membranes were studied in detail. Also, it discusses the nanopore arrangement of PAA membranes using 2D fast Fourier transform analysis.

3.1 INTRODUCTION

In general, porous anodic alumina (PAA) membranes were prepared by two-step anodization process. During second-step anodization of Al, the pores are preferentially nucleated at concaves and grooves on the surface, where the local electric field appears to be higher (Poinern et al., 2011), (Li et al., 1998). Therefore it is important to ensure large areas on the Al surface which are flat and microscopically smooth (free from trenches, hillocks, etc.). In order to ensure good pore ordering and surface quality of the final PAA membranes, standard pretreatments are employed, such as thermal annealing and electropolishing. Thermal annealing of Al foils allows formation of large grains and wide flat areas on the surface of Al (Masuda et al., 1997). Electropolishing removes protruding features from the Al surface; in the case of optimal process parameters it allows formation of very smooth surface on a big scale (Rauf et al., 2009), (Ma

et al., 2009). For thin (a few hundreds of nanometers) Al films such pretreatments are not applicable. Annealing of such films at high temperatures leads to the growth of hillocks (Ericson et al., 1991); electropolishing might remove too much material from the film and even dissolve it completely. Thus, the preferred way of improving the surface quality of thin Al films is the careful control over the deposition parameters which influence the film microstructure and surface morphology. Structural aspects of PAA, such as pore diameter and interpore distance depend on the operating conditions such as the nature of the electrolyte, anodization potential and anodization process duration. Studies have shown that with increasing anodizing potential, both pore diameter and inter-pore spacing increase linearly (Chowdhury et al., 2011). The familiar methods for the structural analysis of PAA membranes involves the study of the fast Fourier transform (FFT) analysis of scanning electron microscope (SEM) images (Sulka and Parkola, 2007) of PAA.

3.2 RESULTS AND DISCUSSION

3.2.1 Effect of anodization duration

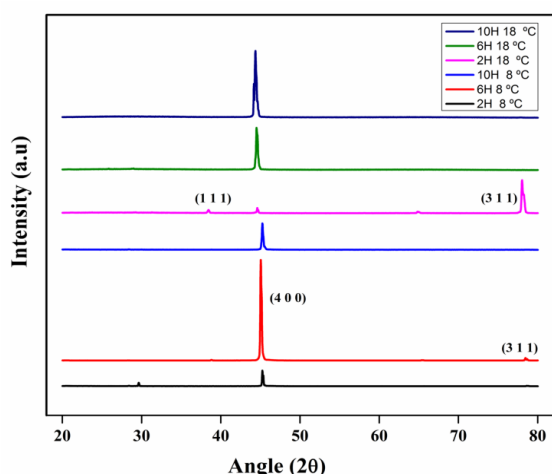


Figure 3.1 XRD pattern of PAA membranes with Al substrate at 8 °C and 18 °C

To study the effect of anodization duration on the structural aspects of PAA membranes, anodization was performed at two temperatures, namely 8 °C and 18 °C. At each temperature, five PAA membranes were prepared at various anodizing durations,

such as 2h, 4h, 6h, 8h and 10h. XRD analysis of PAA membranes prepared at anodization temperatures 8 °C and 18 °C were shown in the Figure 3.1. The diffraction pattern confirms the amorphous nature of alumina along with the peaks related to the aluminium substrate (Choudhari et al., 2012). All of these membranes exhibit a high-

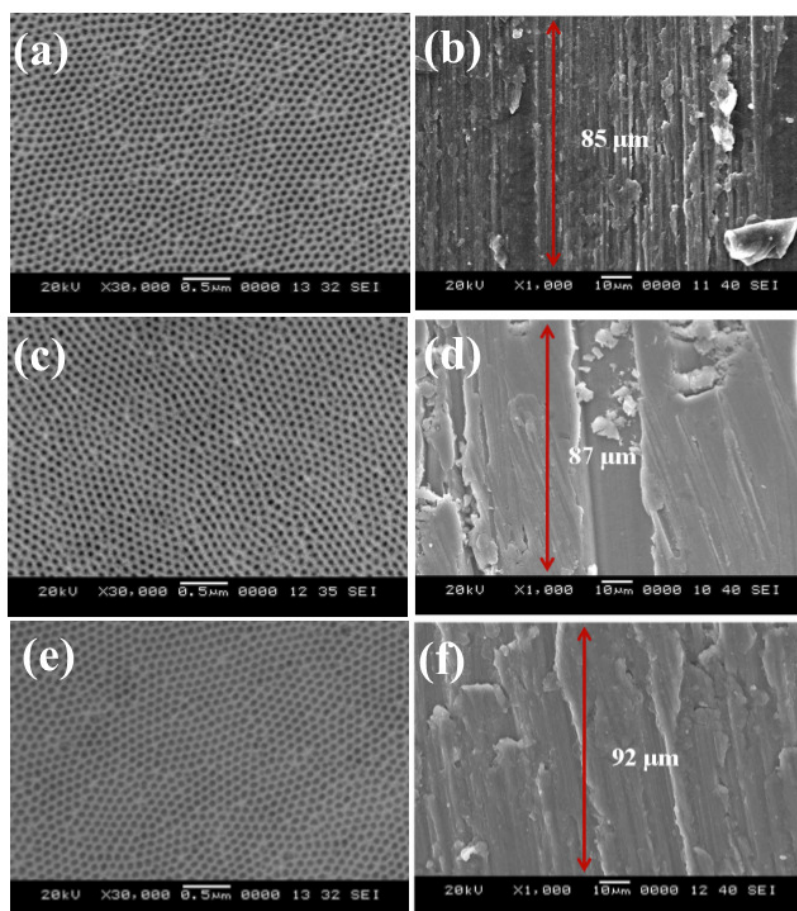


Figure 3.2 SEM top-view micrographs (a, c and e), their cross-sectional images (b, d and f) of PAA membranes formed in 0.3 M oxalic acid at 8 °C at different anodization durations such as 2 h, 6 h and 10 h for both steps.

intensity peak in the 2θ range 45.76° , which is a characteristic of anodic aluminium oxide (400) and matches with JCPDS data (02-1421). PAA membranes obtained with 6h anodization at 8 °C and with 2h anodization duration at 18 °C showed XRD peaks at 78.44° and 38.61° related to Al, corresponding to (311), (111) planes respectively and match with JCPDS data (01-1180). The Energy dispersive X-ray spectroscopy (EDX) analysis of the PAA membranes at 8 °C and 18 °C was carried out and tabulated in Table 3.2.1, indicating the presence of oxygen and Al elements. It was observed from EDX of

PAA membranes, that for 2h anodization duration at 18 °C, the Al atomic percentage is higher compared to those PAA membranes obtained with other anodization durations. As can be seen from the Table 3.2.1, it was observed that, with increasing anodization duration, there was a decrease in oxygen atomic percentage when synthesized at 8 °C and increase for that which was synthesized at 18 °C. In contrast, Al atomic percentage increased with increasing anodization duration at 8 °C and it decreased at 18 °C. Typical SEM top-view micrographs of the PAA membranes grown at 8 °C and 18 °C with anodization potential of 40 V were shown in Figure 3.2 (a, c and e) and Figure 3.3 (a, c

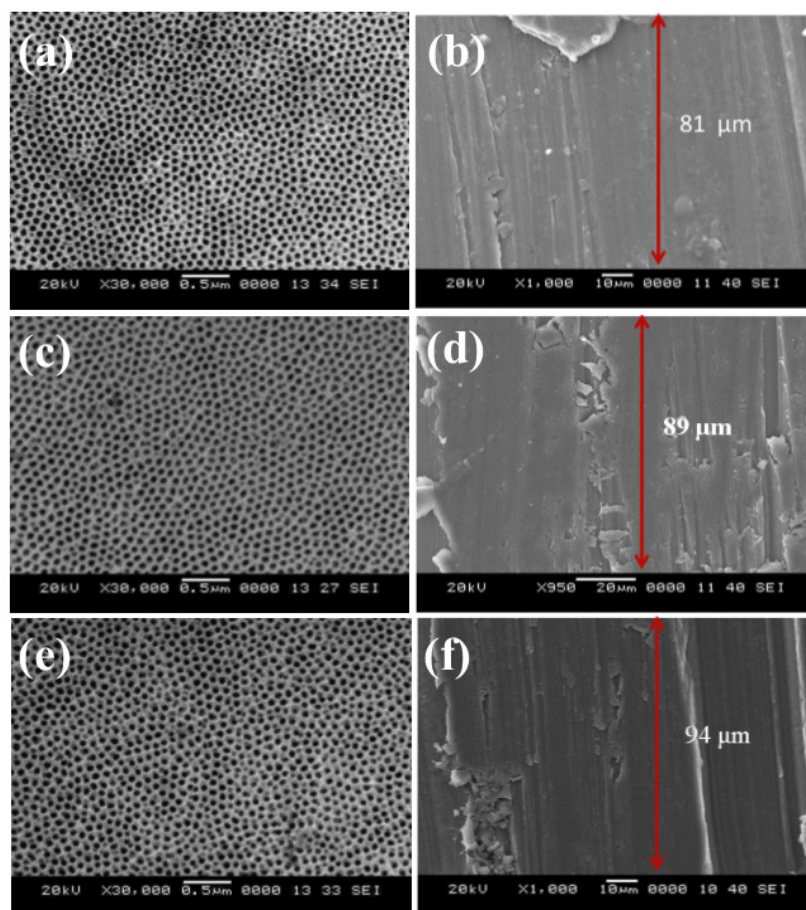


Figure 3.3 SEM top-view micrographs (a, c and e), their cross-sectional images (b, d and f) of PAA membranes formed in 0.3 M oxalic acid at 18 °C at different anodization durations such as 2 h, 6 h and 10 h for both steps.

and e). In all these cases, thick and hexagonally organized pores were observed. Larger pore dimensions were observed when anodization was performed at 18 °C. These observations are also in agreement with the reported values (Stepniowski and Bojar, 2011).

Further, it was observed that the PAA growth rate varied with the anodization duration. Figure 3.2 (b, d and f) and Figure 3.3 (b, d and f) shows the cross-sectional images of PAA membranes prepared at 40 V under 8 °C and 18 °C respectively. These SEM micrographs directly give the pore depth, i.e., PAA film thickness, 85, 87, 92 μm for 2, 6, 10h at 8 °C and 81, 89, 94 μm for 2, 6, 10h at 18 °C respectively. With increasing anodization duration, the thickness of PAA membranes increased from 85 μm to 92 μm at 8 °C and from 81 μm to 94 μm at 18 °C. This is due to the fact that, the oxide growth rate increases with increasing anodization time (Stepniowski et al., 2014c). In the Figure 3.2 and Figure 3.3 SEM micrographs of PAA membrane pores were asymmetrical, however the fast Fourier transforms and their radial averages allow estimation of the pore arrangement.

Table 3.2.1 SEM EDX data of PAA membranes prepared under different anodization durations at 8 °C and 18 °C

Element	2h 8 °C	6h 8 °C	10h 8 °C	2h 18 °C	6h 18 °C	10h 18 °C
	(At%)	(At%)	(At%)	(At%)	(At%)	(At%)
O_2	54.06	52.24	52.88	50.68	53.58	53.90
Al	45.94	47.76	47.12	49.32	46.42	46.10

3.2.2 Effect of electrolyte concentration

Figure 3.4 shows the typical XRD analysis of the free standing PAA membranes produced using oxalic acid in different electrolyte concentrations (0.1-0.9 M). All the membranes provide a similar response to XRD measurements and no sharp diffraction peaks were observed from any specific crystallographic plane of the PAA. Therefore, XRD patterns in Figure 3.4 clearly show that the prepared alumina membranes were amorphous (Khan et al., 2013). A small peak was observed in PAA at an angle 26.3°, related to carboxyl impurities (carbon content), which occurs in the growth of alumina, and this correspond to (1 1 1) plane matching with JCPDS data (75-0444). Figure 3.5 shows the top view SEM micrographs (0.1-a, 0.3-c, 0.5-e, 0.7-g, and 0.9-i) of the PAA fabricated using oxalic acid by varying electrolyte concentration from 0.1 to 0.9 M under a constant anodization potential of 40 V. It was observed that, the concentration of oxalic acid has significant influence on the morphology and regularity of the pore arrange-

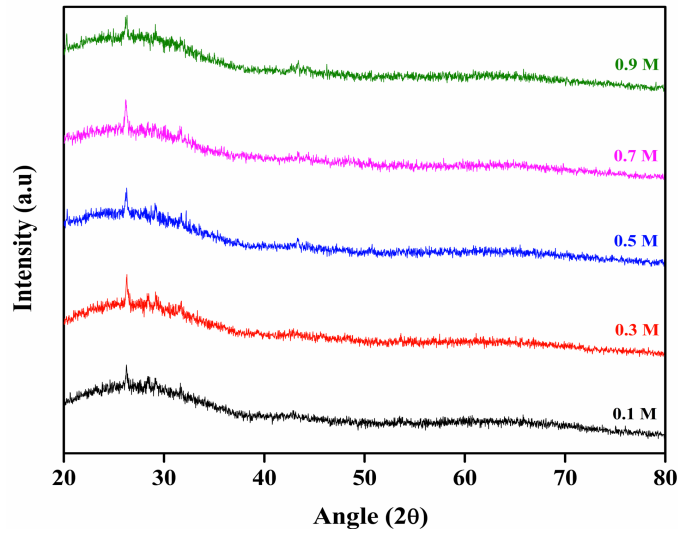


Figure 3.4 XRD pattern of the PAA obtained at different electrolyte concentration (0.1-0.9 M)

ment. When the electrolyte concentration was 0.1 M, the orientation and organization of the cells were not in a uniform order. The hexagonal shape was distorted and pores were not circular. As the concentration of the electrolyte increases from 0.1 to 0.3 M, pore arrangement and cell organization improved considerably. Further, when the concentration was increased to 0.7 and 0.9 M, the hexagonal pore array was retained, but long-range order was disturbed. This can be attributed to growth rate and volume expansion of aluminium oxide that increased with the increasing electrolyte concentration (Voon and Derman, 2013). Cross-sectional images (0.1-b, 0.3-d, 0.5- f, 0.7-h and 0.9 M-j) of the PAA at different electrolyte concentrations were shown in the Figure 3.5 and these results show that oxide layer thickness increases with the concentration of oxalic acid for 0.1 and 0.3 M electrolytes. In order to obtain relevant structural parameters, the alumina layer thickness and growth rate of PAA were obtained by the following equations (Senbahavalli et al., 2016)

$$\text{Thickness} = \frac{W_2 - W_1}{\text{Density of aluminium}} \times \text{Specimen area} \quad (3.2.1)$$

where W_1 and W_2 represents the weights of the specimen before and after anodization.

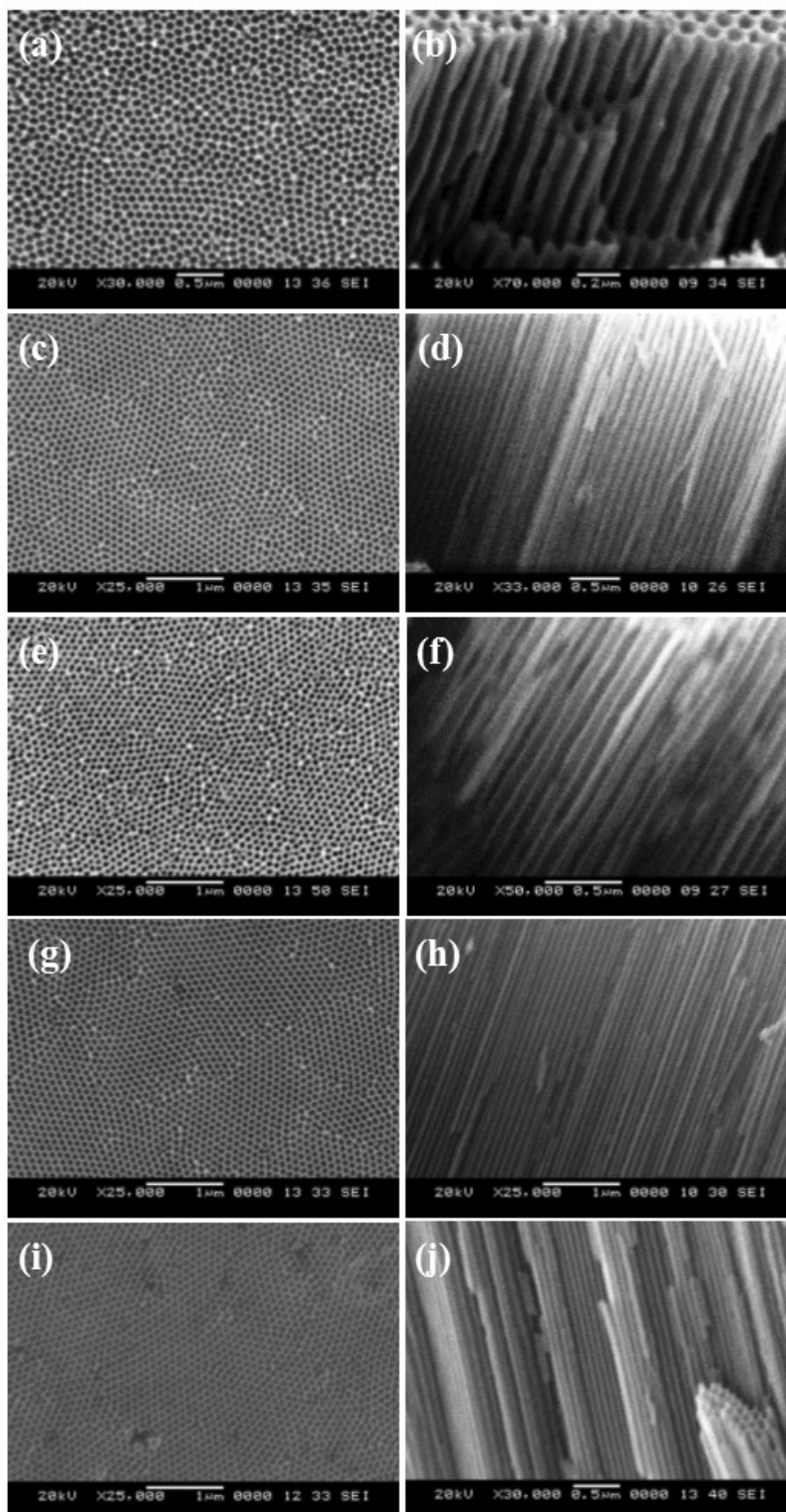


Figure 3.5 SEM top-view micrographs (a, c, e, g and i), their cross-sectional images (b, d, f, h and j) of PAA membranes formed in 0.3 M oxalic acid at 18 °C at different electrolyte concentrations such as 0.1, 0.3, 0.5, 0.7 and 0.9 M.

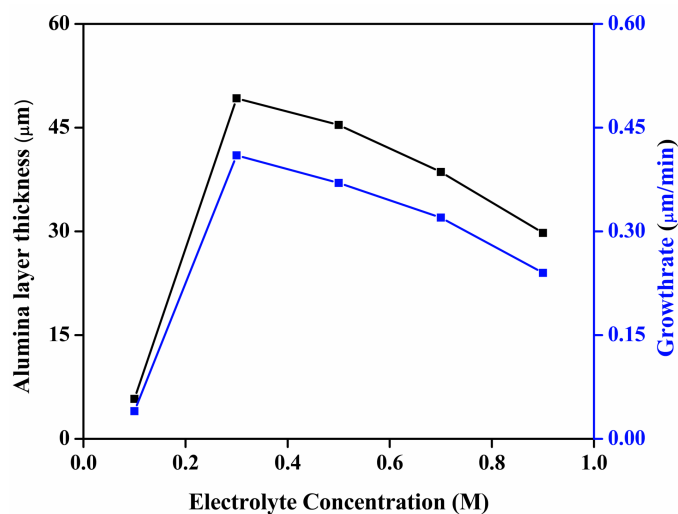


Figure 3.6 Thickness and growth rate as a function of electrolyte concentration for PAA obtained at 0.1 to 0.9 M.

$$\text{Growth rate} = \frac{\text{Thickness}}{\text{Anodization time (min)}} \quad (3.2.2)$$

Effect of electrolyte concentration on the formation and properties of PAA was studied by varying the concentration between 0.1 and 0.9 M under a constant potential of 40 V for second step anodization duration of 2h. The thickness and growth rate as a function of electrolyte concentration was shown in the Figure 3.6. In this study, the maximum thickness ($49.25 \mu\text{m}$) and growth rate ($0.41 \mu\text{m}/\text{min}$) was observed for 0.3 M oxalic acid. This is due to the inner movement of oxygen (O^{2-}) or hydroxide ions (OH^-) towards the Al/oxide interface that increased with increasing the electrolyte in the electrolytic bath. These anions react with the cations (Al^{3+}) that are moving outwards from the Al surface. It was noticed that the thickness and growth rate of PAA decreased, on further increasing the electrolyte concentration from 0.4 to 0.9 M. This is because of more amount of hydroxide ions are produced in the electrolytic bath which acidified the electrolyte near the anodic area. Based on these results, it was concluded that highly ordered uniform porous membranes could be obtained by 0.3 M of oxalic acid at 40 V for an optimum second step anodization duration of 120 min. The thickness and growth rate data of all PAA were tabulated in Table 3.2.2.

Table 3.2.2 Thickness and growth rate data of PAA membranes obtained at different electrolyte concentrations (0.1-0.9 M)

PAA (M)	Thickness (μm)	Growth rate($\mu m/min$)
0.1	5.78	0.04
0.3	49.25	0.41
0.5	45.4	0.37
0.7	38.59	0.32
0.9	29.77	0.24

3.3 PORE PARAMETERS (D_p , D_i , α and n)

A complete study of the structural features of PAA membranes was performed using SEM micrographs. All collected measurements of the interpore distance and pore diameters calculated from SEM top-view micrographs for different anodization duration processes were divided into seven systems covering the whole series. Figure 3.7 and Figure 3.8 show the distribution images of the interpore spacings (D_i) and pore diameter (D_p) determined from SEM top-view micrographs. The major part of the PAA membrane shows the pore diameter among 61 nm to 69 nm at 18 °C and 64 to 73 nm at 8 °C. Alternatively, the interpore spaces are in the range of 103.5 to 100.2 nm at 8 °C and 104 to 100.1 nm at 18 °C. Additionally, pore density and porosity were calculated using data obtained from Image-J analysis software. The effect of anodization duration on pore diameter and interpore spaces of nanoporous alumina obtained by anodization at 8 °C and 18 °C is shown in Figure 3.9. It was observed that the anodization duration affects the pore diameter and linear associations between the pore diameter and anodization duration (Figure 3.9).

A slight decrease of the interpore distance was noticed with an extension of the anodization duration. This was caused by the increase in the uniformity of pore structure array with the increase of the anodization duration (Zaraska et al., 2009). A gradual improvement in the regularity of the pore system to the perfect hexagonal array is observed with increasing duration of anodization time. The average pore diameter of anodic alumina was calculated by taking 1000 pores from each SEM micrographs for various anodizing durations. Figure 3.9a shows the distribution diagram of anodization

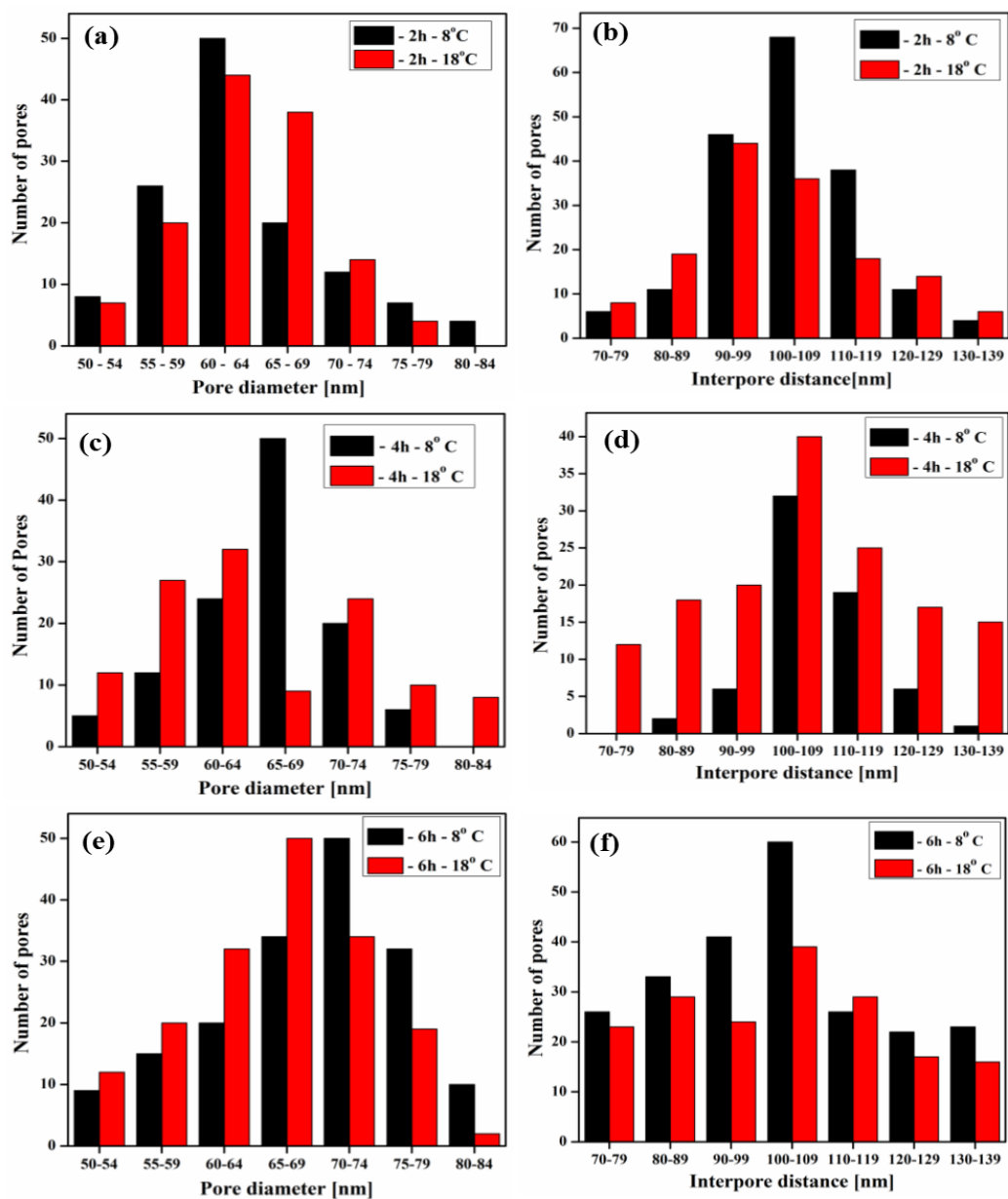


Figure 3.7 Pore diameter and inter pore distance distribution of PAA membranes prepared for different anodization durations, 2h (a) pore diameter (b) inter pore distance, 4h (c) pore diameter (d) inter pore distance and 6h (e) pore diameter (f) inter pore distance at 8 °C and 18 °C.

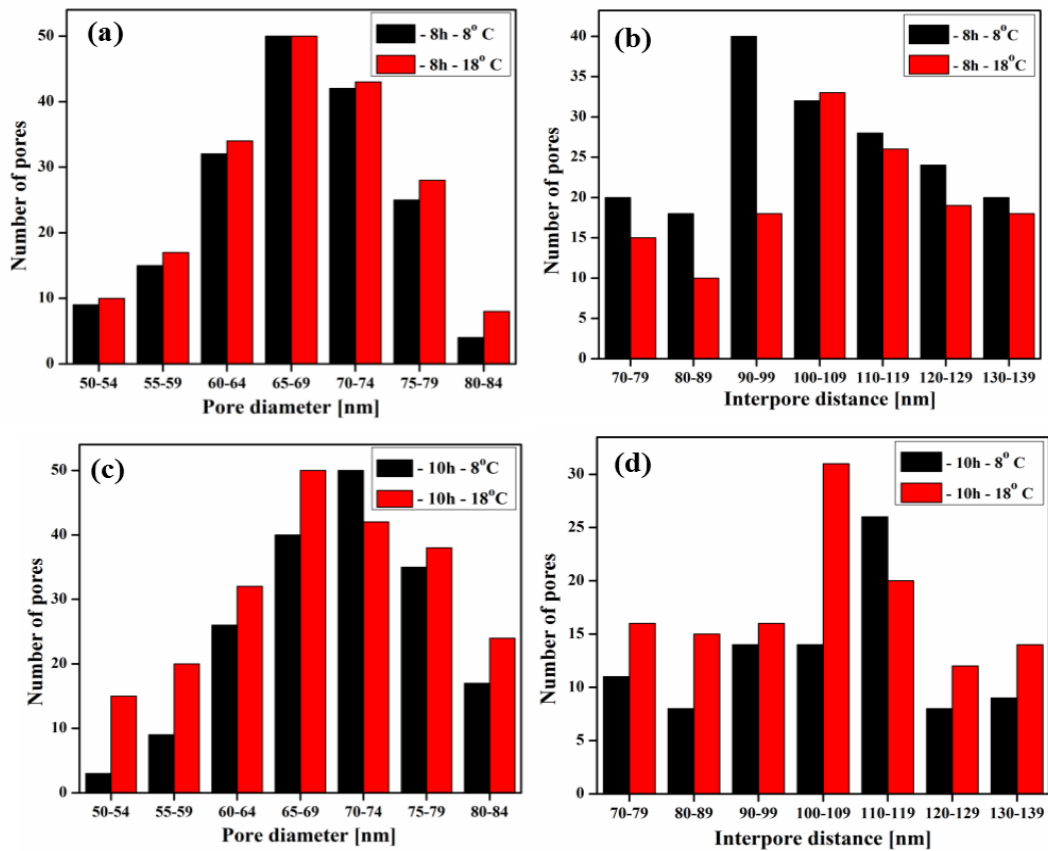


Figure 3.8 Pore diameter and inter pore distance distribution of PAA membranes prepared for different anodization durations, 8h (a) pore diameter (b) inter pore distance and 10h (c) pore diameter (d) inter pore distance at 8 °C and 18 °C

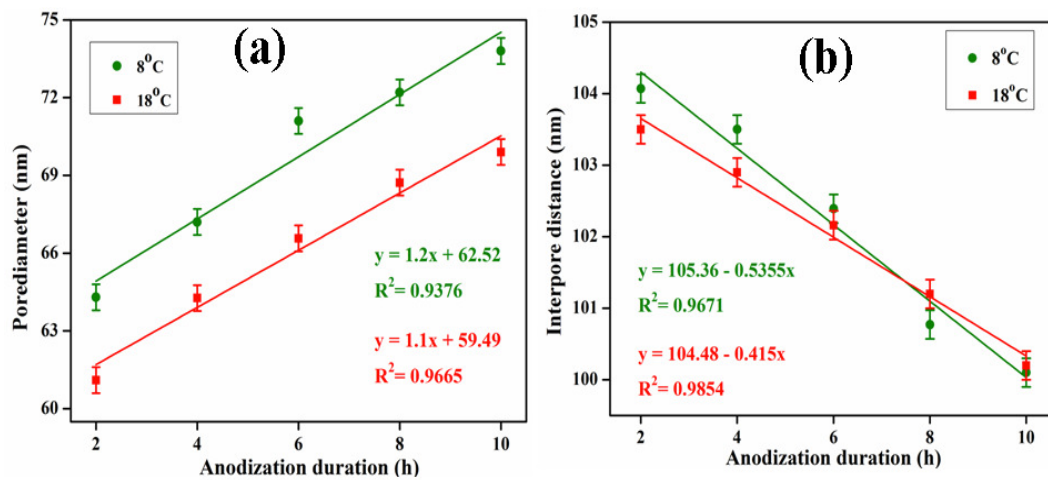


Figure 3.9 The influence anodizing duration on the pore diameter (a) and inter pore distance (b) of porous anodic alumina films formed in 0.3M $H_2C_2O_4$ for 2h, 4h, 6h, 8h and 10h at 8 °C and 18 °C

duration with the pore diameter (D_p , eq.no 1.4.1) of PAA membranes formed in 0.3M $H_2C_2O_4$ at 2h, 4h, 6h, 8h and 10h at 8 °C and 18 °C. It was observed that the pore diameter is linearly dependent on anodizing time. The effect of anodizing duration on the interpore distance (D_i , eq.no 1.4.2) of porous anodic alumina formed in 0.3M oxalic acid at different anodization durations at 8 °C and 18 °C was shown in Figure 3.9b. It was found that interpore distance linearly decreased with the increase of anodization duration. The average interpore distance of PAA membranes prepared for 2h, 4h, 6h, 8h and 10h using two-step anodization process was estimated from SEM top-view images. However, it may be noted that a little lower (D_i) values were noticed for the anodization performed at 18 °C. The structural data of PAA membranes were given in Table 3.3.1, Table 3.3.2, Table 3.3.5 for 8 °C and Table 3.3.3, Table 3.3.4 Table 3.3.6 for 18 °C. The other important aspects often used for the explanation of structural characterization of porous anodic alumina are the wall thickness (W , eq.no 1.4.3) and the barrier layer (B , eq.no 1.4.5) thickness.

The dense behavior of the barrier layer indicates the direct electrochemical deposition of metals into the pores of PAA templates. For all the anodized samples, these results were recorded in Table 3.3.5 and Table 3.3.6. The data in Table 3.3.5 show that neither W nor B depends considerably on the anodization duration. Figure 3.10a, 3.10b show the variation of barrier layer thickness and wall thickness with anodization duration. Increase of the thickness of W and B was noticed at high temperature as a result of the advanced field-assisted dissolution of aluminum oxide at the oxide/electrolyte interface. Production of a porous aluminum oxide layer using self-organized two-step anodization of aluminum results in PAA membranes with the dielectric oxide film at the pore bottoms, this barrier layer elimination is regarded as a significant step towards the creation of a through-hole porous template for nanofabrication (Lee et al., 2006). Owing to the fact that the interpore distance (D_i) is directly related to the anodizing potential, the pore density (n) should increase with increasing anodization duration. As can be noticed, these results show that pore density increases with increasing anodizing duration (Figure 3.11a) for all the temperatures which we have investigated. The effect of anodization duration on the porosity (α , eq.no 1.4.4) of PAA membranes fabricated

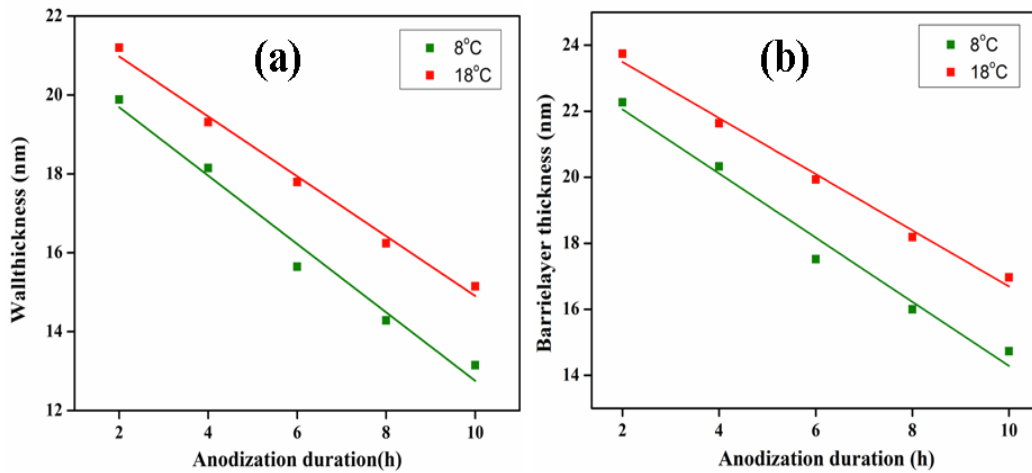


Figure 3.10 The influence anodizing duration on the wall thickness (a) and barrier layer thickness (b) of porous anodic alumina films formed in 0.3M $H_2C_2O_4$ for 2h, 4h, 6h, 8h and 10h at 8 °C and 18 °C

by a two-step anodization process in 0.3M oxalic acid for 2h, 4h, 6h, 8h and 10h at 8 °C and 18 °C is shown in Figure 3.11b. The results in Figure 3.11b show that the

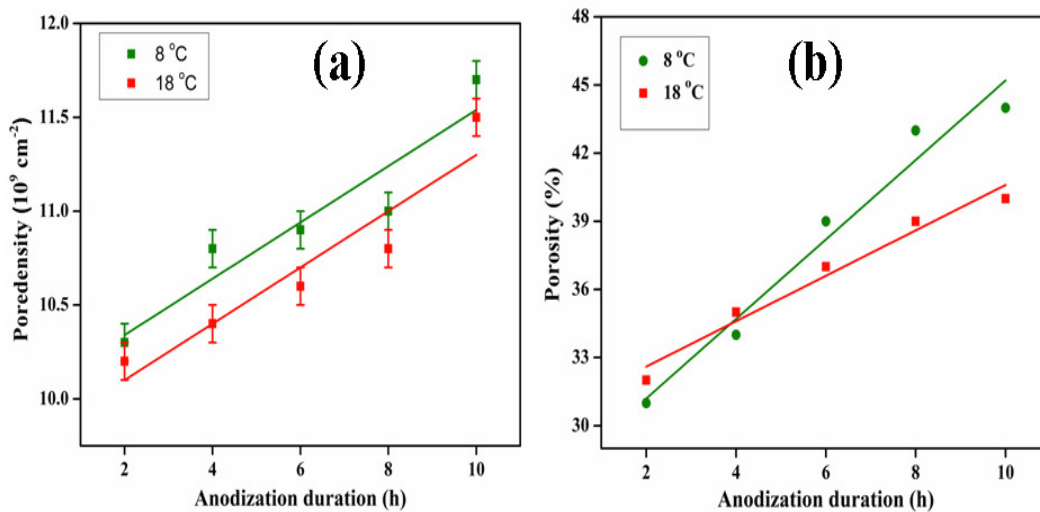


Figure 3.11 Anodizing duration influence on the pore density (a) and porosity (b) of porous anodic alumina films formed in 0.3M $H_2C_2O_4$ for 2h, 4h, 6h, 8h and 10h at 8 °C and 18 °C

porosity of anodic alumina increases with increasing anodization duration, when anodizing was carried out for 2h to 10 hours. The porosity decreases from 42% to 39% with increasing anodizing temperature from 8 °C to 18 °C for 10h duration. The pore diameter increases with the duration of the anodization process and it may be due to the

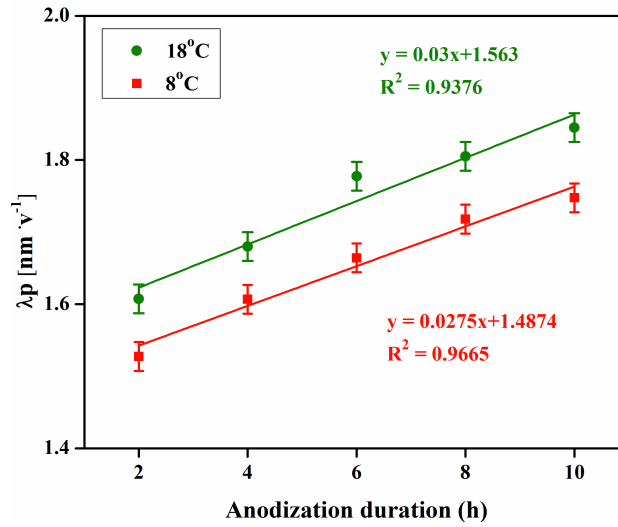


Figure 3.12 Effect of the anodization duration on the proportionality constant λ_p between the pore diameter and applied anodizing potential.

continual chemical action of the electrolyte on the Al_2O_3 . Alumina was dissolved by the acidic electrolyte and longer contact of the PAA with oxalic acid results in highly developed alumina utilization by the electrolyte. At higher temperature, the rate of reaction between pore walls and the electrolyte is enhanced. Further, it may be pointed out that the proportionality constant (λ_p) is linearly dependent on the temperature and for the longer anodizing duration the slope of the curve rises significantly. For anodization carried out for 2h to 10h, λ_p varies from 1.6 to 1.8 at 18 °C and 1.5 to 1.7 at 8 °C as shown in Figure 3.12. The proportionality constant data for all these PAA membranes were tabulated in Table 3.3.5 and Table 3.3.6.

Table 3.3.1 Pore diameter and interpore distance of PAA membranes using SEM micrographs and the software Image-J, for different anodization durations carried out in 0.3 M oxalic acid at a temperature of 8 °C.

Sample	Duration (h)	Pore diameter (nm)		Interpore distance (nm)	
		SEM	Image-J	SEM	Image-J
A1	2	72±6	63 ± 4	107±6	101±7
A2	4	64±5	62±5	102±5	103±5
A3	6	67±7	66±4	101±5	102±4
A4	8	65±7	68±5	103±7	106 ±5
A5	10	63±6	69±5	100±8	104±5

Table 3.3.2 Porosity and Pore density of PAA membranes using the SEM micrographs and the software Image-J, for different anodization durations carried out in 0.3 M oxalic acid at a temperature of 8 °C.

Sample	Duration (h)	Porosity (%)		Pore density ($10 \times 10\text{cm}^{-2}$)	
		SEM	Image-J	SEM	Image-J
A1	2	40	35	1.00	1.13
A2	4	35	32	1.10	1.08
A3	6	39	37	1.13	1.10
A4	8	36	37	1.08	1.02
A5	10	35	39	1.15	1.06

Table 3.3.3 Pore diameter and interpore distance of PAA membranes using the SEM micrographs and the software Image-J, for different anodization durations carried out in 0.3 M oxalic acid at a temperature of 18 °C.

Sample	Duration (h)	Pore diameter (nm)		Interpore distance (nm)	
		SEM	Image-J	SEM	Image-J
A1	2	62± 4	61 ± 5	101 ±7	104±6
A2	4	70±5	67±4	103±4	108±5
A3	6	74±4	71±5	105±5	102±4
A4	8	67±7	70±5	104±7	101 ±5
A5	10	70±5	71±5	100±8	103±4

Table 3.3.4 Porosity and Pore density of PAA membranes using the SEM micrographs and the software Image-J, for different anodization durations carried out in 0.3 M oxalic acid at a temperature of 18 °C.

Sample	Duration (h)	Porosity (%)		Pore density ($10 \times 10\text{cm}^{-2}$)	
		SEM	Image-J	SEM	Image-J
A1	2	34	31	1.13	1.06
A2	4	37	34	1.08	0.98
A3	6	44	43	1.04	1.10
A4	8	37	43	1.06	1.13
A5	10	44	42	1.15	1.08

Table 3.3.5 Barrier layer thickness, wall thickness and proportionality constant of PAA membranes using the SEM micrographs and the software Image-J, for different anodization durations carried out in 0.3 M oxalic acid at a temperature of 8 °C.

Sample	Duration (h)	Barrier layer thickness (B) (nm) 8 °C	Wall thickness (W) (nm) 8 °C	Proportionality constant (λ_p) 8 °C
A1	2	62± 4	101 ±7	1.607
A2	4	70±5	103±4	1.680
A3	6	74±4	105±5	1.777
A4	8	67±7	104±7	1.805
A5	10	70±5	100±8	1.845

Table 3.3.6 Barrier layer thickness, wall thickness and proportionality constant of PAA membranes using the SEM micrographs and the software Image-J, for different anodization durations carried out in 0.3 M oxalic acid at a temperature of 18 °C.

Sample	Duration (h)	Barrier layer thickness (B) (nm) 18 °C	Wall thickness (W) (nm) 18 °C	Proportionality constant (λ_p) 18 °C
A1	2	61 ± 5	104±6	1.527
A2	4	67±4	108±5	1.606
A3	6	71±5	102±4	1.664
A4	8	70±5	101 ±5	1.718
A5	10	71±5	103±4	1.747

3.4 FAST FOURIER TRANSFORM (FFT) BASED ANALYSIS OF PORE REGULARITY

The regularity of the pore array in the PAA membrane is quantitatively investigated by using 2D FFT pattern of the SEM micrographs. This is very effective in establishing the effect of anodization conditions on the symmetry of pore distributions. FFT images for PAA membranes were generated from the image software using WSxM (<http://www.nanotec.es>), which give the periodicity of the pores in the inverse space showing the lattice points for the corresponding SEM images of PAA. It reveals the periodicity of the pore distribution, such as, (i) six distinct points or six-fold symmetry for the highly ordered pore distributions, (ii) the disc shape for disordered pore structure, and (iii) a ring for ordered periodicity with non-uniform pore size. The effect of anodization conditions based on their regularity profile is discussed below.

3.4.1 Effect of anodization duration

The fast Fourier transforms (b, e and h at 8 °C and b, e and h at 18 °C) and their radial averages (c, f and i at 8 °C and c, f and i at 18 °C) of PAA membranes at different anodization durations were shown in the Figure 3.13 and Figure 3.14. A quantitative calculation, based on radial averages, shows a small increase of the averaged regularity ratio with an increase of anodization duration from 2h to 6h at 8 °C and decrease from 8h to 10 h. At 18 °C, a decrease of average regularity ratio with an increase of anodization duration from 2h to 10h is observed. The effect of anodization duration on the alumina pore ordering at 8 °C and 18 °C is shown in the Figure 3.15. In this case, the

regularity ratios (R , eq.no 1.5.1) were calculated from the FFT intensity profiles (Figure 3.13 c, f, i and Figure 3.14 c, f, i). The regularity ratio changes with time in a quite asymmetrical manner. Certainly, anodization duration for both the first step and the second step is the same, so the longer the anodization time means the longer first step of anodization. It has been formerly shown that if the first step of anodization duration

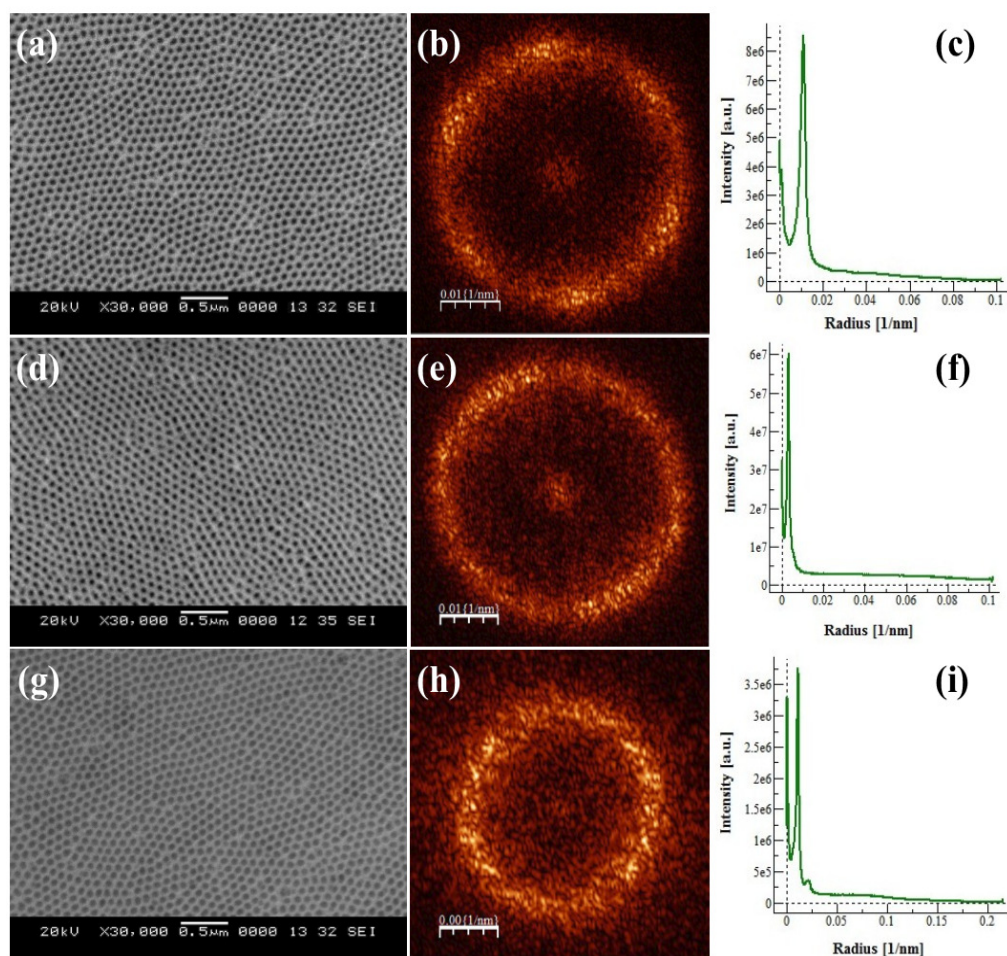


Figure 3.13 SEM top view micrographs, 2D FFT images and average profiles of the FFT radius of PAA formed 0.3 M of $H_2C_2O_4$ for 2h (a, b and c), 6h (d, e and f), and 10 h (g, h and i) at 8 °C.

is longer, the final nanoporous array would be better (Stepniowski et al., 2011). Overall, the increase of average regularity ratio with anodization duration was observed and at low temperature, regularity ratio values were found to be larger compared with those at higher temperatures. It may be noted that, the highest regularity ratio was observed for PAA membranes, obtained for 6h anodization at 8°C and 2h anodization at 18°C.

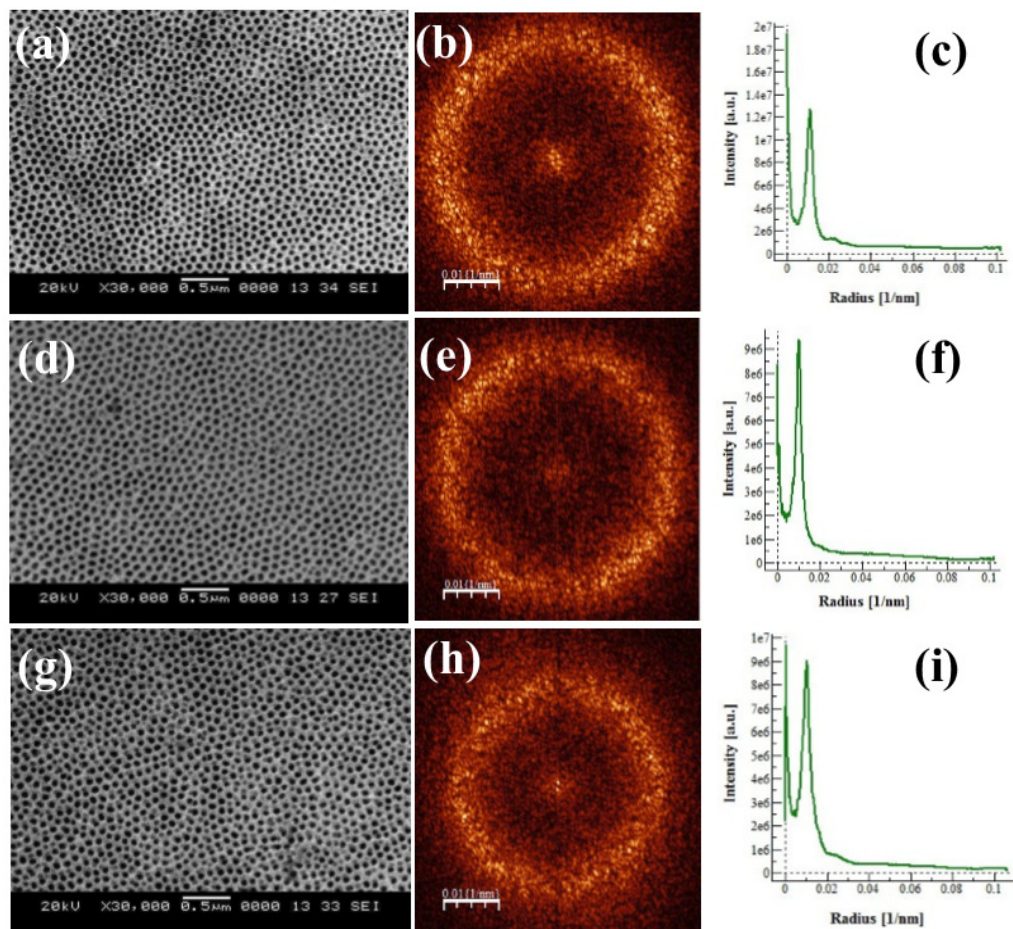


Figure 3.14 SEM top view micrographs, 2D FFT images and average profiles of the FFT radius of PAA formed 0.3 M of $H_2C_2O_4$ for 2h (a, b and c), 6h (d, e and f), and 10 h (g, h and i) at 18 °C.

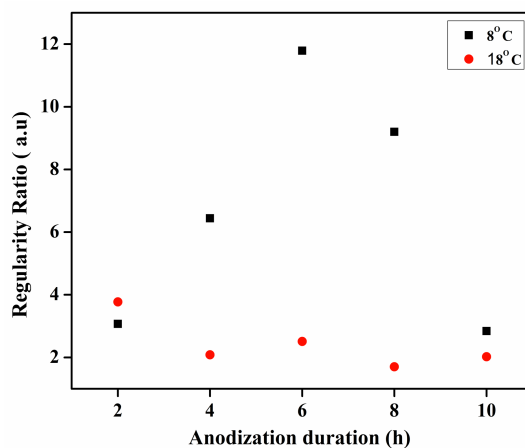


Figure 3.15 Average regularity ratio vs anodization duration (2, 4, 6, 8 and 10h) at 18 °C and at 18 °C.

3.4.2 Effect of electrolyte concentration

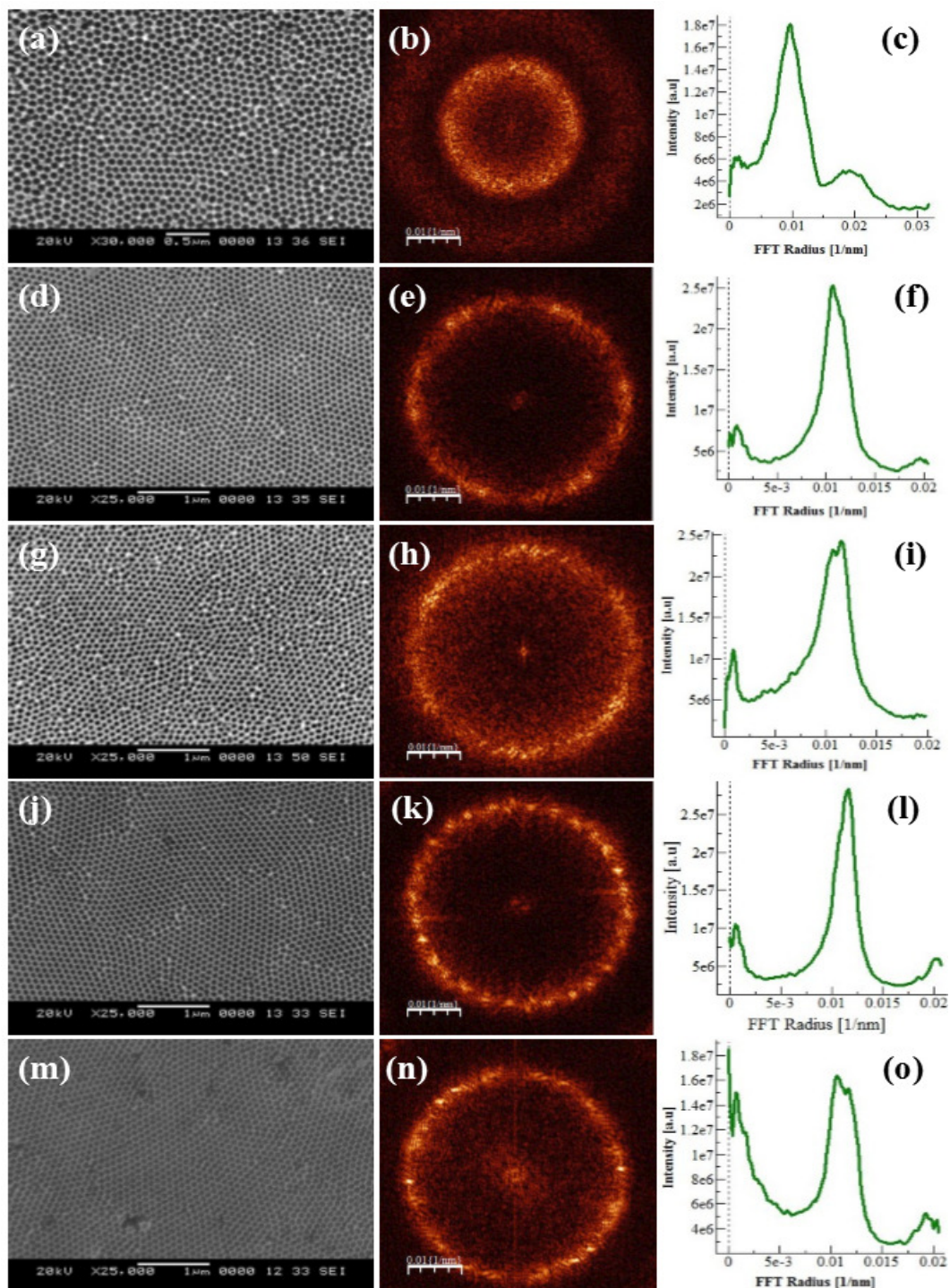


Figure 3.16 SEM top view micrographs, 2D FFT images and average profiles of the FFT radius of PAA formed with 0.1 M (a, b and c), 0.3 M (d, e and f), 0.5 M (g, h and i), 0.7 M (j, k and l) and 0.9 M (m, n and o) of $\text{H}_2\text{C}_2\text{O}_4$ under a constant anodization potential of 40 V

The electrolyte concentration was also influenced by the regularity of the pores in the anodization process. Figure 3.16 indicates the 2D FFT images (0.1-b, 0.3-e, 0.5-h, 0.7-k and 0.9 M-n) and average FFT radius profiles (0.1-c, 0.3-f, 0.5-i, 0.7-l and 0.9 M-o) of SEM images of PAA membranes obtained at different electrolyte concentrations. In the case of 0.3 M oxalic acid, the periodicity of the pores is high and due to this six distinct spots on the FFT spectrum was observed (Sulka et al., 2010) (Sulka and Stepniowski, 2009). The periodicity of the pores decreases with increasing electrolyte concentration from 0.5 to 0.9 M. Because of this disordered ring shape of FFT spectrum was observed. But in the case of 0.1 M, thick ring shape FFT image reveals the low periodicity of the pores. Moreover the quantitative investigation was carried out in order to obtain deeper understanding of the regularity of pore arrangement.

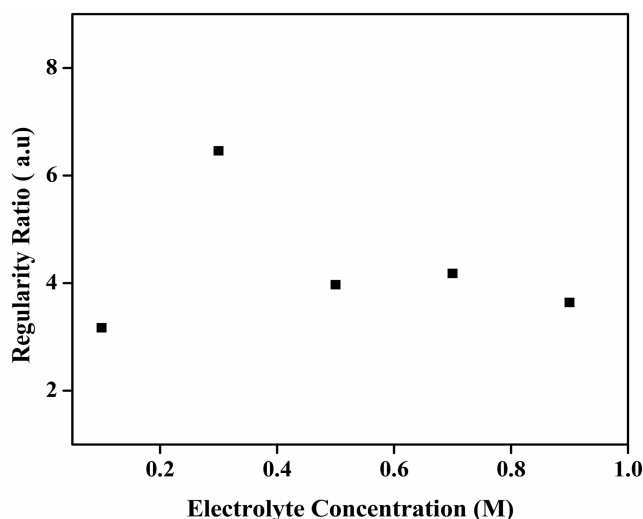


Figure 3.17 The regularity ratio as a function of electrolyte concentration (0.1-0.9 M) for PAA formed under a constant potential of 40 V

A moderately higher intensity of radial profile was observed in the case of 0.3 M electrolyte concentration. Regularity ratio (R , eq.no 1.5.1) as a function of electrolyte concentration is shown in the Figure 3.17. From the above results, it was concluded that the better arrangement of pores in the PAA membranes was possible in 0.3 M (Figure 16e) oxalic acid. Below and above this optimal concentration, a significant decrease of the pore regularity was observed. Regularity ratios of PAA membranes obtained in different electrolyte concentrations were tabulated in Table 3.4.1.

Table 3.4.1 Regularity ratios of PAA membranes obtained at different electrolyte concentrations (0.1-0.9 M)

PAA (M)	Regularity ratio (a.u)
0.1	3.17
0.3	6.46
0.5	3.97
0.7	4.18
0.9	3.64

3.4.3 Conclusions

1. The effect of process parameters such as anodization duration and electrolyte concentration on pore parameters of PAA membranes were studied systematically.
2. Increasing of anodization duration causes the changes in pore dimensions. This was due to the increase in the uniformity of pore structure array with the increase of the anodization duration.
3. Increasing electrolyte concentration also shows the changes in pore dimensions from 0.1 to 0.3 M. This can be attributed to growth rate and volume expansion of aluminium oxide which increases with increasing electrolyte concentration.
4. The nanopore arrangement was calculated based on the FFT images using WSxM software. From the FFT analysis, it was revealed that the better nanopore arrangement was possible for an optimal anodization duration of 6h and electrolyte concentration of 0.3 M.

Chapter 4

MECHANICAL PROPERTIES OF POROUS ANODIC ALUMINA MEMBRANES

This chapter discusses the mechanical properties of PAA membranes, such as hardness and Youngs moduli using micro and nanoindentation techniques. The effect of porosity and regularity ratio of pores on mechanical properties of PAA membranes were studied in detail.

4.1 INTRODUCTION

Presently, great attention is paid to the manufacturing of well-organized membranes based on porous materials, such as the PAA membranes. These are being used to produce nano structured surfaces on a large scale. The chemical structure of PAA membranes are usually composed of four layers (Romero et al., 2014). In general, the presence of these two layers and the existence of various crystallographic phases after annealing the samples above 800 °C (Dehnavi et al., 2014) influence the mechanical stability of PAA. Hardness and Youngs moduli can be varied to a large extent by varying the anodizing (Aerts et al., 2007) conditions. The surface properties of the PAA membranes make anodized aluminium products suitable for a broad array of applications, including their use in the aerospace industries, architectural applications and packaging. In several of these applications an important role is played by the mechanical properties like wear resistance and hardness (Ngan, 2005). In fact, the mechanical response of macroscopic honey comb structures has raised a lot of research interest in

the mechanics community (Lu et al., 2002). By varying the indentation depth, change in elastic modulus and hardness of PAA membranes formed in oxalic acid were already reported (Xia et al., 2004). However the mechanical properties of PAA membranes synthesized using sulphuric acid as electrolyte have been much less investigated.

In the present work, the anodizing of polished samples was carried out in two different electrolytes, such as 0.3 M oxalic acid at 40 V and 0.3 M of sulphuric acid at 20 V for 6h, and then the formed oxide layer was eliminated by etching the samples in a mixture of 1.8 wt% H_2CrO_4 and 6 wt% H_3PO_4 acid at 60 °C. The foils were then anodized with similar conditions as those of the first step for 6h. After the second step anodization, pore widening was performed using 5 wt% of H_3PO_4 for 30 min at room temperature.

4.2 RESULTS AND DISCUSSION

4.2.1 Micro indentation

Figure 4.1 shows the FE-SEM (a and f), cross-sectional views (b and g), fast Fourier transforms (c and h), radial averages (d and i) and surface roughness (e and j) images of anodic alumina membranes obtained using oxalic and sulphuric acid as electrolytes at a temperature of 8 °C. From Figure 4.1, it was noticed that highly ordered hexagonal pores were produced in both oxalic and sulphuric acids. Closer analysis of the pores tells us that they are round in shape with a porosity of 26.40% and 10.37% with a pore diameter of about 60 nm and 23 nm for oxalic and sulphuric acids, respectively. Results indicate that pores are arranged in uniform order and organized into a honey comb like-array structure in both oxalic and sulphuric acid cases (Figure 4.1a-c and 4.1f-h). The intensity of the radial averages calculated for whole FFT is higher in oxalic acid (Figure 4.1d) as compared with that for sulphuric acid (Figure 4.1i). This may be due to better array of pore arrangement in oxalic acid (Stepniowski et al., 2014b). The average surface roughness of PAA membranes estimated using WSxM software, for oxalic acid was ~ 38 nm (Figure 4.1e) and for sulphuric acid ~ 14 nm (Figure 4.1j) respectively.

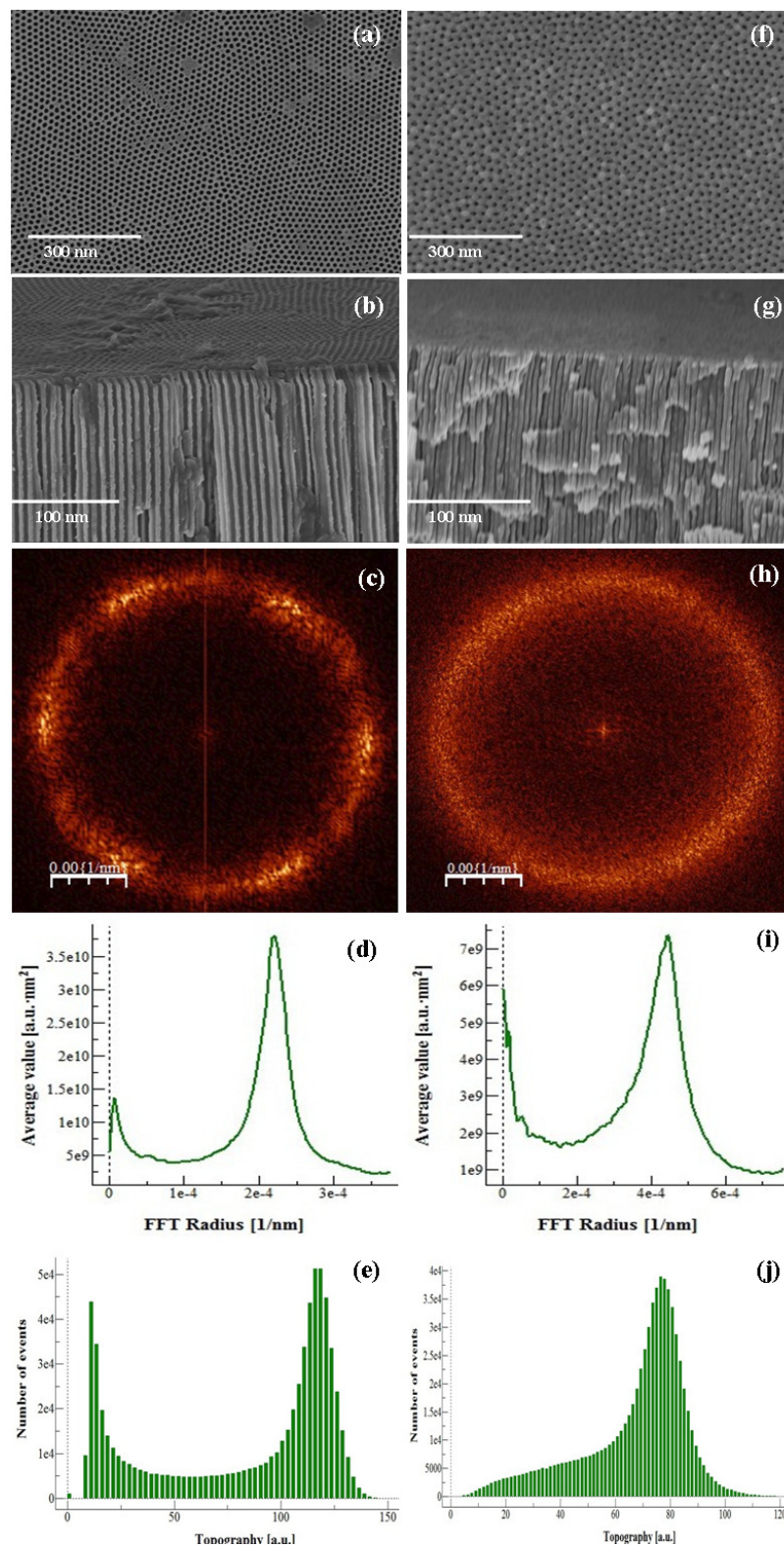


Figure 4.1 FE-SEM images (a, f), cross-sectional images (b, g), fast Fourier transforms (c, h), radial averages (d, i) and average surface roughness (e, j) of PAA membranes obtained in 0.3 M oxalic and 0.3 M of sulphuric acid at 8 °C.

The alumina layer thickness of PAA membranes used in our study was measured about 47 μm and 41 μm for oxalic and sulphuric acids, respectively. These values are about more than 4 times the nano-indentation depth. Vickers hardness was estimated using the eq.no 2.5.1 (Tsyntsar et al., 2014) discussed in the second chapter. In this study, the forces were set as 0.98 N and 9.8 N. The evaluated hardness values at 0.98 N were 0.22 GPa and 0.47 GPa for oxalic and sulphuric acids respectively. Micro hardness of PAA membranes changes with porosity and an increase of porosity in oxalic acid causes decrease in hardness (Tsyntsar et al., 2014).

Figure 4.2a and Figure 4.2e shows the SEM image of an indenter of the PAA using a Vickers indenter with a load of 0.98 N for oxalic and sulphuric acids. These images reveal that the pores (Figure 4.2b and Figure 4.2f) were crushed during the indentation. Figure 4.2c (oxalic acid) and Figure 4.2g (sulphuric acid) show the SEM image of PAA using a Vickers indenter with a load of 9.8 N. When load is about 9.8N, the alumina structure undergoes a fracture along the pore wall. It may be noted that the crack is near to the indent and an arrow mark illustrates that surface ring cracks are generated within the Vickers indentation in oxalic acid case. Figure 4.2d is the higher magnified image of crack formed in oxalic acid (Figure 4.2c), in which the gap between the two arrow marks illustrates that the crack flow through the nano porous anodic alumina. Small arrow and bigger arrow marks in Figure 4.2g indicate that the cracks are generated from the corners of the Vickers indentation pattern and the higher magnified image of crack produced in sulphuric acid is shown in Figure 4.2h. Compared with PAA membranes of sulphuric acid, more cracks were generated in those of oxalic acid, with the application of 9.8 N load due to the increase in pore diameter and increase in porosity was observed by SEM analysis.

4.2.2 Nanoindentation

Figure 4.3 shows the corresponding AFM topographic images of nanoindentation imprints in samples prepared in oxalic (Figure 4.3a) and sulphuric acids (Figure 4.3d) after indentation. Surface height profiles of residual Berkovich indents (Tan and Cheetham,

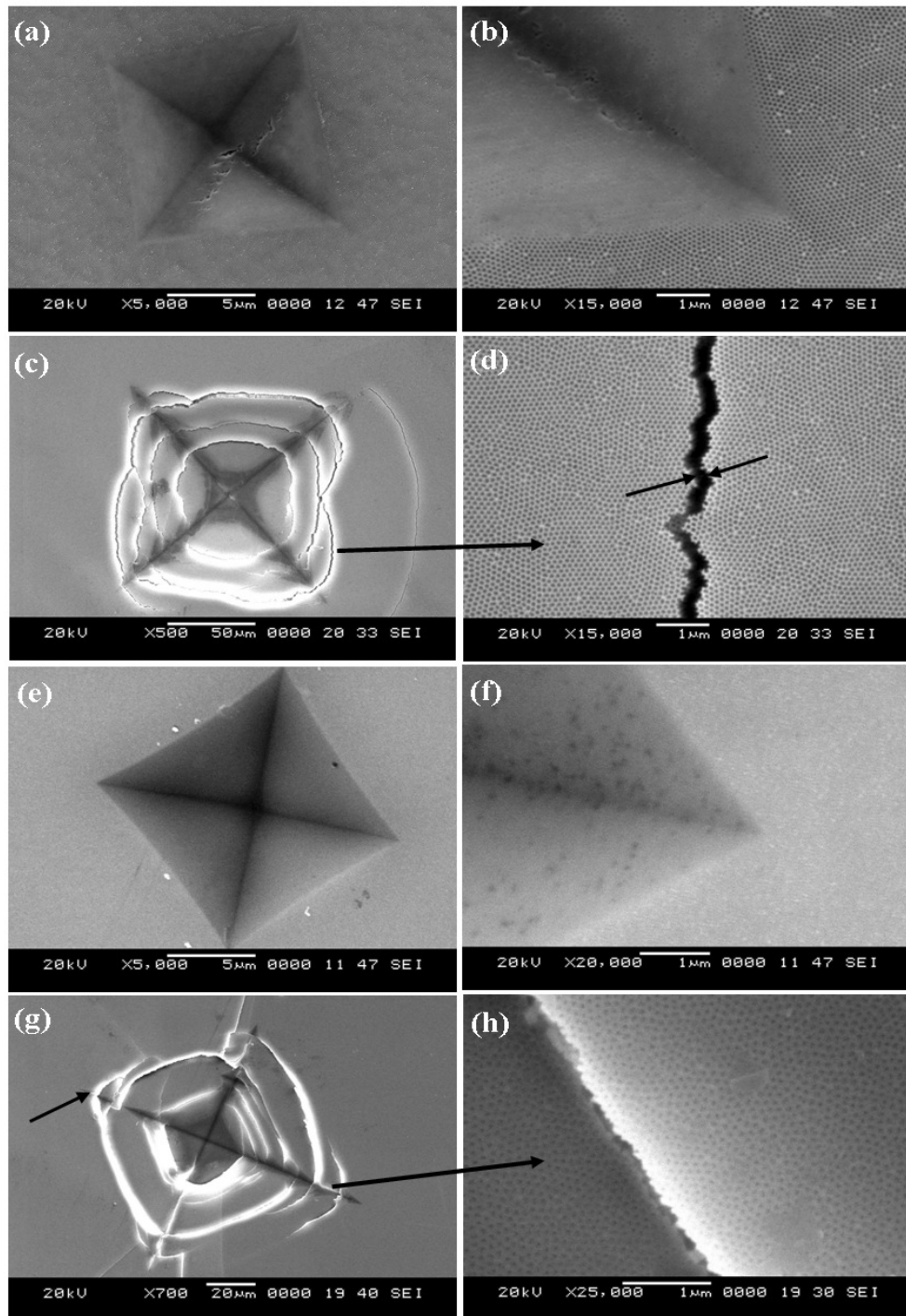


Figure 4.2 SEM micrographs of the indent mark of the PAA using Vickers Indenter and corresponding morphologies after applying loads at the edge of the indented PAA formed using sulphuric acid:0.98 N (a, b) and 9.8N(c, d) and oxalic acid:0.98 N (e, f) and 9.8 N (g, h) at 8 °C

2011) for oxalic acid (Figure 4.3b) and sulphuric acid (Figure 4.3e) cases made on the three directions of PAA membranes can be seen. The strain hardening behavior of PAA membranes were represented by red, green and blue arrows respectively along the diagonals of the indenter. Green color direction exhibits higher value of the pile-up developed around the indentation in both oxalic acid (Figure 4.3c) and sulphuric acid (Figure 4.3f) cases. PAA membranes formed in oxalic acid case exhibits the least amount of pile-up compared with sulphuric acid case around the indentation. This is because in sulphuric acid case lower elastic deflection and surface roughness tend to exhibit more pile-ups, ranging from 50-150 nm.

SEM images of the nanoindentation imprints for PAA membranes from oxalic acid (Figure 4.3g) and sulphuric acid (Figure 4.3i) are shown in the Figure 4.3. Figure 4.3h and Figure 4.3j show the indented images attained by applying a load of 10 mN for oxalic and sulphuric acid cases. From Figure 4.3, it can be noted that, no cracks were seen near or surrounding of the imprint in oxalic and sulphuric acid cases. This may be due to the intrinsic structure of PAA and also due to the difference in other parameters affecting the growth rate of PAA (Ng et al., 2009). The high-magnification images (Figure 4.3j) show that minor cracks are actually formed in sulphuric acid. It was attributed to the strain induced owing to the difference in pore sizes (Li and Huang, 2007b). PAA membranes formed in oxalic acid do not show any sign of cracking. It was observed that, no cracks on PAA were produced in oxalic acid, when comparing with those produced in sulphuric acid, even though they had a larger pore size. This may be due to the differences between the structural composition of PAA produced in sulphuric and oxalic acids. Figure 4.4 shows the corresponding load penetration depth curves for PAA membranes formed in oxalic and sulphuric acids respectively. Load verses indenter displacement shows a smooth behavior during indentation test. The indentation penetration displacement was increased with increasing load (Figure 4.4a) and the indenter displacement was not the same for oxalic and sulphuric acid PAA membranes during loading time. It was noticed that the indenter did not penetrate in sulphuric acid case, as much as it did in oxalic acid for maximum load. As a result, PAA membranes formed in

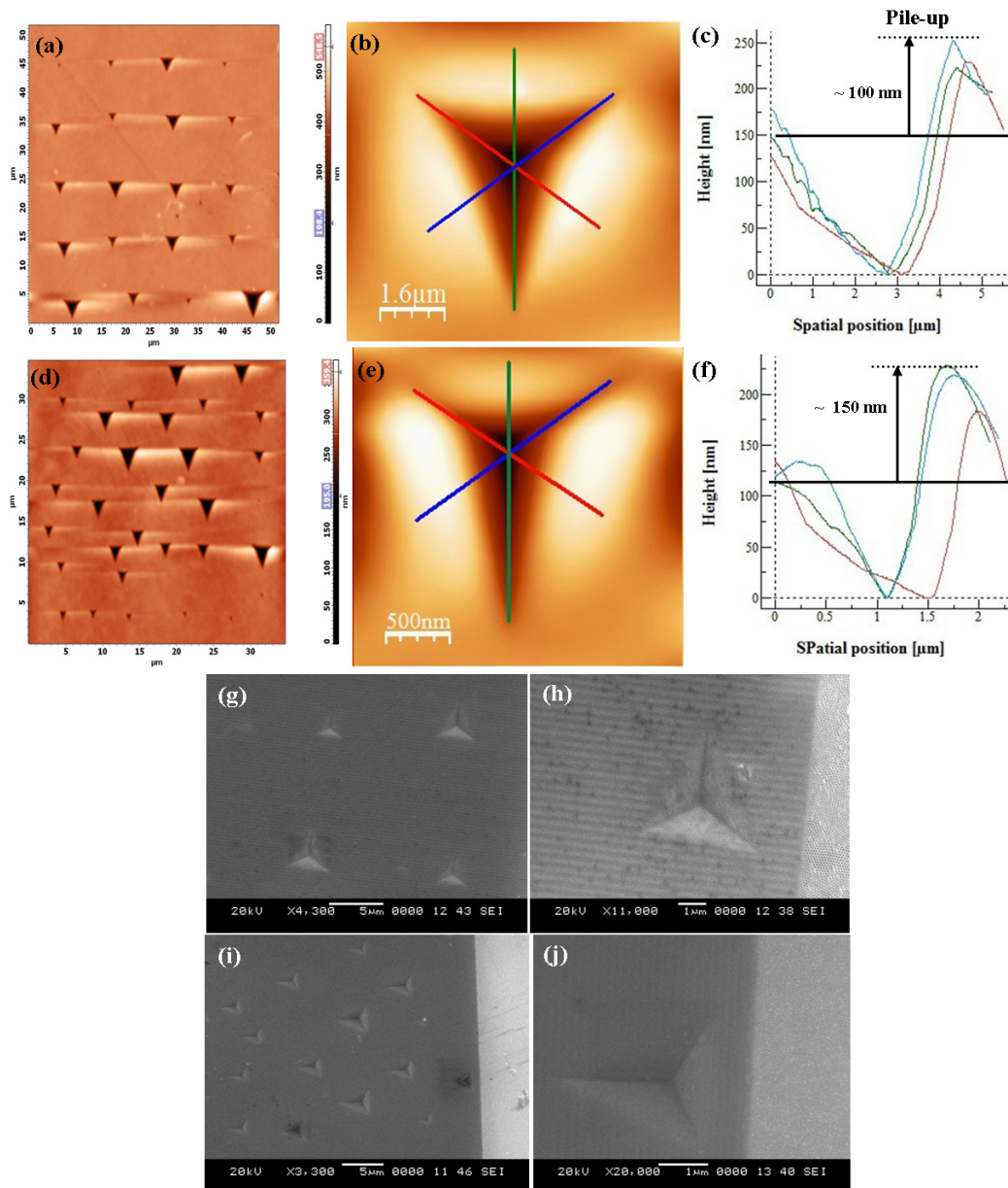


Figure 4.3 AFM topographic images of nano indentation imprints in oxalic acid (a) and sulphuric acid (d) after indentation. Surface height profiles of residual Berkovich indents made on the three directions of PAA membranes (Oxalic acid: b, c and Sulphuric acid: e, f). SEM images typical Berkovich of the nano indentation imprints and indented images obtained by applying a load of 10mN for oxalic acid (g, h) and sulphuric acid (i, j).

oxalic acid appears to be better capable to survive a state of deformation (Samantilleke et al., 2013). This nature is attributed to the change of pore sizes in PAA membranes that are attained by varying the anodization process parameters. At the beginning of the loading process in oxalic and sulphuric acid nanopore walls crush with one another (Fang et al., 2007), causing a little pop-in behavior (Figure 4.4b).

The elastic deflection (h_{el} , eq.no 2.5.2) of the anodic alumina at the maximum load with negligible of pile-up is measured using Oliver and Pharr formula (Oliver and Pharr, 2004). The plot of contact depth verses elastic deflection of the material surface is given in Figure 4.4. Results indicate that surface elastic deflection of the PAA membranes increases slowly with indenter displacement in both oxalic and sulphuric acid cases. In oxalic acid case (Figure 4.4c) elastic deflection increases linearly with applied load, but in sulphuric acid (Figure 4.4d) not in a linear manner, due to low porosity of PAA membranes obtained in sulphuric acid. On the other hand, the magnitude of the contact depth (h_c) also increased with indenter displacement (h_i) in oxalic and sulphuric acids for the same applied load. It can be noted that, for small loads below 3 mN, the contact depth increases quickly as a result of the crash of the nanopore walls (Samantilleke et al., 2013).

In order to examine the mechanical properties further, we studied the hardness (H_V , eq.no 2.5.3) and Youngs moduli (E , eq.no 2.5.4) of PAA membranes obtained in oxalic and sulphuric acids. The hardness and the E moduli of the PAA membranes for indentation depths of about 50-350 nm were 3 GPa to 6 GPa and 80 GPa to 110 GPa for oxalic acid; 5GPa to 10 GPa and 120 GPa to 160 GPa for sulphuric acid respectively. Nano mechanical features of PAA membranes obtained in oxalic and sulphuric acids are tabulated in Table 4.2.1, Table 4.2.2, Table 4.2.3 and Table 4.2.4. A plot of the hardness and E moduli as a function of applying load for oxalic and sulphuric acids is shown in the Figure 4.4. The hardness and E moduli decreases with increasing applied load up to 4 mN and then remains almost constant from 4 mN - 10 mN. PAA membranes show quite a similar trend for hardness (Figure 4.4e) and E Moduli (Figure 4.4f) as a function of the applied load, in oxalic and sulphuric acid case apart from small loads, where there is

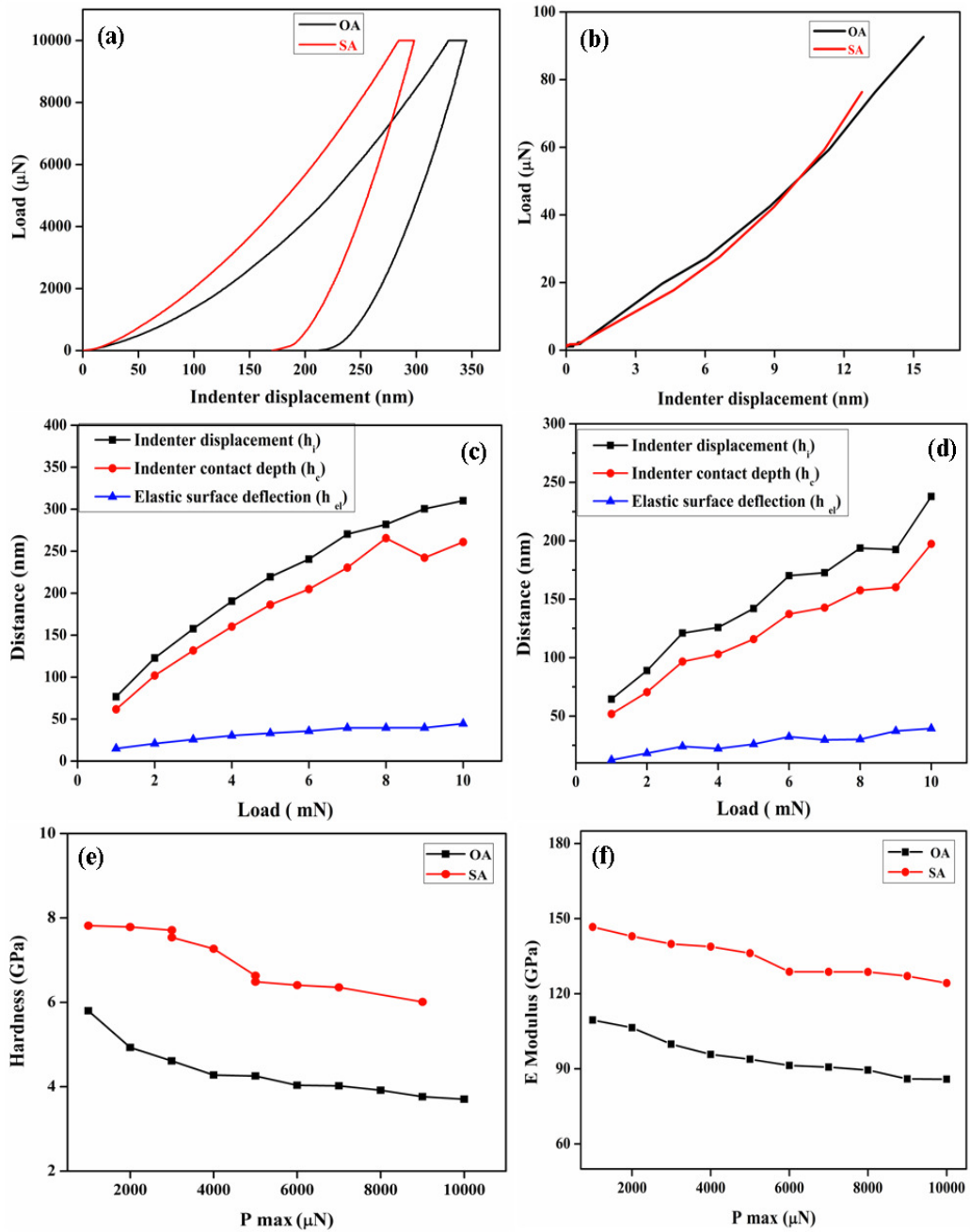


Figure 4.4 Load-displacement curves of the PAA membranes formed in Oxalic and Sulphuric acid (a, b). The surface elastic deflection, contact depth and indenter displacement as a function of the applied load for PAA membranes in oxalic (c) and sulphuric acid (d). Hardness (e) and E Modulus (f) as a function of load (P_{max}) for PAA membranes prepared in oxalic and sulphuric acids.

a huge dispersion. This is because of small difference in the porosity percentage of the PAA membranes formed in oxalic and sulphuric acids (Ng et al., 2009). The hardness

Table 4.2.1 Nano mechanical analysis of PAA membranes formed in oxalic acid

Load $P_{max}(m/N)$	Contact depth h_c (nm)	Stiffness constant $S(\mu m/nm)$	Maximum displacement h_{max} (nm)
1	61.6	49.8	76.9
2	101.9	71.8	123.4
3	131.7	87.1	158.0
4	160.1	99.0	190.5
5	186.2	112.6	219.6
6	204.8	125.7	240.6
7	230.5	132.1	270.4
8	265.5	151.2	282.1
9	242.2	151.4	300.5
10	260.9	189.5	311.2

and the E moduli of the PAA membranes formed in oxalic acid is less compared with those formed in sulphuric acid, because of lower porosity and regularity ratio of PAA in sulphuric acid (Ng and Ngan, 2012). Residual mechanical stresses and differences in the structure of PAA are reasons for the low values of hardness and youngs moduli in oxalic acid case.

Table 4.2.2 Hardness and Young's moduli of PAA membranes formed in oxalic acid

Load $P_{max}(m/N)$	Hardness (GPa)	Young's Modulus (GPa)
1	5.79	101.59
2	4.92	106.41
3	4.61	99.87
4	4.27	95.77
5	4.25	93.86
6	4.03	91.37
7	4.02	90.70
8	3.91	89.52
9	3.76	85.97
10	3.70	85.85

Table 4.2.3 Nano mechanical analysis of PAA membranes formed in sulphuric acid.

Load $P_{max}(m/N)$	Contact depth h_c (nm)	Stiffness constant $S(\mu m/nm)$	Maximum displacement h_{max} (nm)
1	51.8	60.2	64.4
2	70.4	82.2	88.8
3	96.6	93.3	120.9
4	102.8	101.4	125.7
5	115.7	115.3	142.0
6	137.3	115.9	170.1
7	142.7	126.2	172.6
8	157.6	149.2	193.7
9	160.2	140.7	192.4
10	197.3	171.0	237.9

Table 4.2.4 Hardness and Young's modulus of PAA membranes formed in sulphuric acid.

Load $P_{max}(m/N)$	Hardness (GPa)	Young's Modulus (GPa)
1	7.81	146.68
2	7.78	142.93
3	7.70	139.88
4	7.53	138.80
5	7.26	136.18
6	6.63	128.81
7	6.48	128.77
8	6.40	128.77
9	6.35	127.06
10	6.01	124.28

4.2.3 Conclusions

1. Highly ordered hexagonal array of PAA membranes were prepared using oxalic and sulphuric acids as electrolytes at 8 °C. Regularity ratio of PAA membranes was more in oxalic acid than in sulphuric acid, because of uniformity of pore arrangement obtained in oxalic acid.
2. Micro hardness of PAA membranes produced in sulphuric acid is high, due to the difference between structural composition of PAA formed in oxalic and sulphuric acids. The pile-up developed around the indent in PAA membranes formed in sulphuric acid is more pronounced. This was caused by lower surface roughness and elastic deflection of PAA formed in sulphuric acid. Nanoindentation does

not reveal any major crack formation in PAA membranes prepared in oxalic and sulphuric acids.

3. The hardness-contact depth analysis indicates that for oxalic and sulphuric acids, hardness decreases with increasing applied load. However, the corresponding hardness remains nearly constant at high loads (4 mN). Young's modulus and nano hardness of PAA in sulphuric acid is higher compared with those of oxalic acid cases. This was attributed to the low porosity and regularity of pores obtained in sulphuric acid.

Chapter 5

OPTICAL PROPERTIES OF POROUS ANODIC ALUMINA MEMBRANES

This chapter illustrates the optical analysis of PAA membranes using UV-Visible and Photoluminescence techniques. The effect of growth parameters such as anodization duration and electrolyte concentration on optical properties of PAA membranes were studied in detail.

5.1 INTRODUCTION

In recent years, a great scientific attention has been focused on the porous materials with ordered nanopore arrays, due to their potential applications as membranes in synthesis of nanostructured materials (Jessensky et al., 1998). Among the different nanomaterials used to develop optical sensing platforms, PAA has gained increasing interest during the last few years as a result of its interesting physical and chemical properties. (Santos et al., 2014). PAA has been preferred as a suitable material for manufacturing optical nanoscale devices (Liu et al., 2008) (Ye et al., 2011) due to their unique optical properties. Furthermore, studies on photoluminescence (PL) properties of PAA have attracted considerable attention recently, because these membranes could be used as photonic crystals (Li et al., 1999), humidity sensors (Nahar and Khanna, 1998), cathodes for organic light emitting diodes (Kukhta et al., 2002) etc. Over the past decades, many efforts have been made to explain the PL mechanism and the nature of PL centers in PAA membranes (Li and Huang, 2007a). In these works, one suggests that F^+ centers, are

associated with the oxygen vacancies (Du et al., 1999). Further, F centers which are also attributed to oxalic impurities get incorporated into PAA structure during the anodization process (Li et al., 2003). The maximum peak intensity and position of PL curve depends on anodizing parameters and generally the PL curve of PAA is a Gaussian-like shape (bell structure).

In the present study, Anodization was carried out with a constant potential of 40 V by varying the electrolyte concentration from 0.1 to 0.9 M with a step of 0.1 M at 18 °C. First step anodization was carried out for 12h. The aluminium oxide obtained during the first step anodization was removed by chemical etching in the bath containing 6 wt% H_3PO_4 and 1.8 wt% H_2CrO_4 at 60 °C for 2h. Next, samples were re-anodized at the same anodic conditions for 2h. Finally, to remove the remaining part of the aluminium substrate, the sample was etched in a saturated $CuCl_2$ solution.

5.2 RESULTS AND DISCUSSION

Figure 5.1a shows the optical absorption spectra of the oxalic and sulphuric alumina and results indicated that optical absorption was high in oxalic alumina compared with sulphuric alumina. The bandgap energy of PAA membranes estimated from UV-Visible absorption spectra using the Tauc's relation (Laatar et al., 2016),

$$(\alpha h\nu)^{1/n} = A(h\nu - E_g) \quad (5.2.1)$$

Where E_g is optical bandgap, $h\nu$ is incident photon energy, A is a constant parameter independent of photon energy, α is absorption coefficient and n is a constant which depends on the type of the transition between valance band and conduction band, for amorphous materials the value of n is 2 (Kim et al., 2000). The plot of $(\alpha h\nu)^2$ as a function $h\nu$ (eV) is shown in the Figure 5.1b. The calculated bandgap energy values for PAA membranes were found to be 3.7 and 4.3 eV for oxalic and sulphuric alumina respectively. Decrease in band gap energy in oxalic alumina compared with sulphuric alumina may be due to more absorption defects and oxalic impurities in oxalic alumina (Majid et al., 2013), (Vrublevsky et al., 2014). Moreover, the incorporation of cations and anions into oxides during anodic oxidation of metals also causes the change in the

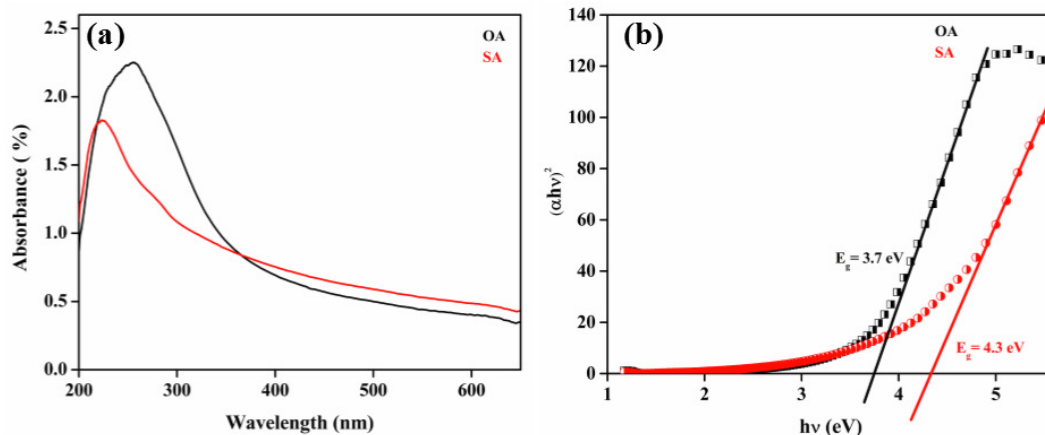


Figure 5.1 UV-Visible absorption spectra (a) and plot of $(\alpha h\nu)^2$ versus $h\nu$ (eV) of PAA membranes for oxalic and sulphuric alumina.

band gap of oxalic alumina (Stepniowski et al., 2016). The reflectance spectra of the PAA membranes were shown in the Figure 5.2. The reflectance increases gradually and smoothly from blue region to red region of the spectrum, the interference band with

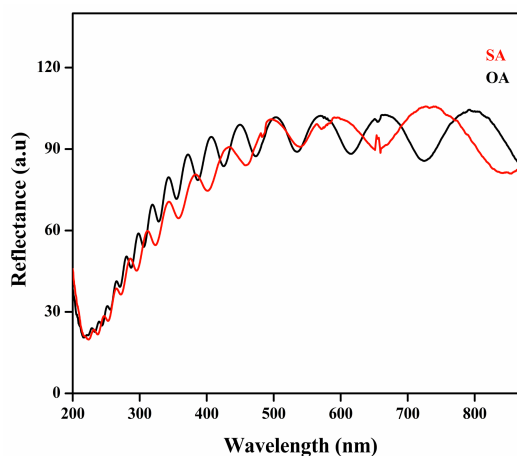


Figure 5.2 Reflectance spectra of PAA membranes obtained in oxalic and sulphuric acid solution.

maximum reflectance in the visible region shows a red shift in both oxalic and sulphuric alumina. The most significant factor for the red shift is the increase of thickness of PAA membranes according to the calculations obtained from Bragg's relation (Shaban, 2016), (Chen et al., 2007) which indicates that the wavelength of the maximum reflection increases with increasing film thickness. The reflectance spectra between 400-800 nm was also shown in the Figure 5.3 (Inset). Moreover, the coordinates of the PAA membranes were estimated using the international commission on illumina-

tion (CIE) 1931 and color functions are represented in Figure 5.3. The Chromaticity coordinates calculated for oxalic and sulphuric alumina were $x=0.3476$, $y=0.3371$ and $x=0.3476$, $y=0.3369$ respectively. The higher intensity reflectance peak was observed

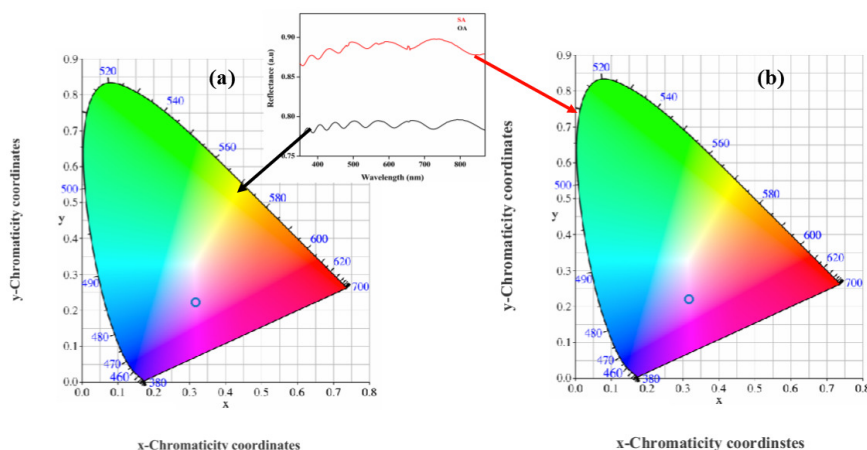


Figure 5.3 CIE chromaticity diagram for reflectance spectra in (a) oxalic and (b) sulphuric alumina.

in the red region in sulphuric and oxalic alumina. It was also confirmed by the CIE analysis of reflectance spectra for oxalic (Figure 5.3a) and sulphuric (Figure 5.3b) alumina. The maximum number of interference reflections were more in oxalic alumina compared with sulphuric alumina, due to lower thickness of alumina in sulphuric acid solution. The PL spectra of the PAA membranes obtained in oxalic and sulphuric acid electrolytes were shown in the Figure 5.4. It was inferred that PAA membranes exhibit a broad luminescence in the blue region (300-600 nm).

To study the dependence of blue PL band on the pore array of alumina, the asymmetric PL spectra can be assumed to be Gaussian (Huang et al., 2005), and it could be divided into two sub-bands without deviations, as shown in the Figure 5.4a, 4b. Two Gaussian components of emission peaks, one at lower energy side corresponding to optical transitions in the F centers (oxygen vacancy with two electron), whereas another one at higher energy side originating from F^+ centers (oxygen vacancy with one electron) were found in oxalic and sulphuric alumina. The maximum emission intensity for oxalic and sulphuric alumina were at 483 and 466 nm, which are near to middle of the blue region. On the other hand lower emission intensity for oxalic and sulphuric alu-

mina are at 423 and 421 nm, which are near to beginning of the blue region. Therefore, it is necessary to highlight that in spite of various electrolytes, spectra of these membranes do not coincide in position. From this it may be concluded that, the luminescence

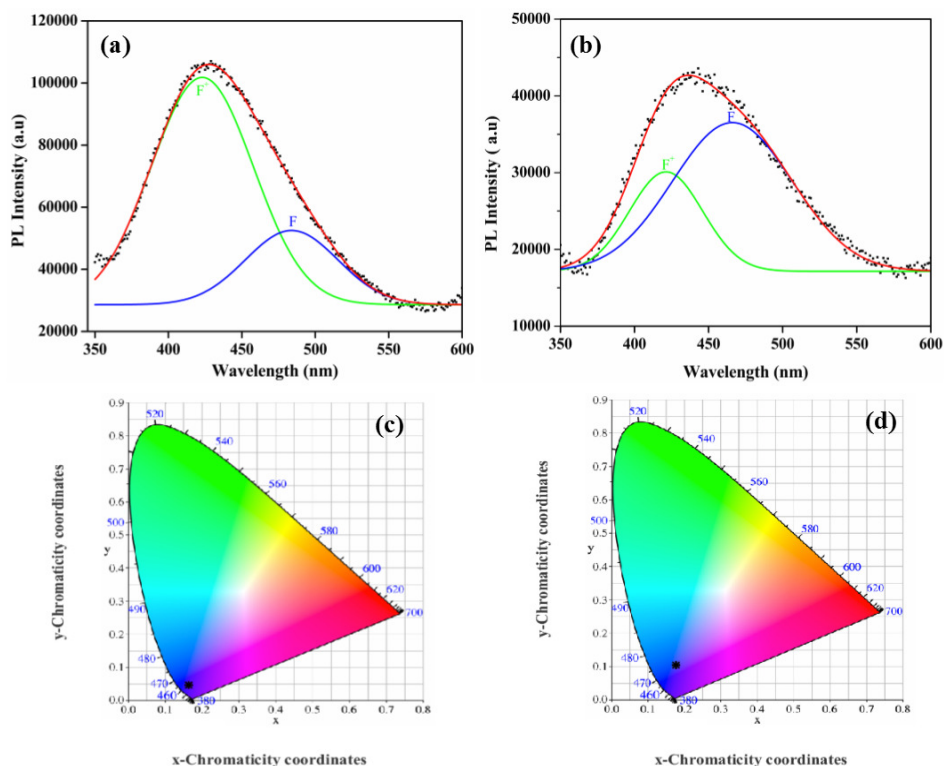


Figure 5.4 PL spectra with Gaussian, separated into two sub-bands in oxalic (a) and sulphuric (b) alumina. Chromaticity diagram for PL spectra in (c) oxalic and (d) sulphuric alumina.

of anodic alumina depends on the type of the acid in electrolyte solution. Chromaticity analysis of PL spectra for oxalic and sulphuric alumina was shown in the Figure 5.4. The chromaticity coordinates obtained for oxalic (Figure 5.4c) and sulphuric (Figure 5.4d) were $x=0.1951$, $y=0.2033$ and $x=0.2075$, $y=0.2483$ respectively. From Figure 5.4, it was observed that the maximum PL intensity of oxalic and sulphuric alumina have blue emission color. The intensity of PL peak is lower for sulphuric alumina than for membranes obtained in oxalic alumina. This could be due to presence of oxalic impurities in the structure of PAA in oxalic acid (Tao et al., 2003). The structural and optical analysis data was tabulated in Table 5.2.1 and Table 5.2.2.

Table 5.2.1 Structural analysis of PAA membranes formed in oxalic and sulphuric acids

Sample	Pore diameter (nm)	Interpore distance (nm)	Porosity %	Wall thickness (nm)
OA	64	122	25	29
SA	34	69	22	17

Table 5.2.2 PL data of PAA membranes formed in oxalic and sulphuric acids

Sample	λ (nm)	$F^+(\lambda_1)$ (nm)	$F(\lambda_2)$ (nm)
OA	428	423	483
SA	436	421	466

5.3 EFFECT OF ANODIZATION DURATION

To study the effect of anodization duration on the photoluminescence properties of the PAA membranes, PL spectra for PAA membranes obtained for 2h, 6h, and 10h durations at two different temperatures (8 °C and 18 °C) were shown in Figure 5.5. All the spectra of Figure 5.5 were attained at 325 nm excitation wavelength in order to investigate the optical transitions. It may be pointed out that from Figure 5.5, with an increase in the anodization duration the emission spectrum of the PAA membranes was broadened and shifted in the direction of shorter wavelength side (Nourmohammadi et al., 2012). Significant widening and shifting in the direction of UV region were noticed for PAA membranes with 10h anodizing time at 8 °C. Thus, it was inferred that an increase in anodizing time by 10h assisted in the creation of the optically active oxygen positions with sub band gaps which were out of the visible range. This event decreases the emission behaviour of the PAA membranes in the visible area. The locations of all Gaussian emissions of PAA membranes formed at 18 °C were shown by a blue shift. In Figure 5.5a, the greatest emission intensity (labeled as band 1) for 2h, 6h and 10h at 18 °C are at 483, 469 and 470 nm respectively, which are near to the middle of the blue region. However, the lower emission intensity (labeled as band 2) for 2h, 6h and 10h are 425, 421 and 426 nm which are near to the beginning of the blue region.

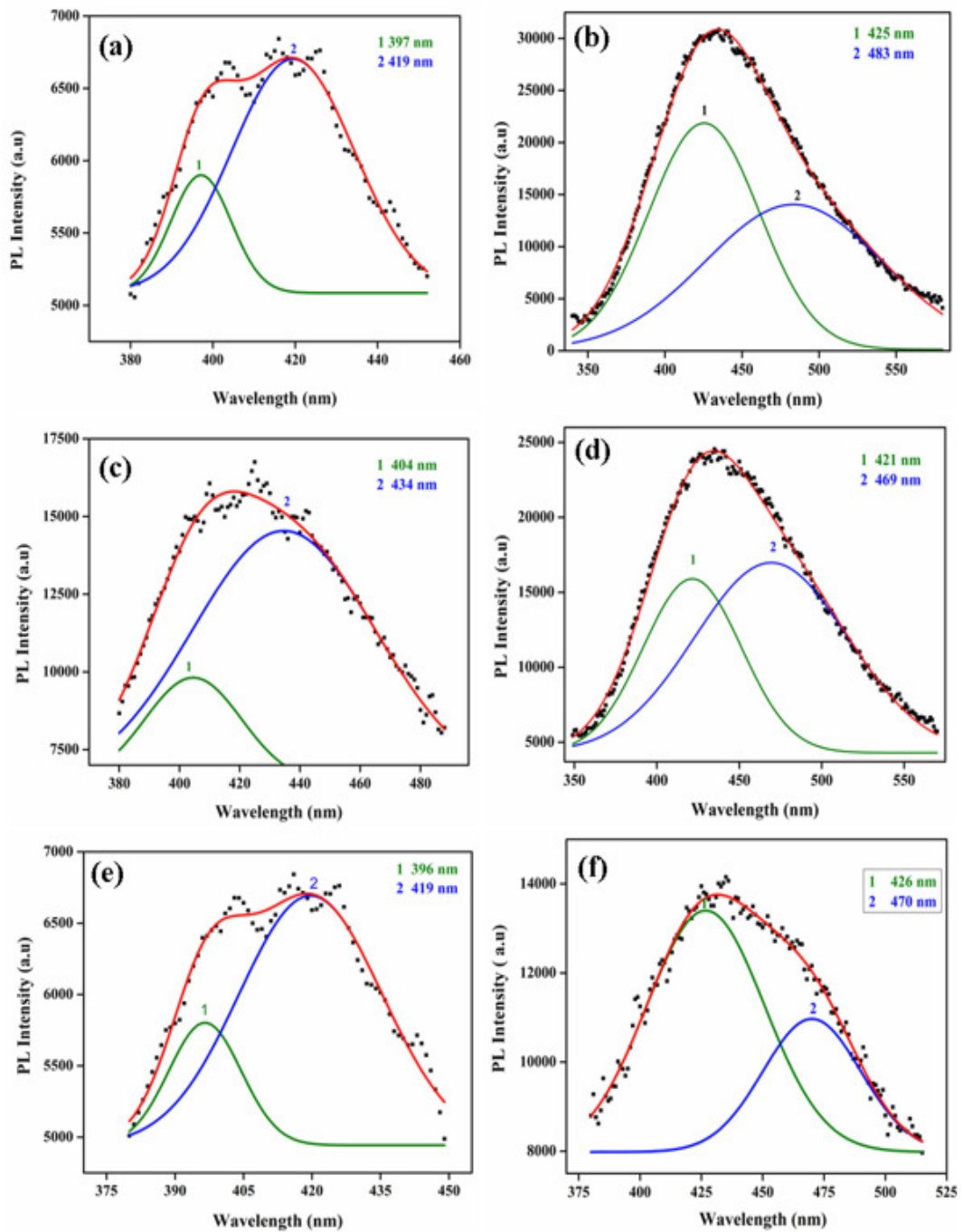


Figure 5.5 PL spectra of the PAA membranes obtained using anodization of Al foils in 0.3M oxalic acid at 8 °C and 18 °C under different anodization durations of 2h (a, b), 4h (c, d) and 10h (e, f) respectively. Each spectrum can be Gaussian separated into two sub bands, which are shown in thick lines and labeled as 1 and 2.

On the other hand, the greatest emission intensity (labeled as band 1) for 2h, 6h and 10h at 8 °C are 419, 434 and 419 nm respectively, which are near to the beginning of the blue region. However, the lower emission intensity (labeled as band 2) for 2h, 6h

and 10h are 397, 404 and 396 nm which are somewhat near to the UV region. All the measured values are tabulated in Table 5.2. For the membranes which are anodized for 10 h at 8 °C, a low emission peak is observed at 396 nm which is somewhat near to the UV region. This confirms the broadening of the electronic sub-band spacing because of the oxygen positions during a long time anodization (Nourmohammadi et al., 2012). After the formation of the pores in PAA, pore growth takes place in a steady state manner was reported (O’sullivan and Wood, 1970). In this arrangement, the porous Al_2O_3

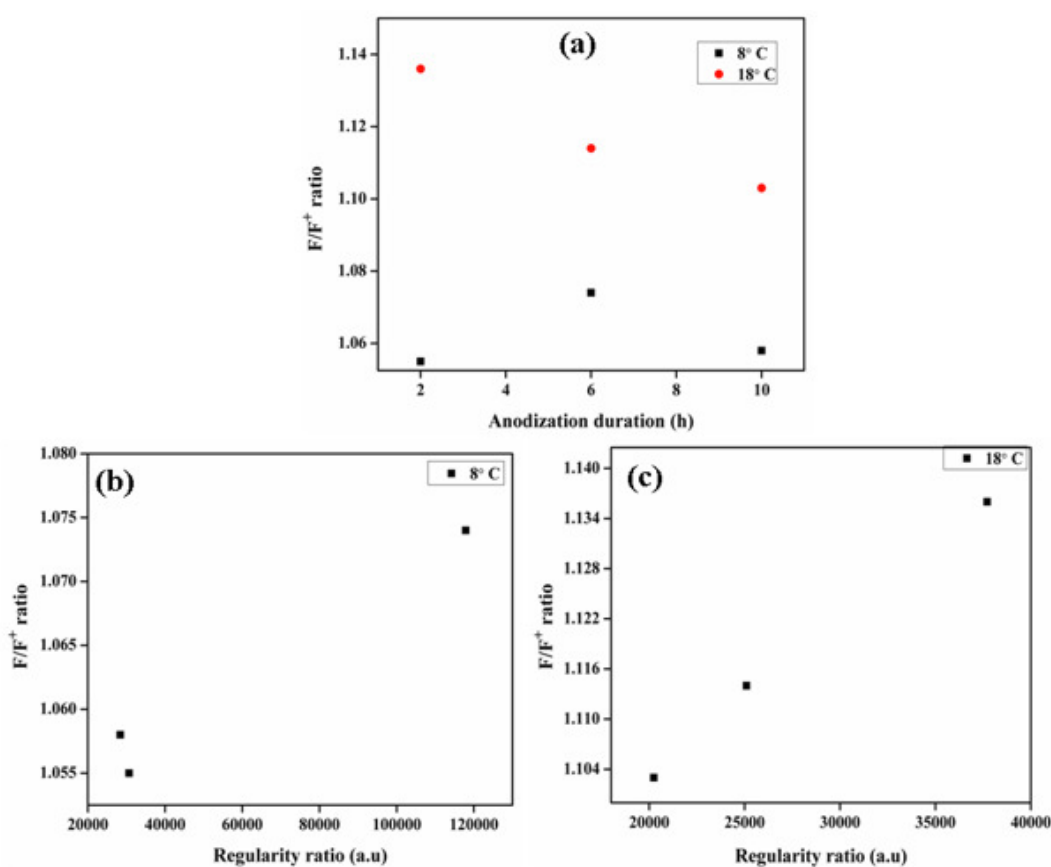


Figure 5.6 Effect of anodization duration on F/F^+ ratio at 8 °C and 18 °C (a), relationship of F/F^+ ratio and regularity ratio at 8 °C (b) and 18 °C (c)

layer thickness increases with time, and no major growth take place in its arrangement. It might be inferred that an increase in anodization duration would alone increase the PL line intensities. Further, a significant blue shift is noticed in all the PL emissions with an increase in the anodization duration (Figure 5.5). This shift is due to the longer duration (10 h) of voltage application influencing the sub-band electronic spacing in the anodic oxide layer. Additionally, the PL spectrum is gradually widened with increasing

anodization duration from 2h to 10h (see peaks 1 to 2 Figure 5.5 b, d, f). It can be assumed that these emissions were initiated from F^+ centers, which occur in the main part of the amorphous PAA membranes formed in the oxalic acid. Figure 5.6a shows the plot between anodization duration and the PL intensity ratio of F and F^+ centers (F/F^+). From the Figure 5.6a, it was noticed that the F/F^+ ratio increases as the anodization duration increases from 2h to 6h, and then decreases as the anodization duration further increases to 10 h at 8 °C. But in the case of those PAA membranes synthesized at 18 °C, an increasing anodization duration from 2h to 10 h, F/F^+ ratio decreases. F/F^+ ratio is closely related to the regularity ratio of PAA, F^+ and F centers might be present in the pore walls and barrier layers of PAA (Chin et al., 2015). It is easier for PAA to obtain free electrons from anions (OH^- and O^{2-}) in the electrolyte with higher regularity ratio, which increases the possibility for the conversion of F^+ to F centers. This was considered to be the reason for the increased concentration of F centers relative to that of F^+ centers. This idea could explain the observed trend where F/F^+ ratio increases with the regularity ratio of PAA, at 8 °C (Figure 5.6b) and at 18 °C (Figure 5.6c).

Table 5.3.1 PL data analysis of PAA membranes. The maximum peak positions of the PAA membranes (λ), band1 (λ_1) and band2 (λ_2) are presented.

Temp (°C)	Anodization duration (h)	λ (nm)	λ_1 (nm)	λ_2 (nm)
8	2	419	397	419
8	6	424	404	434
8	10	419	396	419
18	2	469	425	483
18	6	446	421	469
18	10	435	426	470

5.4 EFFECT OF ELECTROLYTE CONCENTRATION

Figure 5.7 shows the optical absorbance spectra of the PAA obtained by varying electrolyte concentration, which was measured using UV-Vis photometer at room temperature. Absorbance was found to slightly shift towards the higher wavelength side with increasing electrolyte concentration. The maximum absorbance occurs for PAA obtained in 0.1 M and minimum for those which were formed in 0.5 M electrolyte con-

centration. Results show that, with increasing electrolyte concentration the oxalic acid solution features showed different optical absorbance behaviour, among them only one absorbance band appeared (Figure 5.7). It was revealed that the $H_2C_2O_4$ with different concentrations would have different existing forms in water (Tao et al., 2003). Therefore, it was reasonable to infer that for all PAA (0.1-0.9 M), there are several kinds of incorporated oxalic impurities with different existing forms, having different optical transition probability and activity (Figure 5.7). The band gap energy of PAA calculated using Taucs relation (Qurashi, 2013), for 0.1, 0.3, 0.5, 0.7 and 0.9 M of PAA were 3.68, 3.20, 2.79, 2.75 and 2.75 eV respectively. To evaluate the effect of electrolyte con-

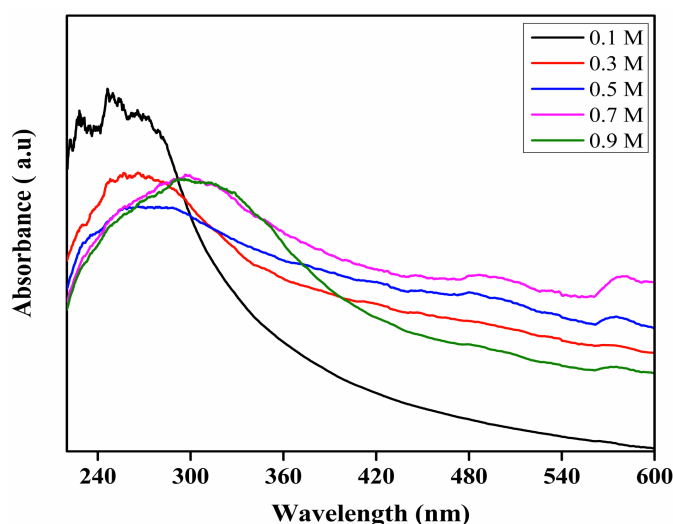


Figure 5.7 UV-Visible spectra of PAA membranes at different electrolyte concentrations (0.1-0.9 M)

centration, the PL wavelength spectra of the PAA obtained in oxalic acid at different electrolyte concentrations (0.1-0.9 M) were shown in the Figure 5.8. All the spectra of Figure 5.8 were formed at 320 nm excitation wavelength of a Xe lamp, PAA formed in 0.3 M shows a strong peak in the blue region. These results indicate that electrolyte concentration has a strong influence on the light-emitting property of the PAA. It was noticed that, the intensity of PL peak was maximum for 0.3 M oxalic acid, as compared with PL peaks for other electrolyte concentrations (0.1, 0.5, 0.7 and 0.9 M). It was found that the microstructural features of the membranes formed in different electrolyte concentrations was different. Different electrolyte concentration can lead to different anodic current during anodization (Zhou et al., 2012). This affects the local environ-

ment of the oxygen positions, hence slight changes in the PL peaks of the membranes formed at different electrolyte concentrations. According to the previous studies, the presence of oxygen positions (F, F^+) were considered to be responsible for observed

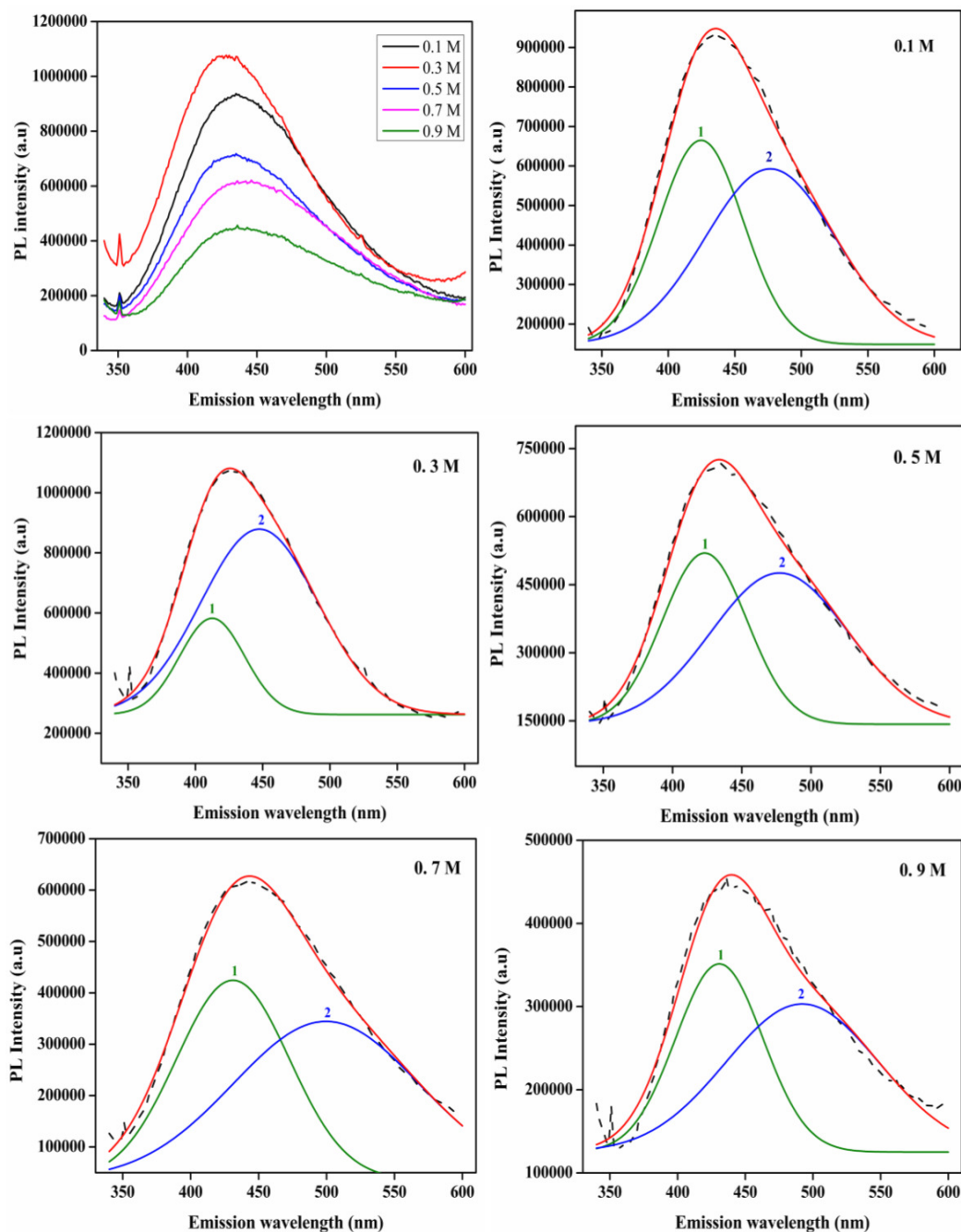


Figure 5.8 PL spectra of the PAA membranes obtained at different electrolyte concentrations (0.1-0.9 M) (a) under a constant potential of 40 V and Gaussian analysis of PAA membranes at 0.1 (b), 0.3 (c), 0.5 (d), 0.7 (e) and 0.9 M (f).

PL in the anodic alumina (Liu et al., 2009). In order to investigate the origins of the

PL peak in alumina, each PL peak is studied using Gaussian fitting analysis (Figure 5.8b-5.8f). The PL spectra attained in all these cases were divided into two Gaussian distributions. Besides these two bands, a small peak was observed at 350 nm for all membranes. This may be due to oxalic impurities ($C_2O_4^{2-}$) incorporated into the PAA during the anodization process. These ions can partly replace the O^{2-} in the oxide as substitutions or impurities during anodization, which can be transformed into luminescent centers because of self-organization the pores (Tao et al., 2003). PL intensity of the two bands varies with electrolyte concentration, representing two bands having different origins. The shift of the PL peak positions varies with electrolyte concentration, maximum for 0.7 M (84 nm) and minimum for 0.1 M (35 nm) between two bands (1 and 2) shown in the Figure 5.8. This shift cannot be caused by one type of defect center but arises from different defect centers existing in PAA.

The peaks at high energy side (2.85 eV- 0.5 M) correspond to F^+ center (labeled as -1) oxygen position with one electron and low energy side (2.44 eV- 0.7 M) is related to the F (labeled as -2) oxygen position with two electrons. The intensity of these two peaks varies with the electrolyte concentration of oxalic acid. This suggests that the relative densities of F and F^+ centers have an affinity to increase or decrease correspondingly with increase of the electrolyte concentration of the oxalic acid. The PL intensity of F^+ centers (0.1-423, 0.3-412, 0.5- 423, 0.7-431 and 0.9 M-430 nm) varies with electrolyte concentration which are in violet region, where as F centers of 0.7, 0.9 M are 499, 492 nm which are near to green region and 0.1, 0.3, 0.5 M are 476, 447, 477 nm which are in blue region. It was clearly visible in the chromaticity diagram analysis of PAA in the Figure 5.8a-5.8c).

Moreover, the coordinates of the PAA estimated using the international commission on illumination (CIE) 1931 (Yang et al., 2014) and color functions are represented in Figure 5.9(a-c). The chromaticity coordinates were calculated for λ_{max} , λ_1 (F-center) and λ_2 (F^+ -center) all the membranes obtained at 0.1, 0.3, 0.5, 0.7 and 0.9 M respectively under an excitation wavelength of 320 nm. It was observed that all the samples have blue emissions color. In the case of F^+ centers, PL peaks for PAA obtained in 0.7 and 0.9 M appeared near to red region. At low concentrations (0.1-0.3 M), density of F

centers is larger, due to lower currents and further oxygen positions trap two electrons. Whereas at higher concentrations (0.5- 0.9 M), density of F^+ centers is large, because of large currents and oxygen positions trap only one electron. Hence, the distribution of two kinds of defects in the membranes were different for different samples. The

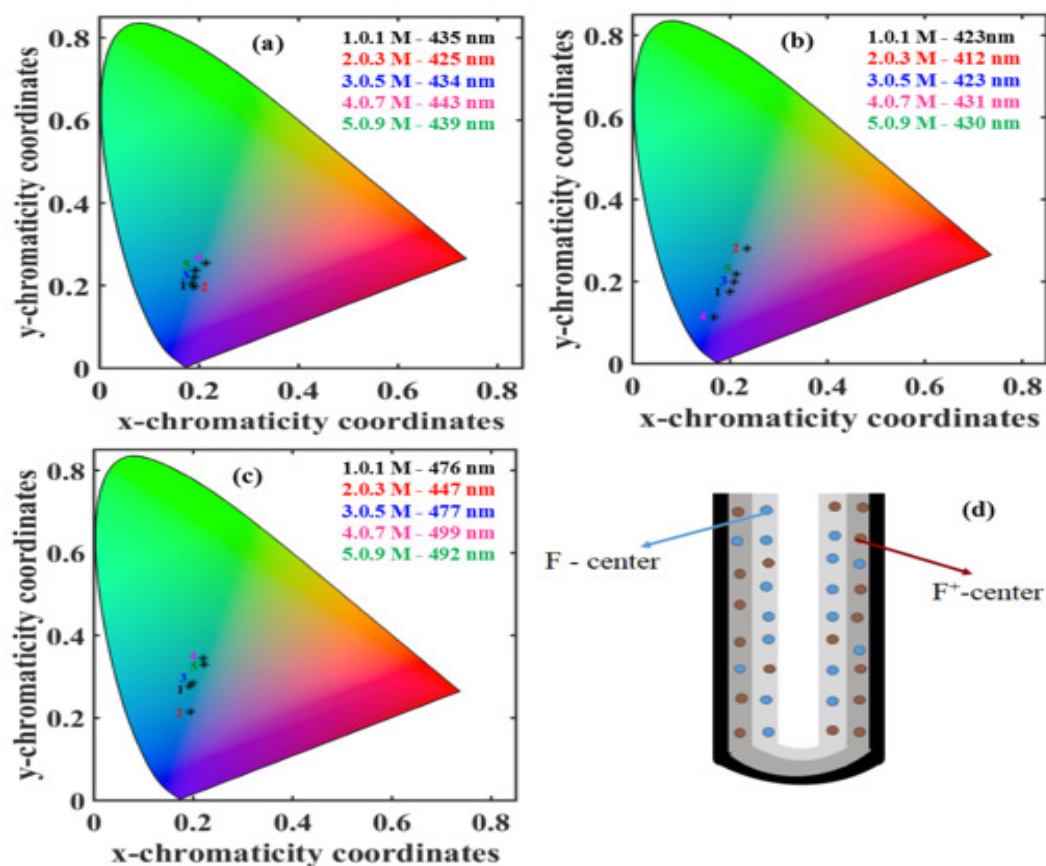


Figure 5.9 CIE chromaticity diagram for (a) maximum wavelength (max), (b) F^+ centers, (c) F centers for PAA obtained at different electrolyte concentrations and (d) Defect-distribution model of PAA.

concentration of F centers is more on the surface, followed by gradual decrease with decrease in the pore wall thickness. The condition for F^+ centers is just reversed. Our results show that, PL peak position of F and F^+ centers varies in asymmetric manner with electrolyte concentration, indicating that the distribution of defects in the membranes is inhomogeneous (Huang et al., 2003). This represents the presence of F and F^+ centers on the pore walls of PAA. From PL spectra of PAA, the values of F and F^+ centers were noticed in Table. 3.

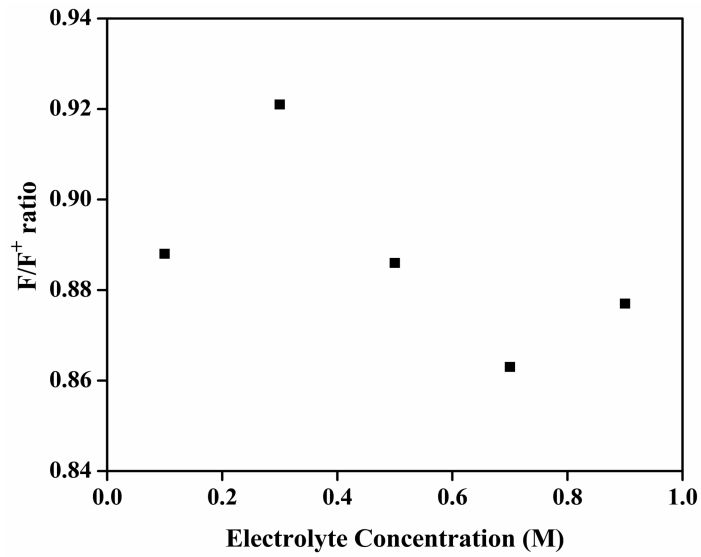


Figure 5.10 Effect of electrolyte concentration on F/F^+ ratio of PAA membranes.

The PL intensity ratio (F/F^+) plotted as a function of electrolyte concentration to study the competition in the charge carrier transport between the F^+ transition and F transition centers is shown in Figure 5.10. The F/F^+ ratio is maximum for 0.3 M, further increasing electrolyte concentration to 0.7 M, the PAA shows a large reduction in this ratio. This may be due to intensity of F^+ centers increasing with electrolyte concentration as compared with F centers. The plot of regularity ratio verses PL intensity ratio of F/F^+ is shown in the Figure 5.11. The conversion of F^+ to F centers

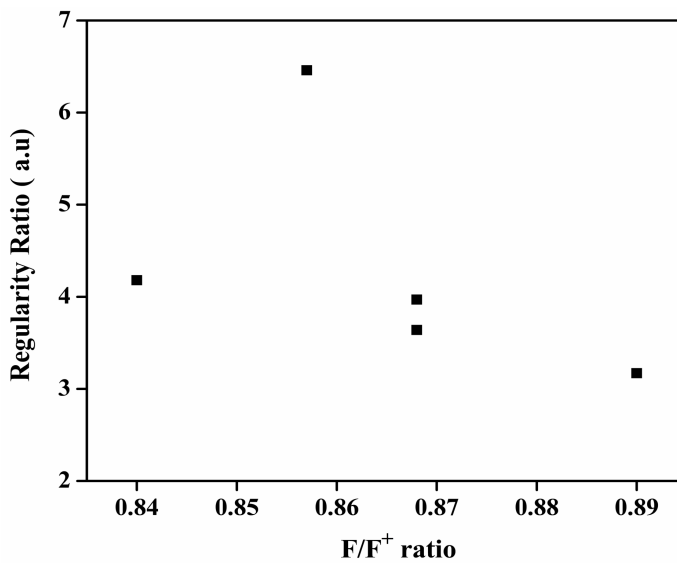


Figure 5.11 Relationship of regularity ratio and F/F^+ ratio PAA membranes.

increases with high regularity ratio (0.3 M), because it is easier for PAA to obtain free electrons from anions (O^{2-} and OH^-) in the electrolyte with high regularity ratio and these centers are present at pore walls (F^+) and barrier layers (F) of PAA (Chin et al., 2015). From the illustration, it is obvious that F/F^+ ratio increases with the regularity ratio from 0.1 to 0.3 M, and then decreases from 0.5 to 0.9 M. These results may be quite useful for the structural tuning ability to control over the PL properties of alumina membranes. PL and regularity ratio of PAA membranes were presented in the Table 5.4.1 and Table 5.4.2.

Table 5.4.1 PL data of PAA membranes for different electrolyte concentrations (0.1-0.9 M)

Electrolyte concentration (M)	λ_{max} (nm)	$F(\lambda_1)$ (nm)	$F^+(\lambda_2)$ (nm)
0.1	435	423	476
0.3	425	412	447
0.5	434	423	477
0.7	443	431	499
0.9	439	430	492

Table 5.4.2 PL and regularity ratio analysis data of PAA membranes for different electrolyte concentrations (0.1-0.9 M)

Electrolyte concentration (M)	F/F^+	Regularity ratio (a.u)	PL Intensity (a.u)
0.1	0.888	3.17	949902
0.3	0.921	6.46	1106567
0.5	0.886	3.97	646630
0.7	0.863	4.18	533141
0.9	0.877	3.64	401919

5.4.1 Conclusions

1. The absorption spectra of PAA slightly moves towards higher wavelength side with increasing electrolyte concentration. PAA membranes obtained in oxalic acid exhibit asymmetric luminescence band within 300-600 nm wavelength range in blue region. Gaussian analysis of this spectrum show two sub bands originating from two types of oxygen-deficient centers.
2. Increased anodization duration widens the PL spectra and reduces the PL behaviour of PAA membranes in the visible region. This spectrum was divided into two sub-bands by Gaussian analysis, originating from two kinds of oxygen-deficient centers, F^+ and F centers respectively.
3. F/F^+ ratio of PAA membranes attained highest value for 6h anodization duration at 8 °C and for 2h anodization duration at 18 °C. F/F^+ ratio increased with the regularity ratio of PAA, which might be due to its improved capability to accept free electrons from electrolyte followed by conversion of F^+ centers to F centers.
4. Two PL emission bands could be observed from PAA formed in different electrolyte concentrations at 420 (F^+) and 470 nm (F), PAA grown by 0.3 M in oxalic acid has the highest F/F^+ ratio. In addition to these bands, a small peak was observed at 350 nm, this may be due to oxalic impurities incorporated into the PAA during the anodization process. F/F^+ ratio increases with RR of PAA from 0.1 to 0.3 M and then decreases. This is due to its enhanced capability to obtain free electrons allowing F^+ centers to get converted into become F centers.

Chapter 6

GROWTH OF DIFFERENT NANOSTRUCTURES USING PAA MEMBRANES

This chapter illustrates the applications of alumina based nanostructures. It begins with the wettability analysis of alumina nanostructures and also it discuss the synthesis of metal nanostructures such as copper and silver nanowires grown on alumina membranes using electroless deposition method.

6.1 INTRODUCTION

Now a days, the fabrication of surfaces with special wettability, as well as super hydrophobicity, has attracted great research attention because these surfaces have high potential for use as self-cleaning surfaces in micro fluidics and droplet based technologies (Barberoglou et al., 2010). A surface is called super hydrophobic when the effective contact angle (CA) of a liquid water droplet with the surface exceeds 150° and, on the other hand, super hydrophilic when the CA is smaller than 10° (Yuan and Lee, 2013). For the fabrication of super hydrophobic materials, a low surface energy material is regularly merged with a surface having hierarchical geography at the nanometer and/or micrometer scale. In recent years, solids with nanometre-scale pores have become well-known members for producing super hydrophobic surface due to their inherent surface roughness (Tasaltin et al., 2011). Surface wettability property is considered to be managed by both the chemical composition and geometrical arrangement of solid surfaces

(Feng et al., 2002). The correlation between the structural attributes and the surface wettability of PAA arrays with changing anodization and pore widening duration was studied.

Metallic nanowires are a subject of relevant interest due to their promising applications in nanosensors, nanoactuators, and nanocarriers (Yan et al., 2011), (Yao et al., 2008). The high aspect ratio of metallic nanowires confer them outstanding properties and enhanced versatility promoting applications in diverse fields. Metallic nanowires can play an important role in the middle scale of 10-200 nm to connect molecular scale devices to the macroscale world (Pena et al., 2000), and to connect elements in nano-electronics, due to rapid decrease in size of electronic devices. In the present study, synthesis of metallic nanostructures such as Ag and Cu inside the pores of PAA membranes were studied in detail.

6.2 WETTABILITY ANALYSIS

6.2.1 Effect of anodization duration

To understand how the interfacial features influence the introduction of water molecules on PAA, it is necessary to carry out a careful study of the nature of the liquid-solid interface. Here, the contact angle (CA) has been used as an evaluation of wetting between a liquid and a solid surface (Redon et al., 2005). With increasing anodization duration, the average pore diameter and the surface porosity of PAA membranes was found to increase. With increasing pore diameter contact angle varies in a linear manner. Initially the water drop is able to go into the pores, with increasing pore size, However gradually air is trapped in the pores leading to the higher contact angle (Leese et al., 2013). To study the effect of the anodization duration on the wetting of PAA membranes in detail, we measured the CA for PAA membranes for different anodization durations such as 2h, 6h and 10h at 8 °C and 18 °C. Figure 6.1 shows the wettability behaviour of PAA membranes formed at different anodization durations. From Figure 6.1, it is to be noted that, PAA membranes show hydrophilic nature with contact angles 70.40°,

76.08° and 74.85° for 2h, 6h and 10h respectively at 8 °C. In addition, PAA membranes prepared at 18°C also show hydrophilic nature with contact angles 74.03°, 79.53° and 78.07° respectively for 2h, 6h and 10h. Surface free energy of PAA membranes were measured using Youngs equation (γ_s , eq.no 2.4.2) (Rudawska and Jacniacka, 2009) and these calculated values are given in Table 6.2.1. Surface energy values vary from 32.45

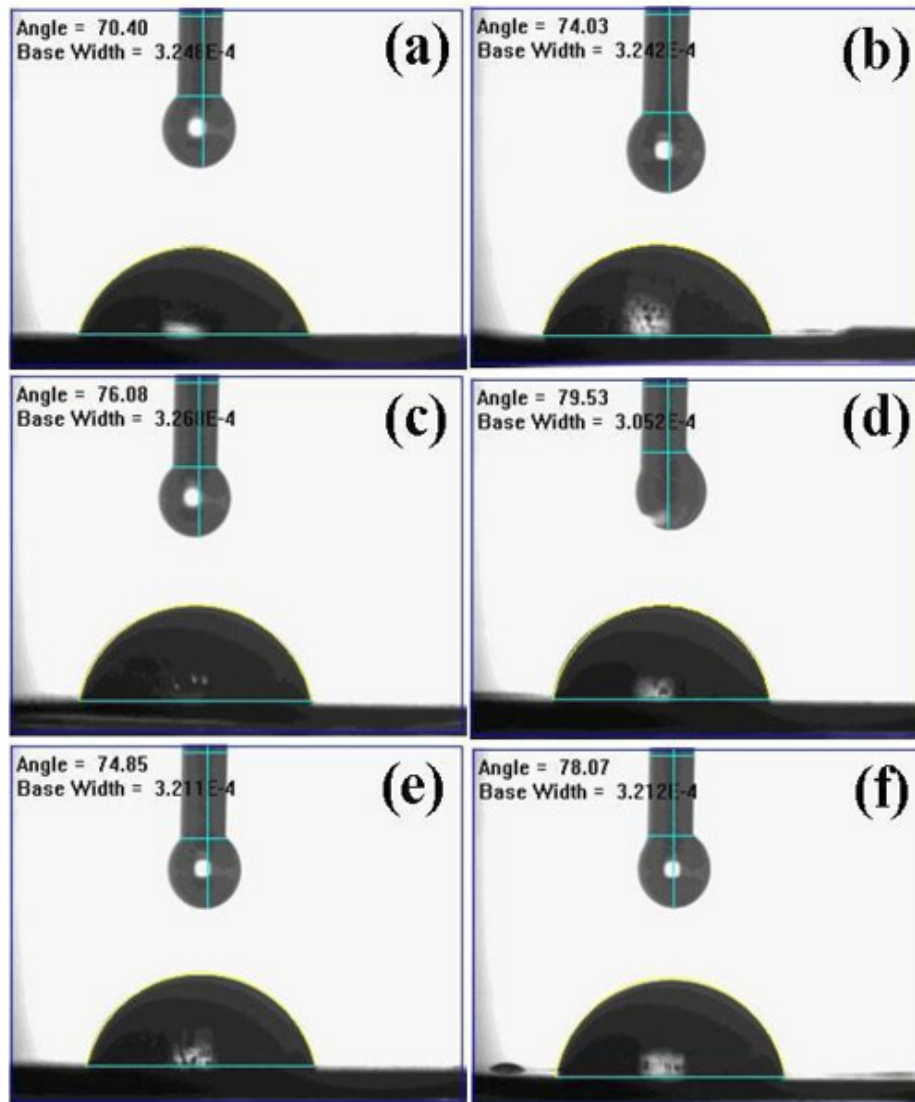


Figure 6.1 Shows contact angle measurement images of PAA membranes obtained at different anodization durations. (a) 2h, (c) 6h, (e) 10h at 8 °C and (b) 2h, (d) 6h, (f) 10h at 18 °C.

to 28.95 mJ/m^2 for PAA membranes obtained at 8 °C and it varies from 29.59 to 26.50 mJ/m^2 for PAA membranes prepared at 18 °C. It was noticed from the above calculated surface energy values that with increasing anodization duration there is not much

variation in the surface energy values. These PAA membranes are in fact high energy solid materials which may be used for coloring and coating applications.

Table 6.2.1 Surface energy values of the obtained PAA membranes.

<i>Temp.</i> (°C)	Anodization duration (h)	Surface energy (<i>mJ/m²</i>)	Pore diameter (nm)	Contact angle (°)
8	2	32.45	64	70.40
8	6	28.00	71	76.08
8	10	28.95	73	74.85
18	2	29.59	61	74.03
18	6	25.41	66	79.53
18	10	26.50	69	78.07

6.2.2 Effect of pore widening duration

To study the effect of a pore widening on the wetting properties of PAA membranes, we etched the PAA membranes in 5wt% phosphoric acid at 30 °C. In the present study PAA membranes were prepared using oxalic and sulphuric acid as electrolytes with anodizing potential of 40v and 20 V at 8 °C. The wetting of the PAA surfaces is largely dependent on the surface porosity (Buijnsters et al., 2013). With increasing pore widening duration, the pore wall thickness decreases and as a result of both the average pore diameter and the surface porosity increase. The pore widening results in a shift of the contact angle (CA) toward higher values for PAA membranes. To examine the effect of the pore opening on the wetting of PAA in more detail, we varied the etching time (60 min, 120 min) and the resulting oxide membranes were studied. Figure 6.2 shows the wettability behaviour of PAA membranes formed at different pore widening durations. The measurement on water contact angles (CA) at room temperature are recorded in the Table 6.1. From Figure 6.2, it was evident that, PAA membranes show hydrophilic behaviour with contact angle 21.50° and 21.30° for sulphuric acid and oxalic acid respectively without pore widening. Furthermore with increasing pore widening duration from 0 min to 120 min contact angles varies from 21.50° to 54.02° for sulphuric acid and to 21.30° to 72.07° for oxalic acid showing hydrophilic nature. In addition, PAA membranes prepared using oxalic acid show hydrophilic behaviour and sulphuric acid shows super hydrophilic nature with contact angles 17.04° and 6.00° in

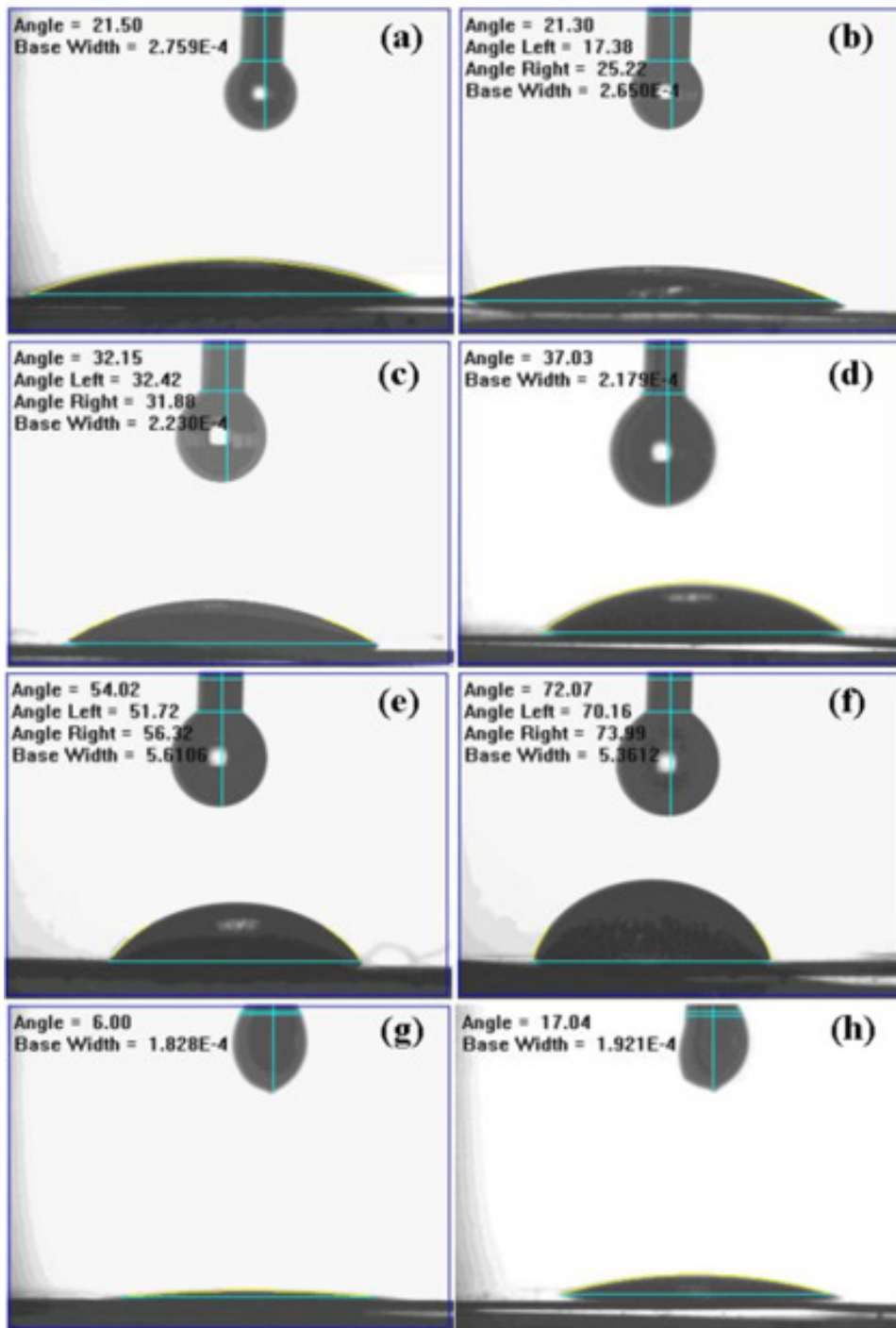


Figure 6.2 Contact angle measurement images of PAA membranes formed at different pore widening durations: Without pore widening (a). Sulphuric acid and (b). Oxalic acid; 1 hr pore widening (c). Sulphuric acid and (d). Oxalic acid; 2 hr pore widening (e). Sulphuric acid and (f). Oxalic acid; In acetone medium (g) Sulphuric acid (h) Oxalic acid.

acetone medium. The surface energy of the PAA membranes was then calculated from Young's equation (γ_s , eq.no 2.4.2) (Rudawska and Jacniacka, 2009). It showed variation between 45.23 to 68.67 mJ/cm^2 for sulphuric acid and 30.69 to 66.69 mJ/cm^2 for oxalic acid respectively (Table 6.1). From the wettability studies in acetone medium, the surface energy values for oxalic acid was found to be 68.67 and for sulphuric acid 71.39 mJ/cm^2 respectively. From the CA images and the obtained values of contact angle, we can notice that the contact angle is directly influenced by the surface structure of the film.

Table 6.2.2 Contact angle data for PAA membranes formed in 0.3 M of oxalic and sulphuric acid at different pore widening durations.

Pore widening (min)	Contact angle ($^\circ$)		Surface energy (mJ/cm^2)		Pore diameter (nm)	
	SA	OA	SA	OA	SA	OA
0	21.50	21.30	66.87	66.96	18	52
60	32.15	37.03	61.19	58.04	28	62
60	6 (Ace)	17.04 (Ace)	23.56	22.67	28	62
120	54.02	72.07	45.23	30.69	38	68

6.3 SILVER NANOPARTICLES

PAA membranes were prepared using two-step anodization process. The remaining aluminium substrate was removed using saturated $CuCl_4$ solution after the pore widening process. Then 0.5 M of silver nitrate solution was injected into the pores of PAA membrane and dried at room temperature. Finally the membrane was annealed with a heating rate of 40 $^\circ C/min$, at 500 $^\circ C$ for 4h. Figure 6.3a shows the FE-SEM micrograph of PAA membranes formed in 0.3 M of oxalic acid by two-step anodization process and the corresponding cross sectional image is shown in Figure 6.3b. Hexagonal array of pores were obtained with an average diameter of about 60 nm and interpore distance 134 nm. The circular pores are distributed on the entire surface, uniform pore size and highly ordered pore arrangement was observed over a large area. Moreover to study the surface morphology, 2D FFT images were generated for PAA and Ag-PAA using WSxM software (Stepniowski et al., 2014c).

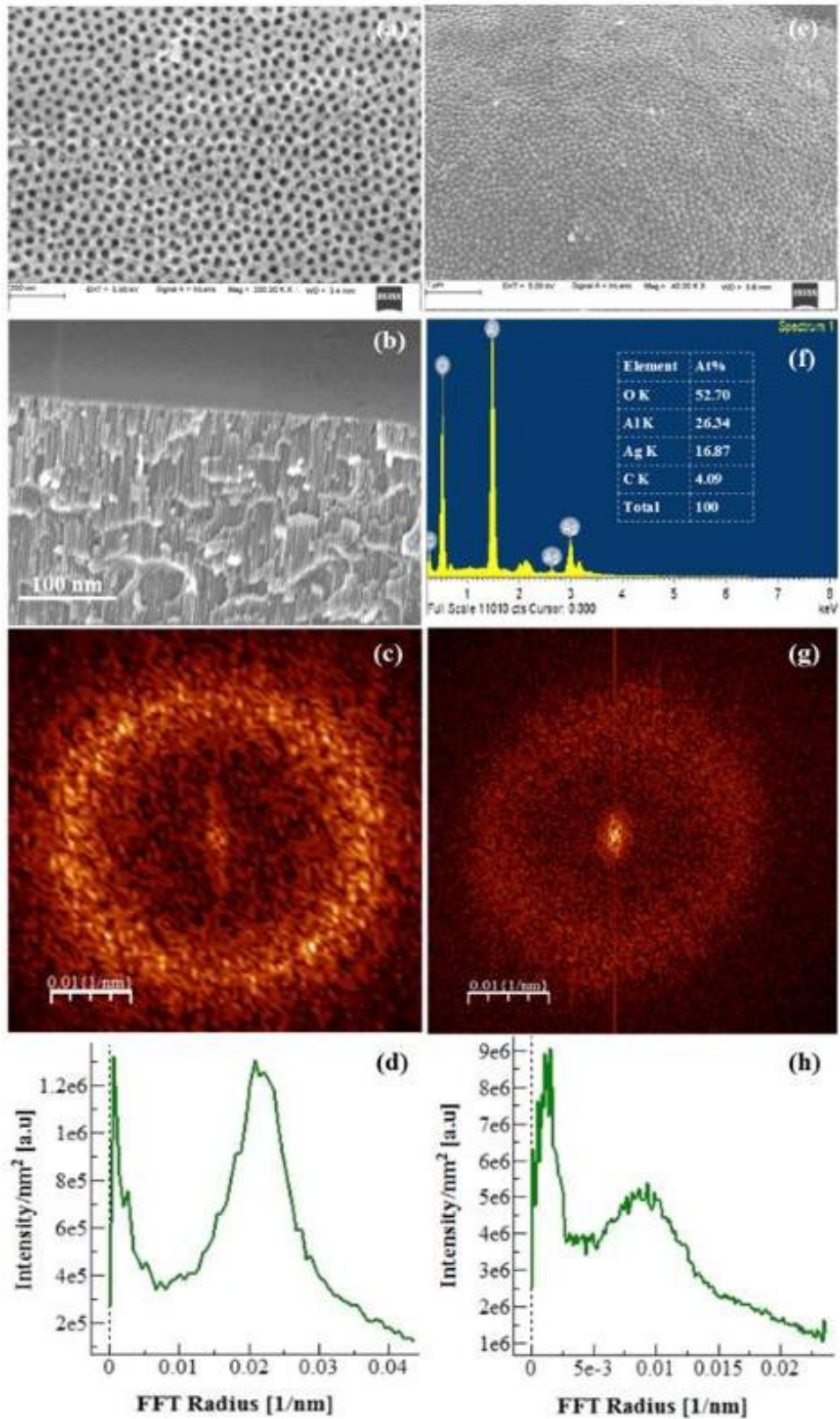


Figure 6.3 FESEM images (a, e), Cross-sectional image (b), EDAX (f), 2D FFT images (c, g) and radial averages (d, h) of PAA and Ag-PAA

Radial average was estimated for each FFT image to measure regularity ratio (RR) of pores. RR was calculated using the expression (R , eq.no 1.5.1) (Stepniowski et al., 2014c), the analysis of FFT images indicated that a blurred ring for PAA (Figure 6.3c) and Ag-PAA (Figure 6.3g). For an ideal hexagonal arrangement of pores, FFT pattern consists of six points on the ring perimeter. The better arrangement was not observed in both cases of PAA and Ag-PAA, because of which the shape of FFT pattern was a blurred ring. It was noticed that intensity of radial average was more in the case of Ag-PAA (Figure 6.3h) compared with that of pure PAA (Figure 6.3d). Silver nanoparticles obtained by electroless deposition in 0.5 M of silver nitrate solution was shown in the Figure 6.3e. Figure 6.3e represents the fact that the Ag nanoparticles were grown inside the pores of the PAA membrane. These Ag nanoparticles were nearly spherical in shape and uniformly distributed over a large area of the membrane. In order to further confirm the existence of silver nanoparticles, the Energy dispersive X-ray (EDX) spectroscopy of the sample was analyzed. The signal of Ag appeared shown in the Figure 6.3f.

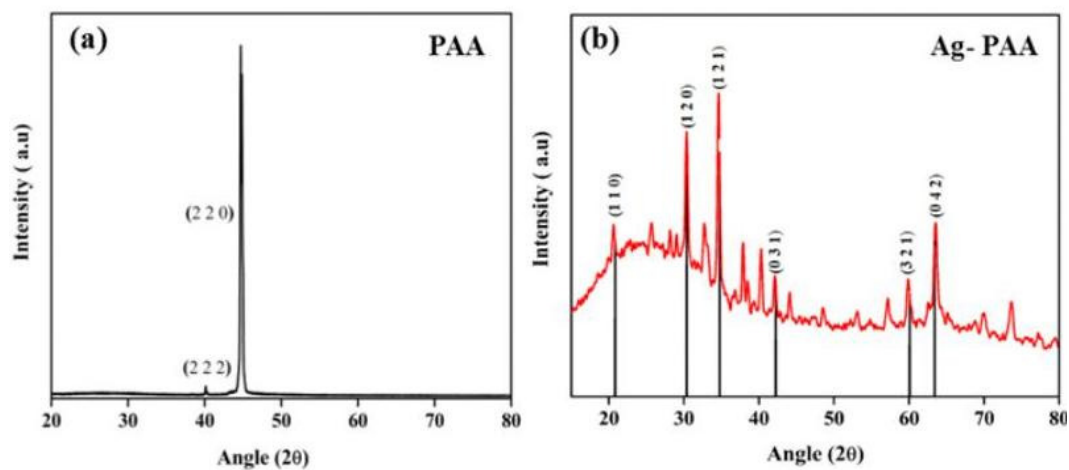


Figure 6.4 XRD pattern of (a) PAA and (b) Ag-PAA.

The signals of Al and O elements were also shown in the EDX pattern. The trace of carbon element is due to the adsorption of the oxalic acid on the aluminium cathode (Gan et al., 2016). The atomic ratio of aluminium to oxygen was about 1:2, which was characteristics of the Al_2O_3 in the PAA membrane. XRD patterns of PAA (Figure 6.4a) and Ag-PAA (Figure 6.4a) was shown in the Figure 6.4. The XRD analyses show that the diffraction peaks of pure Al_2O_3 with aluminium substrate were located at 40.05°

and 45.08° corresponding to the planes (2 2 2) and (2 2 0) matching with JCPDS data (01-1304). These results reveal that as prepared PAA membrane with Al substrate in oxalic acid was amorphous in nature (Reddy et al., 2016). As shown in the Figure 6.4b, six reflection peaks correspond to the Ag-PAA crystalline were observed. The six reflection peaks were assigned to diffraction from $2\theta = 20.68^\circ$ (1 1 0), $2\theta = 30.38^\circ$ (1 2 0), $2\theta = 34.75^\circ$ (1 2 1), $2\theta = 42.23^\circ$ (0 3 1), $2\theta = 60.06^\circ$ (3 2 1) and $2\theta = 63.39^\circ$ (0 4 2) planes of Ag-PAA respectively and matched with JCPDS data (21-1070). From the width of the peak (1 2 1), the diameter of the silver nanoparticles was estimated to be about 26.78 nm by using Scherrer formula eq.no 2.3.2 (Kumar et al., 2013).

6.4 ALUMINA NANOWIRES

To prepare alumina nanowire (ANW) array, anodization process was carried out in 0.5 M electrolyte concentration, with anodization potential of 40 V and 20 V, duration of 6 h in both oxalic and sulphuric acid solutions. After the anodization process PAA membranes were etched in 1 M of phosphoric acid for 45 min. Immediately, the formed alumina nanowires were annealed in air for 2h at 60°C .

ANW arrays were produced from PAA membranes by chemically etching the samples in phosphoric acid solution (Han et al., 2007). The schematic illustration of the formation of the of alumina nanowires was shown in the Figure 6.5. Figure 6.5a

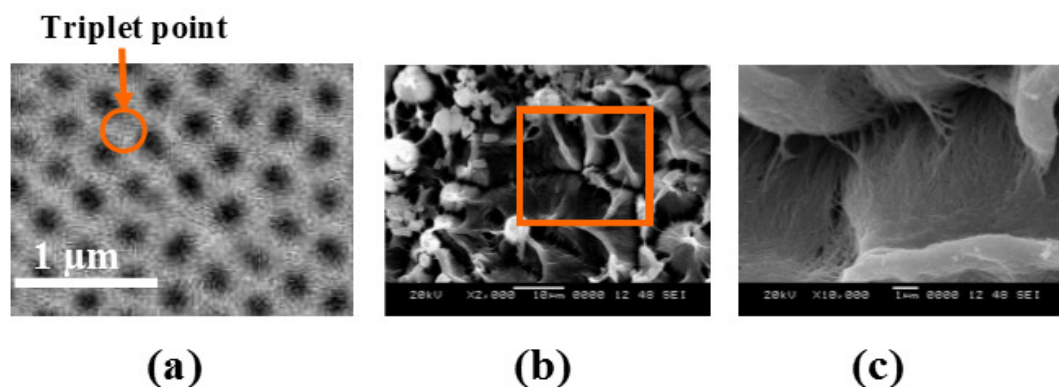


Figure 6.5 Schematic of the formation of the ANW from APA: (a) porous structure of the APA with triplet point, (b) Thinning of pore walls after dissolution of PAA in H_3PO_4 solution, (c) Alumina nanowires formation from triplet points.

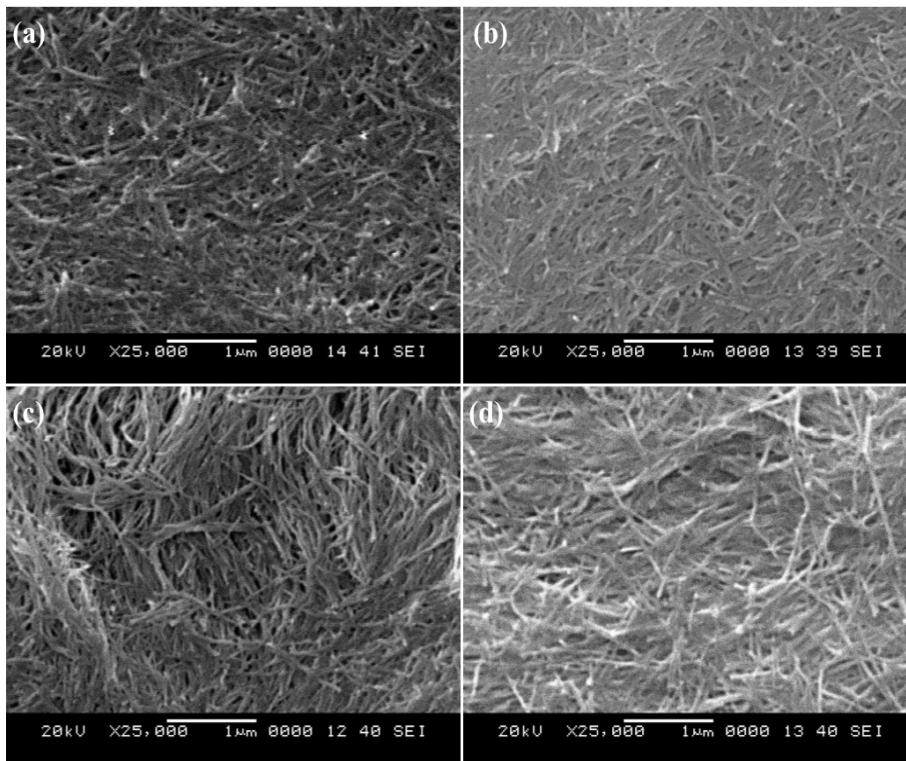


Figure 6.6 SEM micrographs of the ANW formed in sulphuric and oxalic acid with the dissolution of APA membranes 30 (a, b) and 45 min (c, d) in H_3PO_4 solution.

shows the PAA membranes with hexagonal array of pores, formed in 0.5 M of oxalic acid. During the dissolution of alumina membranes in phosphoric acid, pore walls linking three neighboring cells (triplet point) undergo thinning as shown in the Figure 6.5b after the dissolution of 10 min. Further increasing etching time from 10 min to 20 min, the thinning walls are broken and triplet points are separated as shown in the Figure 6.5c. After 30 min, the pore walls are dissolved and only nanowires remaining, which are generated from triplet points of the pores observed in oxalic (Figure 6.6b) and sulphuric acid (Figure 6.6a) respectively. Finally, after 45 min dissolution, the PAA membrane is completely dissolved, dense alumina nanowires were observed in oxalic (Figure 6.6d) and sulphuric acids (Figure 6.6c) with the same orientation. The thickness of the PAA membranes can influence the morphology of the alumina nanowire arrays. The nanowires have uniform diameter with a thickness less than 10 nm, and length is below 5 μm in oxalic and sulphuric acid, which is related to the original thickness of alumina membrane. Formation of the ANW corresponds to the splitting of the wall surroundings of the pores. The number of pores on the surface of the PAA membranes

is larger, compared with the interface between the PAA membrane and Al substrate in the first step anodization (Mei et al., 2005). It is inferred that the wall between the pores is thinner near to the surface as compared with the beneath. Splitting between the pores is more likely to be near to the surface, because the pore density is high near to the surface. The number of ANW array depends on the number of pore walls split. In our studies the number of pore walls splitting is more in sulphuric alumina (Figure 6.6c) as compared with oxalic alumina (Figure 6.6d), due to smaller wall thickness in sulphuric alumina (17 nm). It may be emphasized that growth of nanostructures on the PAA membranes without the need to implant materials is the significant feature of the present work. These alumina nanowires are suitable for applications in various fields, such as catalyst, electrolytic capacitors and negative electrodes of Li-ion batteries (Kondo et al., 2016).

6.5 COPPER NANOWIRES

6.5.1 Synthesis of Cu nanowires inside the pores of PAA membranes

Figure 6.7 gives a schematic diagram of copper nanowire array grown in to the pores of PAA via electroless deposition process. Highly ordered PAA (Figure 6.7a) was obtained by two-step self-organized anodization process in 0.3 M of oxalic acid with anodization potential of 40 V. After pore widening of PAA for 30 min in 5 Wt% H_3PO_4 , it was found that the pore diameter was ~ 68 nm with thickness ~ 110 μm . Removal of barrier layer using saturated copper chloride solution was shown in the Figure 6.7b. Then 0.5 M of copper nitrate solution was injected into the pores of free-standing PAA and dried at room temperature (Figure 6.7c) for 2h. Finally copper nanowires were obtained inside the pores of PAA after annealing the sample at 60 C for 4h was shown in the Figure 6.7d. During the annealing time, copper nitrate solution undergo thermal decomposition in the presence of excess of oxygen leading to the formation of copper nanowires. Thermal decomposition of copper nitrate solution near to the alumina surface is given below:



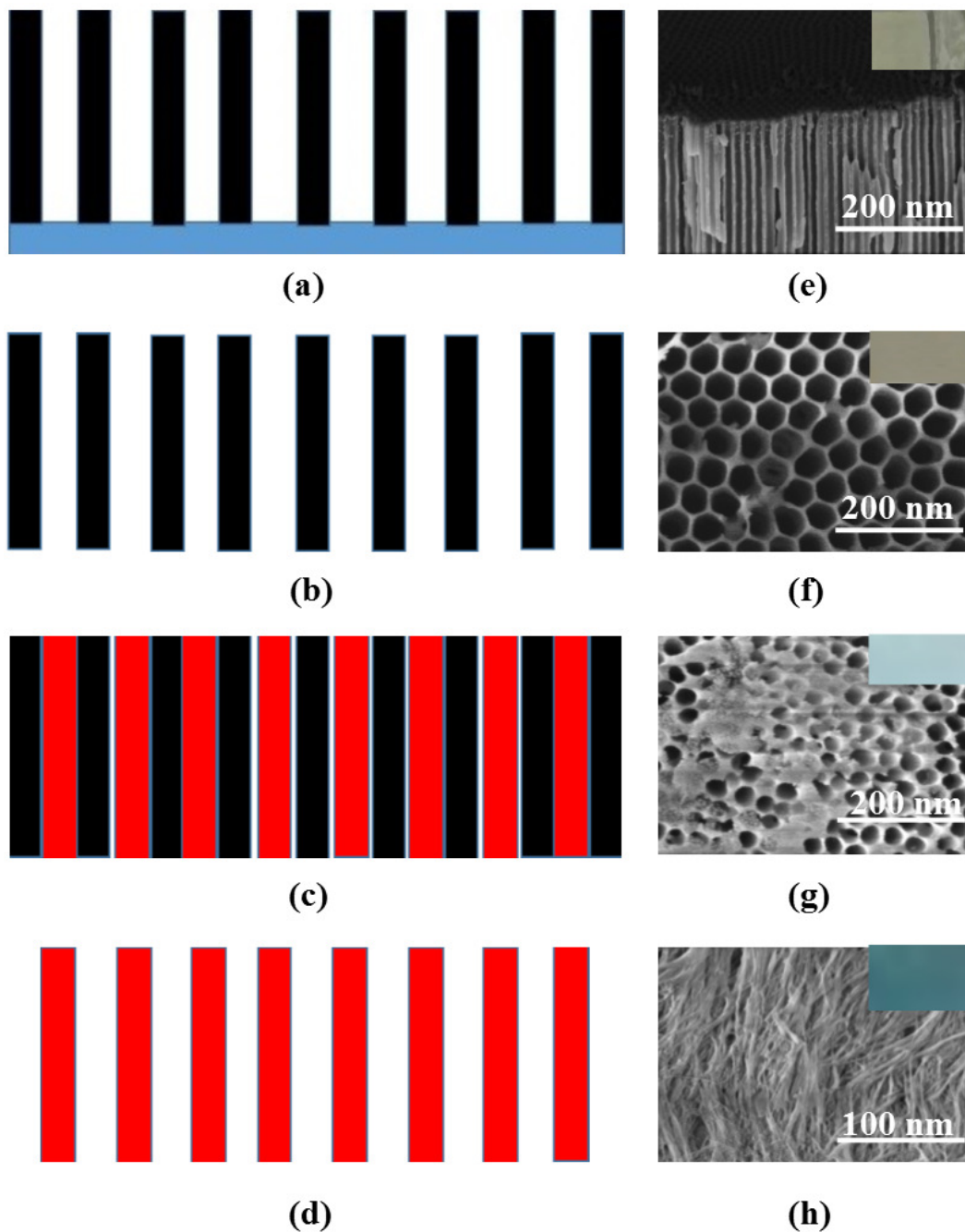


Figure 6.7 Schematic of synthesis of Cu nanowires into the pores of PAA. (a) PAA with highly ordered pores, (b) Free standing PAA film, (c) Electroless deposition of copper nitrate solution into the pores of PAA and (d) Formation of Cu nanowires. The corresponding FE-SEM images and variation of color (inset) of the sample for each step (e, f, g and h) of fabrication of Cu nanowires.

The conversion of the formed copper oxide into the pure copper nanowires after 4h continuous annealing was confirmed from the color change (Figure 6.7h) of the sample and also from the EDX analysis. The corresponding FESEM images of PAA and variation of color of the sample (Inset) for each step was illustrated in Figure 6.7e, 6.7f, 6.7g and 6.7h respectively. The main advantage of this method is to avoid the complex process of Al and barrier layer removal prior to deposition.

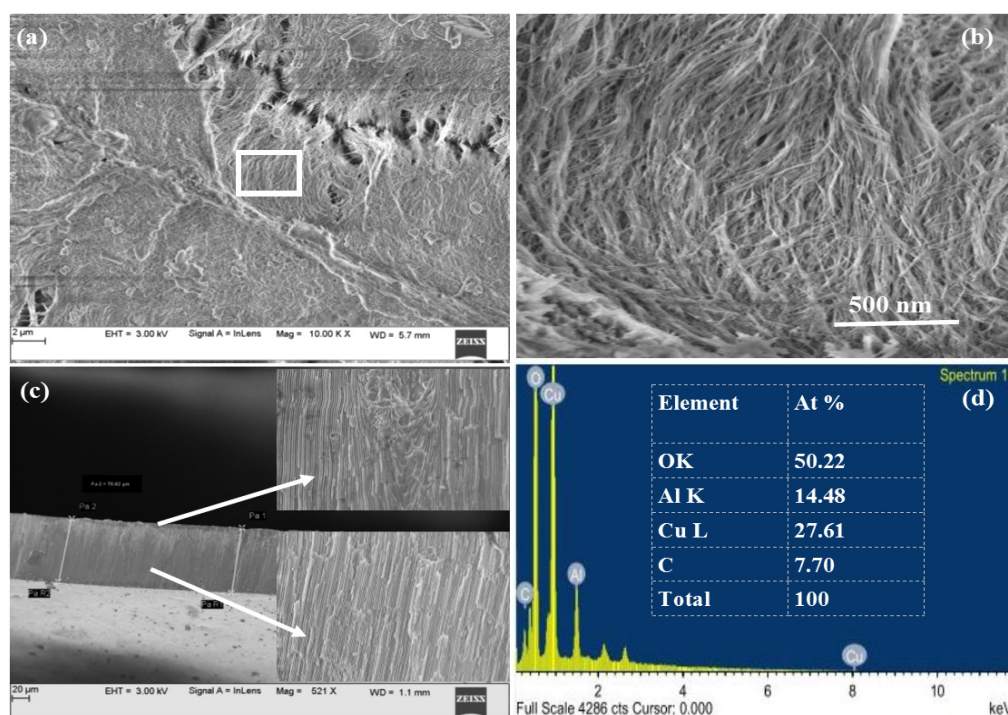


Figure 6.8 (a) FE-SEM images of copper nanowires grown inside the pores of PAA, (b) Higher magnified image of randomly oriented Cu nanowires, (c) Variation of cross-sectional image PAA before and after growth of Cu nanowires and (d) EDX spectra of Cu nanowires.

Figure 6.8 shows the typical FE-SEM images of free standing Cu nanowires fabricated into the pores of PAA by electroless deposition method (Ren et al., 2007). Cu nanowires grown were highly homogeneous in shape, continuous and uniform throughout the surface of the membrane (Figure 6.8a). Higher magnified Cu nanowire (Figure 6.8b) array reveals that nanowires were randomly oriented on the pores of PAA and tips of the nanowires aggregated into clumps. The cross-section image of PAA was shown in the Figure 6.8c. Inset images illustrate the variation of pore wall before and after deposition of Cu nanowires. It was observed that after deposition of Cu nanowires, pore

wall crushes near to the surface of PAA. The EDX spectra shown in the Figure 6.8d confirms the existence of Cu. The dimensions of Cu nanowires is consistent with the average value of pore diameter of PAA. It may be noted that such copper nanowires have wide ranging applications in gas sensing, field emission and photovoltaic devices, light emitting diodes and thin film solar cells (Rathmell et al., 2010).

6.5.2 Conclusions

1. Contact angle measurements showed that PAA membranes prepared at different anodization durations were hydrophilic in nature and with increasing pore diameter contact angle varied in a linear manner. Due to increasing pore size, progressively air is trapped in the pores leading to the higher contact angle.
2. As the pore widening duration was increased, the contact angle was found to increase in both oxalic acid and sulphuric acids. PAA membranes showed hydrophilic properties in both oxalic acid and sulphuric acid in water medium. In fact, PAA membranes produced in sulphuric acid exhibited super hydrophilic nature which was confirmed through contact angle measurements in the acetone medium.
3. Silver nanoparticles were grown inside the pore of PAA successfully by electroless deposition method. XRD analysis of as PAA shows the amorphous nature, whereas Ag-PAA shows crystalline nature. UV-Visible analysis of PAA was revealed two absorption bands, but in case of Ag-PAA three absorption bands were observed.
4. The wall thickness of the pores played a major role in the formation of ANW array. The number of ANW array obtained in sulphuric alumina was more compared with that obtained from oxalic alumina, due to smaller pore wall thickness in sulphuric alumina.
5. Copper nanowires were grown into the pores of PAA membranes by electroless deposition method. Cu nanowires were randomly oriented through the surface of the membrane and tips of the nanowires aggregate into clumps.

Chapter 7

SUMMARY AND FUTURE DIRECTIONS

The conclusions of the thesis and scope for future directions are presented in this chapter.

7.1 SUMMARY

Preparation and Characterization of PAA membranes

- The effect of process parameters such as anodization duration and electrolyte concentration on pore parameters of PAA membranes were studied systematically.
- Increasing of anodization duration causes the changes in pore dimensions. This was due to the increase in the uniformity of pore structure with the increase of the anodization duration.
- Increasing electrolyte concentration also shows the changes in pore dimensions from 0.1 to 0.3 M in oxalic acid. This can be attributed to growth rate and volume expansion of aluminium oxide that increases with increasing electrolyte concentration.
- The nanopore arrangement was calculated based on the FFT images using WSxM software. From the FFT analysis, it was revealed that the better nanopore arrangement was possible for an optimal anodization duration of 6h and electrolyte concentration of 0.3 M in oxalic acid.

Mechanical properties of PAA membranes

- Highly ordered hexagonal array of PAA membranes were prepared using oxalic and sulphuric acids as electrolytes at 8 °C. Regularity ratio of PAA membranes was more in oxalic acid than in sulphuric acid, due to uniform order of pore arrangement in oxalic acid.
- Micro hardness of PAA membranes produced in sulphuric acid is high, due to the difference between structural composition of PAA formed in oxalic and sulphuric acids. The pile-up developed around the indent in PAA membranes formed in sulphuric acid is more pronounced. This was caused by lower surface roughness and elastic deflection of PAA formed in sulphuric acid. However, nanoindentation does not reveal any major crack formation in PAA membranes prepared in oxalic and sulphuric acids.
- The hardness-contact depth analysis indicates that for oxalic and sulphuric acid cases, hardness decreases with increasing applied load. However, the corresponding hardness remains nearly constant at high loads (4 mN). Young's modulus and nano hardness of PAA in sulphuric acid is higher compared with those of oxalic acid cases. This was attributed to the low porosity and regularity of pores obtained in sulphuric acid.

Optical properties of PAA membranes

- The absorption spectra of PAA slightly moves towards higher wavelength side with increasing electrolyte concentration. In all the cases of PAA membranes obtained in oxalic acid, asymmetric luminescence band within 300-600 nm wavelength range in blue region were obtained. Gaussian analysis of this spectrum show two sub bands originating from two types of oxygen-deficient centers.
- Increased anodization duration widens the PL spectra and reduces the PL behaviour of PAA membranes in the visible region. This spectrum was divided

into two sub-bands by Gaussian analysis, originating from two kinds of oxygen-deficient centers, F^+ and F centers respectively.

- F/F^+ ratio of PAA membranes attained highest value for 6h anodization duration at 8 °C and for 2h anodization duration at 18 °C. F/F^+ ratio increased with the regularity ratio of PAA, which might be due to its improved capability to accept free electrons from electrolyte followed by conversion of F^+ centers to F centers.
- Two PL emission bands could be observed from PAA formed in different electrolyte concentrations at 420 (F^+) and 470 nm (F), PAA grown by 0.3 M in oxalic acid has the highest F/F^+ ratio. In addition to these bands, a small peak was observed at 350 nm, this may be due to oxalic impurities incorporated into the PAA during the anodization process. F/F^+ ratio increases with RR of PAA from 0.1 to 0.3 M and then decreases. This is due to its enhanced capability to obtain free electrons allowing F^+ centers to get converted into become F centers.

Wetting properties of PAA membraes

- Contact angle measurements showed that PAA membranes prepared at different anodization durations were hydrophilic in nature and with increasing pore diameter contact angle varied in a linear manner. Due to increasing pore size, progressively air is trapped into the pores leading to the higher contact angle.
- As the pore widening duration was increased, the contact angle was found to increase in both oxalic acid and sulphuric acids. PAA membranes showed hydrophilic properties in both oxalic acid and sulphuric acids in water medium. In fact, PAA membranes produced in sulphuric acid exhibited super hydrophilic nature which was confirmed through contact angle measurements in the acetone medium.

PAA membranes based nanostructures

- Silver nanoparticles were grown inside the pore of PAA successfully by electro-

less deposition method. XRD analysis of as PAA shows the amorphous nature, whereas Ag-PAA shows crystalline nature.

- The wall thickness of the pores played a major role in the formation of ANW array. The number of ANW array obtained in sulphuric alumina was more compared with that obtained from oxalic alumina, because of smaller pore wall thickness in sulphuric alumina.
- Copper nanowires were grown into the pores of PAA membranes by electroless deposition method. Cu nanowires were randomly oriented through the surface of the membrane and tips of the nanowires aggregate into clumps.

7.2 FUTURE DIRECTIONS

- The analysis of structural and optical properties of PAA membranes prepared at different anodization potentials (10-50 V) and to correlate the results with regularity ratio of PAA membranes.
- Preparation of PAA membranes at different annealing temperatures and to study the influence of regularity ratio and crystalline phase on the mechanical properties.
- Fabrication of Ni, Co, Fe and Ag nanowires on the pores of PAA membranes by chemical method. The sensing and magnetic properties of these metal nanostructures will be of specific interest.

REFERENCES

- Adiga, S. P., Jin, C., Curtiss, L. A., Monteiro-Riviere, N. A., and Narayan, R. J. (2009). “Nanoporous membranes for medical and biological applications”. *Wiley Interdisciplinary Reviews: Nanomedicine and Nanobiotechnology*, 1(5):568–581.
- Aerts, T., Dimogerontakis, T., De Graeve, I., Fransaer, J., and Terryn, H. (2007). “Influence of the anodizing temperature on the porosity and the mechanical properties of the porous anodic oxide film”. *Surface and Coatings Technology*, 201(16):7310–7317.
- Albu, S. P., Ghicov, A., Macak, J. M., Hahn, R., and Schmuki, P. (2007). “Self-organized, free-standing tio₂ nanotube membrane for flow-through photocatalytic applications”. *Nano letters*, 7(5):1286–1289.
- Alcala, G., Skeldon, P., Thompson, G., Mann, A., Habazaki, H., and Shimizu, K. (2002). “Mechanical properties of amorphous anodic alumina and tantalum films using nanoindentation”. *Nanotechnology*, 13(4):451.
- Alkire, R. C., Gogotsi, Y., Simon, P., and Eftekhari, A. (2008). *Nanostructured materials in electrochemistry*. John Wiley & Sons.
- Aramesh, M. and Cervenka, J. (2014). “Surface modification of porous anodic alumina for medical and biological applications”. *Nanomedicine*, 438:438.
- Balde, M., Vena, A., and Sorli, B. (2015). “Fabrication of porous anodic aluminium oxide layers on paper for humidity sensors”. *Sensors and Actuators B: Chemical*, 220:829–839.

- Barberoglou, M., Zorba, V., Pagozidis, A., Fotakis, C., and Stratakis, E. (2010). “Electrowetting properties of micro/nanostructured black silicon”. *Langmuir*, 26(15):13007–13014.
- Basu, S., Chatterjee, S., Saha, M., Bandyopadhyay, S., Mistry, K. K., and Sengupta, K. (2001). “Study of electrical characteristics of porous alumina sensors for detection of low moisture in gases”. *Sensors and Actuators B: Chemical*, 79(2):182–186.
- Baumann, W. (1936). “Wechselstromuntersuchungen an anodisch oxydiertem aluminium”. *Zeitschrift für Physik A Hadrons and Nuclei*, 102(1):59–66.
- Bengough, G. and Stuart, J. (1923). “Improved process of protecting surfaces of aluminum and aluminum alloys”. *UK patent*, 223994.
- Buijnsters, J. G., Zhong, R., Tsyntaru, N., and Celis, J.-P. (2013). “Surface wettability of macroporous anodized aluminum oxide”. *ACS applied materials & interfaces*, 5(8):3224–3233.
- Cassie, A. and Baxter, S. (1944). “Wettability of porous surfaces”. *Transactions of the Faraday society*, 40:546–551.
- Chen, H. M., Hsin, C. F., Liu, R.-S., Hu, S.-F., and Huang, C.-Y. (2007). “Controlling optical properties of aluminum oxide using electrochemical deposition”. *Journal of The Electrochemical Society*, 154(6):K11–K14.
- Chin, I., Yam, F., Chai, Y., and Hassan, Z. (2015). “Quantitative analysis of morphological and photoluminescence properties of porous anodic alumina formed in sulfuric acid”. *Journal of Porous Materials*, 22(5):1375–1382.
- Choudhari, K., Sudheendra, P., and Udayashankar, N. (2012). “Fabrication and high-temperature structural characterization study of porous anodic alumina membranes”. *Journal of Porous Materials*, 19(6):1053–1062.
- Chowdhury, P., Raghuvaran, K., Krishnan, M., Barshilia, H. C., and Rajam, K. (2011). “Effect of process parameters on growth rate and diameter of nano-porous alumina templates”. *Bulletin of Materials Science*, 34(3):423–427.

- Cloutier, S. G., Kossyrev, P. A., and Xu, J. (2005). “Optical gain and stimulated emission in periodic nanopatterned crystalline silicon”. *Nature materials*, 4(12):887–891.
- Corma, A. (2003). “State of the art and future challenges of zeolites as catalysts”. *Journal of Catalysis*, 216(1):298–312.
- Dehnavi, V., Liu, X. Y., Luan, B. L., Shoesmith, D. W., and Rohani, S. (2014). “Phase transformation in plasma electrolytic oxidation coatings on 6061 aluminum alloy”. *Surface and Coatings Technology*, 251:106–114.
- Despić, A. (1985). “A note on the effect of the electrolyte on the type of growth of anodic oxide on aluminium”. *Journal of electroanalytical chemistry and interfacial electrochemistry*, 191(2):417–423.
- Despić, A. and Parkhutik, V. P. (1989). “Electrochemistry of aluminum in aqueous solutions and physics of its anodic oxide”. In *Modern Aspects of Electrochemistry No. 20*, pages 401–503. Springer.
- Diggle, J. W., Downie, T. C., and Goulding, C. (1969). “Anodic oxide films on aluminum”. *Chemical Reviews*, 69(3):365–405.
- Doadrio, A., Sousa, E., Doadrio, J., Pariente, J. P., Izquierdo-Barba, I., and Vallet-Regí, M. (2004). “Mesoporous sba-15 hplc evaluation for controlled gentamicin drug delivery”. *Journal of Controlled Release*, 97(1):125–132.
- Du, Y., Cai, W., Mo, C., Chen, J., Zhang, L., and Zhu, X. (1999). “Preparation and photoluminescence of alumina membranes with ordered pore arrays”. *Applied Physics Letters*, 74(20):2951–2953.
- Ericson, F., Kristensen, N., Schweitz, J.-Å., and Smith, U. (1991). “A transmission electron microscopy study of hillocks in thin aluminum films”. *Journal of Vacuum Science & Technology B: Microelectronics and Nanometer Structures Processing, Measurement, and Phenomena*, 9(1):58–63.

- Fang, T.-H., Wang, T., Liu, C.-H., Ji, L.-W., and Kang, S.-H. (2007). “Physical behavior of nanoporous anodic alumina using nanoindentation and microhardness tests”. *Nanoscale Research Letters*, 2(8):410.
- Feng, L., Li, S., Li, Y., Li, H., Zhang, L., Zhai, J., Song, Y., Liu, B., Jiang, L., and Zhu, D. (2002). “Super-hydrophobic surfaces: from natural to artificial”. *Advanced materials*, 14(24):1857–1860.
- Fox, N. P. (2001). “Developments in optical radiation measurement at npl: part i”. In *International Symposium on Optical Science and Technology*, pages 140–154. International Society for Optics and Photonics.
- Fu, X., Zhang, B., Kang, X., Deng, J., Xiong, C., Dai, T., Jiang, X., Yu, T., Chen, Z., and Zhang, G. Y. (2011). “Gan-based light-emitting diodes with photonic crystals structures fabricated by porous anodic alumina template”. *Optics express*, 19(105):A1104–A1108.
- Gan, Y. X., Tavares, G. R., Gonzaga, R. S., and Gan, R. N. (2016). “Silver nanoparticle formation on metal substrate under concentration-limited condition”. *Journal of Micro and Nano-Manufacturing*, 4(3):034502.
- Garg, N. (2013). “Binarization techniques used for grey scale images”. *International Journal of Computer Applications*, 71(1).
- Gong, D., Grimes, C. A., Varghese, O. K., Hu, W., Singh, R., Chen, Z., and Dickey, E. C. (2001). “Titanium oxide nanotube arrays prepared by anodic oxidation”. *Journal of Materials Research*, 16(12):3331–3334.
- Han, J., Kim, J., Choi, Y., Chang, K.-S., Lee, J., Youn, H., and Bu, S. (2007). “Structure of alumina nanowires synthesized by chemical etching of anodic alumina membrane”. *Physica E: Low-dimensional Systems and Nanostructures*, 36(2):140–146.
- Horcas, I., Fernández, R., Gomez-Rodriguez, J., Colchero, J., Gómez-Herrero, J., and Baro, A. (2007). “Wsxm: a software for scanning probe microscopy and a tool for nanotechnology”. *Review of Scientific Instruments*, 78(1):013705.

- Huang, G., Wu, X., Mei, Y., Shao, X., and Siu, G. (2003). “Strong blue emission from anodic alumina membranes with ordered nanopore array”. *Journal of applied physics*, 93(1):582–585.
- Huang, G., Wu, X., Yang, L., Shao, X., Siu, G., and Chu, P. (2005). “Dependence of blue-emitting property on nanopore geometrical structure in al-based porous anodic alumina membranes”. *Applied Physics A: Materials Science & Processing*, 81(7):1345–1349.
- Ingham, C. J., ter Maat, J., and de Vos, W. M. (2012). “Where bio meets nano: the many uses for nanoporous aluminum oxide in biotechnology”. *Biotechnology advances*, 30(5):1089–1099.
- Jason, A. and Wood, J. (1955). “Some electrical effects of the adsorption of water vapour by anodized aluminium”. *Proceedings of the Physical Society. Section B*, 68(12):1105.
- Jessensky, O., Müller, F., and Gösele, U. (1998). “Self-organized formation of hexagonal pore arrays in anodic alumina”. *Applied physics letters*, 72(10):1173–1175.
- Keller, F., Hunter, M., and Robinson, D. (1953). “Structural features of oxide coatings on aluminum”. *Journal of the Electrochemical Society*, 100(9):411–419.
- Khan, G. G., Singh, A. K., and Mandal, K. (2013). “Structure dependent photoluminescence of nanoporous amorphous anodic aluminium oxide membranes: Role of f+ center defects”. *Journal of Luminescence*, 134:772–777.
- Khan, H. and Petrikowski, K. (2000). “Anisotropic structural and magnetic properties of arrays of fe 26 ni 74 nanowires electrodeposited in the pores of anodic alumina”. *Journal of Magnetism and Magnetic Materials*, 215:526–528.
- Kim, E., Jiang, Z.-T., and No, K. (2000). “Measurement and calculation of optical band gap of chromium aluminum oxide films”. *Japanese Journal of Applied Physics*, 39(8R):4820.

- Ko, S., Lee, D., Jee, S., Park, H., Lee, K., and Hwang, W. (2006). “Mechanical properties and residual stress in porous anodic alumina structures”. *Thin solid films*, 515(4):1932–1937.
- Kondo, T., Kitagishi, N., Fukushima, T., Yanagishita, T., and Masuda, H. (2016). “Fabrication of aluminum nanowires by mechanical deformation of Al using anodic porous alumina molds”. *Materials Express*, 6(4):363–366.
- Kukhta, A., Gorokh, G., Kolesnik, E., Mitkovets, A., Taoubi, M., Koshin, Y. A., and Mozalev, A. (2002). “Nanostructured alumina as a cathode of organic light-emitting devices”. *Surface science*, 507:593–597.
- Kulkarni, S. (1998). “Recent trends in the applications of zeolites and molecular sieves for the synthesis of speciality and fine chemicals”. *Studies in Surface Science and Catalysis*, 113:151–161.
- Kumar, A. S., Nagaraja, K., and Nagaraja, H. (2013). “Effect of Sn doping on structural, optical, electrical and wettability properties of oriented ZnO nanorod arrays”. *Journal of Materials Science: Materials in Electronics*, 24(10):3812–3822.
- Kumeria, T., Santos, A., and Losic, D. (2014). “Nanoporous anodic alumina platforms: engineered surface chemistry and structure for optical sensing applications”. *Sensors*, 14(7):11878–11918.
- Laatar, F., Hassen, M., Amri, C., Laatar, F., Smida, A., and Ezzaouia, H. (2016). “Fabrication of CdSe nanocrystals using porous anodic alumina and their optical properties”. *Journal of Luminescence*, 178:13–21.
- Lee, W., Ji, R., Gösele, U., and Nielsch, K. (2006). “Fast fabrication of long-range ordered porous alumina membranes by hard anodization”. *Nature materials*, 5(9):741–747.
- Leese, H., Bhurtun, V., Lee, K. P., and Mattia, D. (2013). “Wetting behaviour of hydrophilic and hydrophobic nanostructured porous anodic alumina”. *Colloids and Surfaces A: Physicochemical and Engineering Aspects*, 420:53–58.

- Leng, Y. (2009). *Materials characterization: introduction to microscopic and spectroscopic methods*. John Wiley & Sons.
- Li, A.-P., Müller, F., Birner, A., Nielsch, K., and Gösele, U. (1999). "Fabrication and microstructuring of hexagonally ordered two-dimensional nanopore arrays in anodic alumina". *Advanced Materials*, 11(6):483–487.
- Li, F., Zhang, L., and Metzger, R. M. (1998). "On the growth of highly ordered pores in anodized aluminum oxide". *Chemistry of materials*, 10(9):2470–2480.
- Li, G., Zhang, Y., Wu, Y., and Zhang, L. (2003). "Wavelength dependent photoluminescence of anodic alumina membranes". *Journal of Physics: Condensed Matter*, 15(49):8663.
- Li, N., Li, X., Yin, X., Wang, W., and Qiu, S. (2004). "Electroless deposition of open-end Cu nanotube arrays". *Solid state communications*, 132(12):841–844.
- Li, Z. and Huang, K. (2007a). "Blue luminescence in porous anodic alumina films". *Journal of Physics: Condensed Matter*, 19(21):216203.
- Li, Z. and Huang, K. (2007b). "The effect of high-temperature annealing on optical properties of porous anodic alumina formed in oxalic acid". *Luminescence*, 22(4):355–361.
- Liu, K., Chien, C., Searson, P., and Yu-Zhang, K. (1998). "Structural and magneto-transport properties of electrodeposited bismuth nanowires". *Applied physics letters*, 73(10):1436–1438.
- Liu, X., Xu, F., Li, Z., and Zhang, W. (2008). "Photoluminescence of poly (thiophene) nanowires confined in porous anodic alumina membrane". *Polymer*, 49(9):2197–2201.
- Liu, Y.-F., Tu, Y.-F., Huang, S.-Y., Sang, J.-P., and Zou, X.-W. (2009). "Effect of etch-treatment upon the intensity and peak position of photoluminescence spectra for anodic alumina films with ordered nanopore array". *Journal of materials science*, 44(13):3370–3375.

- Lu, G. and Zhao, X. S. (2004). “*Nanoporous materials: science and engineering*”, volume 4. World Scientific.
- Lu, Q., Alcalá, G., Skeldon, P., Thompson, G., Graham, M., Masheder, D., Shimizu, K., and Habazaki, H. (2002). “Porous tantalum and alumina films from non-thickness limited anodising in phosphate/glycerol electrolyte”. *Electrochimica acta*, 48(1):37–42.
- Lu, Z., Ruan, W., Yang, J., Xu, W., Zhao, C., and Zhao, B. (2009). “Deposition of Ag nanoparticles on porous anodic alumina for surface enhanced Raman scattering substrate”. *Journal of Raman Spectroscopy*, 40(1):112–116.
- Ma, D., Li, S., and Liang, C. (2009). “Electropolishing of high-purity aluminium in perchloric acid and ethanol solutions”. *Corrosion Science*, 51(4):713–718.
- Majid, F., Riaz, S., Ijaz, T., Farooq, M., and Naseem, S. (2013). “*Synthesis and Characterization of Sol-gel Deposited Aluminum Oxide at Low Temperatures*”.
- Martinson, A. B., Elam, J. W., Hupp, J. T., and Pellin, M. J. (2007). “ZnO nanotube based dye-sensitized solar cells”. *Nano letters*, 7(8):2183–2187.
- Masuda, H. and Fukuda, K. (1995). “Ordered metal nanohole arrays made by a two-step replication of honeycomb structures of anodic alumina”. *science*, 268(5216):1466.
- Masuda, H., Yamada, H., Satoh, M., Asoh, H., Nakao, M., and Tamamura, T. (1997). “Highly ordered nanochannel-array architecture in anodic alumina”. *Applied Physics Letters*, 71(19):2770–2772.
- Mei, Y., Siu, G., Fu, R. K., Chen, P., Wu, X., Hung, T., Chu, P. K., and Yang, Y. (2005). “Formation mechanism of alumina nanotubes and nanowires from highly ordered porous anodic alumina template”. *Journal of applied physics*, 97(3):034305.
- Mendham, J. et al. (2006). “*Vogel's textbook of quantitative chemical analysis*”. Pearson Education India.

- Mínguez-Bacho, I., Rodríguez-López, S., Asenjo, A., Vázquez, M., and Hernández-Vélez, M. (2012). “Self-correlation function for determination of geometrical parameters in nanoporous anodic alumina films”. *Applied Physics A: Materials Science & Processing*, 106(1):105–112.
- Mukherjee, N., Paulose, M., Varghese, O. K., Mor, G., and Grimes, C. A. (2003). “Fabrication of nanoporous tungsten oxide by galvanostatic anodization”. *Journal of Materials Research*, 18(10):2296–2299.
- Murphy, J. and Michelson, C. (1962). “A theory for the formation of anodic oxide coatings on aluminum”. In *Proceedings of Conference on Anodizing Aluminum, Nottingham*, page 83.
- Nahar, R. and Khanna, V. (1998). “Ionic doping and inversion of the characteristic of thin film porous Al₂O₃ humidity sensor”. *Sensors and Actuators B: Chemical*, 46(1):35–41.
- Ng, K., Lin, Y., and Ngan, A. (2009). “Deformation of anodic aluminum oxide nano-honeycombs during nanoindentation”. *Acta Materialia*, 57(9):2710–2720.
- Ng, K. and Ngan, A. (2012). “Effects of pore-channel ordering on the mechanical properties of anodic aluminum oxide nano-honeycombs”. *Scripta Materialia*, 66(7):439–442.
- Ngan, A. (2005). “On the distribution of elastic forces in disordered structures and materials. i. computer simulation”. In *Proceedings of the Royal Society of London A: Mathematical, Physical and Engineering Sciences*, volume 461, pages 433–458. The Royal Society.
- Nielsch, K., Wehrspohn, R., Barthel, J., Kirschner, J., Gösele, U., Fischer, S., and Kronmüller, H. (2001). “Hexagonally ordered 100 nm period nickel nanowire arrays”. *Applied Physics Letters*, 79(9):1360–1362.
- Nourmohammadi, A., Asadabadi, S. J., Yousefi, M. H., and Ghasemzadeh, M. (2012). “Photoluminescence emission of nanoporous anodic aluminum oxide films prepared in phosphoric acid”. *Nanoscale research letters*, 7(1):689.

- Oliver, W. C. and Pharr, G. M. (2004). "Measurement of hardness and elastic modulus by instrumented indentation: Advances in understanding and refinements to methodology". *Journal of materials research*, 19(01):3–20.
- O'sullivan, J. and Wood, G. (1970). "The morphology and mechanism of formation of porous anodic films on aluminium". In *Proceedings of the Royal Society of London A: Mathematical, Physical and Engineering Sciences*, volume 317, pages 511–543. The Royal Society.
- Patemarakis, G. and Moussoutzanis, K. (1995). "Electrochemical kinetic study on the growth of porous anodic oxide films on aluminium". *Electrochimica acta*, 40(6):699–708.
- Paulose, M., Shankar, K., Yoriya, S., Prakasam, H. E., Varghese, O. K., Mor, G. K., Latempa, T. A., Fitzgerald, A., and Grimes, C. A. (2006a). "Anodic growth of highly ordered tio₂ nanotube arrays to 134 μm in length". *The Journal of Physical Chemistry B*, 110(33):16179–16184.
- Paulose, M., Shankar, K., Yoriya, S., Prakasam, H. E., Varghese, O. K., Mor, G. K., Latempa, T. A., Fitzgerald, A., and Grimes, C. A. (2006b). "Anodic growth of highly ordered tio₂ nanotube arrays to 134 μm in length". *The Journal of Physical Chemistry B*, 110(33):16179–16184.
- Pena, D. J., Razavi, B., Smith, P. A., Mbindyo, J. K., Natan, M. J., Mayer, T. S., Mallouk, T. E., and Keating, C. D. (2000). "Electrochemical synthesis of multi-material nanowires as building blocks for functional nanostructures". In *MRS Proceedings*, volume 636, pages D4–6. Cambridge Univ Press.
- Poinern, G. E. J., Ali, N., and Fawcett, D. (2011). "Progress in nano-engineered anodic aluminum oxide membrane development". *Materials*, 4(3):487–526.
- Qurashi, A. (2013). "Structural and optical properties of ultrathin zno nanoneedles grown on gan substrate by hybrid approach". *Journal of Physics and Chemistry of Solids*, 74(1):166–169.

- Rathmell, A. R., Bergin, S. M., Hua, Y.-L., Li, Z.-Y., and Wiley, B. J. (2010). “The growth mechanism of copper nanowires and their properties in flexible, transparent conducting films”. *Advanced materials*, 22(32):3558–3563.
- Rauf, A., Mehmood, M., Rasheed, M. A., and Aslam, M. (2009). “The effects of electropolishing on the nanochannel ordering of the porous anodic alumina prepared in oxalic acid”. *Journal of Solid State Electrochemistry*, 13(2):321–332.
- Reddy, P. R., Ajith, K., and Udayashankar, N. (2016). “Morphological analysis and photoluminescence properties of hydrophilic porous anodic alumina formed in oxalic acid”. *Journal of Materials Science: Materials in Electronics*, 27(5):5331–5344.
- Redon, R., Vázquez-Olmos, A., Mata-Zamora, M., Ordóñez-Medrano, A., Rivera-Torres, F., and Saniger, J. (2005). “Contact angle studies on anodic porous alumina”. *Journal of colloid and interface science*, 287(2):664–670.
- Reich, D., Tanase, M., Hultgren, A., Bauer, L., Chen, C., and Meyer, G. J. (2003). “Biological applications of multifunctional magnetic nanowires”. *Journal of Applied Physics*, 93(10):7275–7280.
- Ren, X., Huang, X., Zhang, H., and He, M. (2007). “Fabrication of cu nano-arrays by template method and their characterizations”. *Frontiers of Materials Science in China*, 1(3):312–315.
- Riveros, G., Green, S., Cortes, A., Gomez, H., Marotti, R., and Dalchiele, E. (2006). “Silver nanowire arrays electrochemically grown into nanoporous anodic alumina templates”. *Nanotechnology*, 17(2):561.
- Romero, V., Vega, V., Garcia, J., Prida, V. M., Hernando, B., and Benavente, J. (2014). “Effect of porosity and concentration polarization on electrolyte diffusive transport parameters through ceramic membranes with similar nanopore size“. *Nanomaterials*, 4(3):700–711.
- Rudawska, A. and Jacniacka, E. (2009). “Analysis for determining surface free energy uncertainty by the owen–wendt method”. *International Journal of Adhesion and Adhesives*, 29(4):451–457.

- Samantilleke, A., Carneiro, J., Azevedo, S., Thuy, T., and Teixeira, V. (2013). “Electrochemical anodizing, structural and mechanical characterization of nanoporous alumina templates”. In *Journal of nano research*, volume 25, pages 77–89. Trans Tech Publ.
- Santos, A., Alba, M., Rahman, M. M., Formentín, P., Ferré-Borrull, J., Pallarès, J., and Marsal, L. F. (2012). “Structural tuning of photoluminescence in nanoporous anodic alumina by hard anodization in oxalic and malonic acids”. *Nanoscale research letters*, 7(1):228.
- Santos, A., Kumeria, T., and Losic, D. (2014). “Nanoporous anodic alumina: a versatile platform for optical biosensors”. *Materials*, 7(6):4297–4320.
- SEE YEOW HOE, G. (2005). “*Fabrication of tungsten oxide nanostructured films using anodic porous alumina and application in gas sensing*”. PhD thesis.
- Senbahavalli, R., Mohanapriya, S., and Raj, V. (2016). “Enhanced corrosion resistance of anodic non-porous alumina (anpa) coatings on aluminium fabricated from mixed organic-inorganic electrolytes”. *Materials Discovery*, 3:29–37.
- Shaban, M. (2016). “Morphological and optical characterization of high density au/paa nanoarrays”. *Journal of Spectroscopy*, 2016.
- Sieber, I., Hildebrand, H., Friedrich, A., and Schmuki, P. (2005a). “Formation of self-organized niobium porous oxide on niobium”. *Electrochemistry Communications*, 7(1):97–100.
- Sieber, I., Kannan, B., and Schmuki, P. (2005b). “Self-assembled porous tantalum oxide prepared in h_2 so $4/hf$ electrolytes”. *Electrochemical and Solid-State Letters*, 8(3):J10–J12.
- Siejka, J. and Ortega, C. (1977). “An o18 study of field-assisted pore formation in compact anodic oxide films on aluminum”. *Journal of The Electrochemical Society*, 124(6):883–891.

- Stefanovich, G., Pergament, A., Velichko, A., and Stefanovich, L. (2004). “Anodic oxidation of vanadium and properties of vanadium oxide films”. *Journal of physics: condensed matter*, 16(23):4013.
- Stepniowski, W. J. and Bojar, Z. (2011). “Synthesis of anodic aluminum oxide (aao) at relatively high temperatures. study of the influence of anodization conditions on the alumina structural features”. *Surface and Coatings Technology*, 206(2):265–272.
- Stepniowski, W. J., Choi, J., Yoo, H., Oh, K., Michalska-Domańska, M., Chilimoniuk, P., Czujko, T., Łyszkowski, R., Józwiak, S., Bojar, Z., et al. (2016). “Anodization of FeAl intermetallic alloys for bandgap tunable nanoporous mixed aluminum-iron oxide”. *Journal of Electroanalytical Chemistry*, 771:37–44.
- Stepniowski, W. J., Michalska-Domańska, M., Norek, M., and Czujko, T. (2014a). “Fast fourier transform based arrangement analysis of poorly organized alumina nanopores formed via self-organized anodization in chromic acid”. *Materials Letters*, 117:69–73.
- Stepniowski, W. J., Norek, M., Michalska-Domańska, M., Forbot, D., and Król, A. (2014b). “Study on the correlation between criterion derived from rayleigh–bénard convective cells and arrangement of nanoporous anodic aluminum oxide”. *Materials Letters*, 125:124–127.
- Stepniowski, W. J., Nowak-Stepniowska, A., Presz, A., Czujko, T., and Varin, R. A. (2014c). “The effects of time and temperature on the arrangement of anodic aluminum oxide nanopores”. *Materials characterization*, 91:1–9.
- Stepniowski, W. J. and Salerno, M. (2014). “Fabrication of nanowires and nanotubes by anodic alumina template-assisted electrodeposition”. *Manufacturing Nanostructures*, pages 321–357.
- Stepniowski, W. J., Zasada, D., and Bojar, Z. (2011). “First step of anodization influences the final nanopore arrangement in anodized alumina”. *Surface and Coatings Technology*, 206(6):1416–1422.

- Storm, A., Chen, J., Ling, X., Zandbergen, H., and Dekker, C. (2003). “Fabrication of solid-state nanopores with single-nanometre precision”. *Nature materials*, 2(8):537–540.
- Su, Z. and Zhou, W. (2008a). “Formation mechanism of porous anodic aluminium and titanium oxides”. *Advanced Materials*, 20(19):3663–3667.
- Su, Z. and Zhou, W. (2008b). “Porous anodic metal oxides”. *Science Foundation in China*, 16(1):36.
- Sui, Y., Cui, B., Guardian, R., Acosta, D., Martinez, L., and Perez, R. (2002). “Growth of carbon nanotubes and nanofibres in porous anodic alumina film”. *Carbon*, 40(7):1011–1016.
- Sulka, G. and Parkola, K. (2007). “Temperature influence on well-ordered nanopore structures grown by anodization of aluminium in sulphuric acid”. *Electrochimica Acta*, 52(5):1880–1888.
- Sulka, G. D., Brzózka, A., Zaraska, L., and Jaskuła, M. (2010). “Through-hole membranes of nanoporous alumina formed by anodizing in oxalic acid and their applications in fabrication of nanowire arrays”. *Electrochimica Acta*, 55(14):4368–4376.
- Sulka, G. D. and Stepniowski, W. J. (2009). “Structural features of self-organized nanopore arrays formed by anodization of aluminum in oxalic acid at relatively high temperatures”. *Electrochimica Acta*, 54(14):3683–3691.
- Takahashi, H., Fujimoto, K., and Nagayama, M. (1988). “Effect of pH on the distribution of anions in anodic oxide films formed on aluminum in phosphate solutions”. *Journal of The Electrochemical Society*, 135(6):1349–1353.
- Tan, J. C. and Cheetham, A. K. (2011). “Mechanical properties of hybrid inorganic–organic framework materials: establishing fundamental structure–property relationships”. *Chemical Society Reviews*, 40(2):1059–1080.

- Tao, G., Guo-Wen, M., and Li-De, Z. (2003). “Origin of the blue luminescence in porous anodic alumina films formed in oxalic acid solutions”. *Chinese physics letters*, 20(5):713.
- Tasaltin, N., Sanli, D., Jonáš, A., Kiraz, A., and Erkey, C. (2011). “Preparation and characterization of superhydrophobic surfaces based on hexamethyldisilazane-modified nanoporous alumina”. *Nanoscale research letters*, 6(1):487.
- Tian, M., Wang, J., Snyder, J., Kurtz, J., Liu, Y., Schiffer, P., Mallouk, T. E., and Chan, M. (2003). “Synthesis and characterization of superconducting single-crystal sn nanowires”. *Applied Physics Letters*, 83(8):1620–1622.
- Tsuchiya, H., Macak, J. M., Sieber, I., and Schmuki, P. (2005). “Self-organized high-aspect-ratio nanoporous zirconium oxides prepared by electrochemical anodization”. *Small*, 1(7):722–725.
- Tsyntsaru, N., Kavas, B., Sort, J., Urgen, M., and Celis, J.-P. (2014). “Mechanical and frictional behaviour of nano-porous anodised aluminium”. *Materials Chemistry and Physics*, 148(3):887–895.
- Vallet-Regí, M. (2006). “Ordered mesoporous materials in the context of drug delivery systems and bone tissue engineering”. *Chemistry–A European Journal*, 12(23):5934–5943.
- Voon, C. H. and Derman, M. N. (2013). “Effect of electrolyte concentration on the growth of porous anodic aluminium oxide (aao) on al-mn alloys”. In *Advanced Materials Research*, volume 626, pages 610–614. Trans Tech Publ.
- Vrublevsky, I., Chernyakova, K., Ispas, A., Bund, A., and Zavadski, S. (2014). “Optical properties of thin anodic alumina membranes formed in a solution of tartaric acid”. *Thin Solid Films*, 556:230–235.
- Walsh, R. J. and Chumanov, G. (2001). “Silver coated porous alumina as a new substrate for surface-enhanced raman scattering”. *Applied spectroscopy*, 55(12):1695–1700.

- Wang, W., Li, N., Li, X., Geng, W., and Qiu, S. (2006). “Synthesis of metallic nanotube arrays in porous anodic aluminum oxide template through electroless deposition”. *Materials research bulletin*, 41(8):1417–1423.
- Wu, Z., Richter, C., and Menon, L. (2007). “A study of anodization process during pore formation in nanoporous alumina templates”. *Journal of the Electrochemical Society*, 154(1):E8–E12.
- Xia, Z., Riestler, L., Sheldon, B., Curtin, W., Liang, J., Yin, A., and Xu, J. (2004). “Mechanical properties of highly ordered nanoporous anodic alumina membranes”. *Rev. Adv. Mater. Sci*, 6(2):131–139.
- Yamane, M. and Mackenzie, J. (1974). “Vicker’s hardness of glass”. *Journal of Non-Crystalline Solids*, 15(2):153–164.
- Yan, H., Choe, H. S., Nam, S., Hu, Y., Das, S., Klemic, J. F., Ellenbogen, J. C., and Lieber, C. M. (2011). “Programmable nanowire circuits for nanoprocessors”. *Nature*, 470(7333):240–244.
- Yang, C., Shen, W., Zhang, Y., Ye, Z., Zhang, X., Li, K., Fang, X., and Liu, X. (2014). “Color-tuning method by filling porous alumina membrane using atomic layer deposition based on metal–dielectric–metal structure”. *Applied optics*, 53(4):A142–A147.
- Yanson, A., Bollinger, G. R., Van den Brom, H., Agrait, N., and Van Ruitenbeek, J. (1998). “Formation and manipulation of a metallic wire of single gold atoms”. *Nature*, 395(6704):783–785.
- Yao, J., Liu, Z., Liu, Y., Wang, Y., Sun, C., Bartal, G., Stacy, A. M., and Zhang, X. (2008). “Optical negative refraction in bulk metamaterials of nanowires”. *Science*, 321(5891):930–930.
- Yao, L., Zheng, M., Li, H., Ma, L., and Shen, W. (2009). “High-performance humidity sensors based on high-field anodized porous alumina films”. *Nanotechnology*, 20(39):395501.

- Ye, S., Hou, Y., Zhu, R., Gu, S., Wang, J., Zhang, Z., Shi, S., and Du, J. (2011). “Synthesis and photoluminescence enhancement of silver nanoparticles decorated porous anodic alumina”. *Journal of Materials Science & Technology*, 27(2):165–169.
- Yuan, Y. and Lee, T. R. (2013). “Contact angle and wetting properties“. In *Surface science techniques*, pages 3–34. Springer.
- Zaraska, L., Sulka, G., and Jaskuła, M. (2009). “Properties of nanostructures obtained by anodization of aluminum in phosphoric acid at moderate potentials”. In *Journal of Physics: Conference Series*, volume 146, page 012020. IOP Publishing.
- Zaraska, L., Sulka, G. D., Szeremeta, J., and Jaskula, M. (2010). “Porous anodic alumina formed by anodization of aluminum alloy (aa1050) and high purity aluminum”. *Electrochimica Acta*, 55(14):4377–4386.
- Zhou, F., Baron-Wiecheć, A., Garcia-Vergara, S., Curioni, M., Habazaki, H., Skeldon, P., and Thompson, G. (2012). “Effects of current density and electrolyte temperature on the volume expansion factor of anodic alumina formed in oxalic acid”. *Electrochimica Acta*, 59:186–195.

List of Publications

List of Publications based on Research Work

Refereed International Journals

- **Ramana Reddy P.**, Ajith K.M, Udayashankar N.K, (2016), “Micro and nanoindentation analysis of porous anodic alumina prepared in oxalic and sulphuric acid”, *Ceramics International*, (Elsevier Journal), DOI: 10.1016/j.ceramint.2016.08.109.
- **Ramana Reddy P.**, Ajith K.M, Udayashankar N.K, (2016), “Morphological and photoluminescence properties of hydrophilic porous anodic alumina formed in oxalic acid”, *Journal of materials science: Materials in Electronics*, (Springer Journal), DOI: 10.1007/s10854-016-4432-6.
- **Ramana Reddy P.**, Ajith K.M, Udayashankar N.K, (2016), “ Contact angle measurement studies on porous anodic alumina membranes prepared using different electrolytes ”, *Advanced Materials Letters*, DOI: 10.5185/amlett.2016.6230
- **Ramana Reddy P.**, Ajith K.M, Udayashankar N.K, (2016), “Structural analysis of Porous Anodic Alumina Templates using the dedicated executable software”, *Advanced Science Letters*, (American Scientific publishers), DOI:<https://doi.org/10.1166/asl.2016.6956>.

International Conference Proceedings

- **Ramana Reddy P.**, Ajith K.M, Udayashankar N.K, (2015), “Studies on Mechanical properties of Porous Anodic Alumina Templates using microindentation test”, *AIP Conference Proceedings*, 1655, 050169, DOI: 10.1063/1.4917810.

Papers Presented in International Conferences

- **Ramana Reddy P.**, Ajith K.M, Udayashankar N.K, (2013). Studies of Structural Properties of Porous Anodic Alumina Templates prepared by using two Step

Anodization Process **International union of materials research society, Materials society of India, International conference in Asia (IUMRS-ICA 2013)**, December 16-20, Indian Institute of Science, Bangalore, India.

- **Ramana Reddy P.**, Ajith K.M, Udayashankar N.K, (2014). The Effect of Process Parameters on the growth mechanism of Porous Anodic Alumina Templates **International Conference of Functional Materials (ICFM-2014)**, Indian Institute of Technology, Kharagpur, February, 14-17, Kharagpur, India.
- **Ramana Reddy P.**, Ajith K.M, Udayashankar N.K, (2014). Thermal properties of porous anodic alumina templates. **International Conference on Materials and Characterization Techniques (ICMCT-2014)**, Vellore Institute of Technology, March, 10-12, Vellore, India.
- **Ramana Reddy P.**, Ajith K.M, Udayashankar N.K, (2014). Structural Analysis of Porous Anodic Alumina Membranes using the dedicated executable software, **International Conference on nano technology: Smart Materials, Composites, Applications and New Inventions (NANOCON-2014)**, Bharati Vidyapeeth University, October 14-15, *best poster award* Pune, India.
- **Ramana Reddy P.**, Ajith K.M, Udayashankar N.K, (2014). Studies on mechanical properties of porous anodic alumina membranes using microindentation test, **59th DAE Solid State Physics Symposium (DAE-SSPS-2014)**, Vellore Institute of Technology, December 16-20, Vellore, India.
- **Ramana Reddy P.**, Ajith K.M, Udayashankar N.K, (2015). Contact angle measurement studies on porous anodic alumina membranes prepared using different electrolytes, **Recent Advances in Nano-Science and Technology (RAINSAT-2015)**, Sathyabama University, July 8-10, India.

Curriculum Vitae

Address for correspondence:

Research Scholar,
Department of Physics,
National Institute of Technology Karnataka,
Surathkal, Mangalore - 575 025.
Phone: +91 9483205247
E-mail: ramana.nitk@gmail.com



Research Interests

- Template-assisted growth of porous anodic alumina nanostructures
- Semiconductor nanostructures by electrochemical Methods
- Sensors and supercapacitor applications

Educational Qualifications

- Doctoral Research towards Ph.D [2011–2017]
Thesis title: Preparation and characterization of porous anodic alumina nanostructures
Department of Physics,
National Institute of Technology Karnataka, Surathkal, Mangalore-575025, India.
- Master of Technology (M.Tech) [2008–2010]
Thesis title: Two electron system in a Gaussian Quantum Dot in a Magnetic field
Department of Physics,
University of Hyderabad, Prof. CR Rao Rd, Gachibowli, Hyderabad, Telangana-500046, India.
Aggregate: 7.63 (CGPA)

- Master of Science (M.Sc in Physics) [2005–2007]
Department of Physics,
Osmania University, Main Road, Amberpet, Hyderabad, Telangana-500007, India.
Aggregate: 65.66 %

Computer Skills

Origin Lab, Ubuntu 14.10, Latex, Beamer latex presentations, Windows, MS Word, Excel, PowerPoint and particle analysis using Image-J and WSxM softwares.

Teaching Experience

Teaching Assistant, 2012-2016

M.Sc, B.Tech labs

NITK Surathkal, Karnataka

Department: Physics

Lecturer 2007-2008

B.Sc lab courses

Ambedkar degree and PG college, Hyderabad

Department: Physics

XXXIX National level workshop on Experimental Physics,

NITK Surathkal-Karnataka